



CERN-THESIS-2007-132

# Reconstruction of charged kaons in the three pion decay channel in Pb+Au 158 AGeV collisions by the CERES experiment

---

Vom Fachbereich Physik  
der Technischen Universität Darmstadt

zur Erlangung des Grades  
eines Doktors der Naturwissenschaften  
(Dr. rer. nat.)

genehmigte Dissertation von

**Mgr. Matúš Kaliský**

aus Banská Bystrica

---

Referent: Prof. Dr. P. Braun-Munzinger

Korreferent: Prof. Dr. N. Pietralla

Tag der Einreichung: 04.12.2007

Tag der Prüfung: 28.01.2008

**Darmstadt 2007**

**D 17**





## Abstract

Strangeness production in ultra-relativistic nucleus-nucleus collisions is one of the most important probes of hot and dense nuclear matter. Yields and spectra of hadrons carrying strangeness are being studied over a broad range of energies. A remarkable result is that the yields of strange hadrons appear to be in chemical equilibrium in nucleus-nucleus collisions in contrast to observations in elementary collisions.

The first part of this thesis is dedicated to the reconstruction of charged kaons in central Pb+Au collisions at the top SPS energy with the CERES spectrometer. The analysis scheme is based on the reconstruction of the decay of charged kaons in three charged pions. This approach is, with the exception of the pioneering work of the NA35 experiment, applied for the first time in ultra relativistic heavy ion collisions for the charged kaons reconstruction. In total 102k  $K^+$  and 57k  $K^-$  were reconstructed in 24.3M central Pb+Au collisions. The mid-rapidity yields are 31.8 for  $K^+$  and 19.3 for the  $K^-$ . These results together with  $K^-/K^+$ ,  $K^+/\pi^+$  and  $K^-/\pi^-$  ratios are compared with the existing results from NA49, NA44, NA57 and CERES measurements as well as with thermal model predictions.

The second part of this thesis is devoted to the study of fast Transition Radiation Detectors (TRD). Results of a stand alone simulation study of the performance of a TRD detector with gas chamber read out in terms of electron-pion separation as a function of the main parameters of the radiator and readout detector are shown. The optimization of the detector was based on the requirements of the CBM experiment. A comparison of simulated energy deposition to experimental data is presented.

## Zusammenfassung

Die Strangeness Produktion in ultrarelativistischen Kern-Kern Stößen ist eine der wichtigsten Sonden für die Untersuchung heißer und dichter Kernmaterie. Multiplizitäten und Spektren Strangeness tragender Hadronen werden daher über einen großen Energiebereich analysiert. Ein bemerkenswertes Ergebnis ist, dass sich im Gegensatz zu Proton-Proton Kollisionen, die Multiplizitäten von Hadronen mit Strangeness bei Kern-Kern Stößen im chemischen Gleichgewicht befinden.

Der erste Teil dieser Arbeit beschäftigt sich mit der Rekonstruktion geladener Kaonen in zentralen Pb+Au Kollisionen bei Top SPS-Energie, gemessen mit dem CERES Spektrometer. Die Analyse basiert auf der Rekonstruktion des Zerfalls geladener Kaonen in drei geladene Pionen. Dieser Ansatz ist, mit Ausnahme der Pionierarbeit des NA35 Experimentes, zum ersten mal für die Rekonstruktion geladener Kaonen in ultrarelativistischen Schwerionen-Kollisionen angewendet worden. In 24.3M zentralen Pb-Au Kollisionen wurden insgesamt 102k  $K^+$  und 57k  $K^-$  rekonstruiert. Die Multiplizitäten bei Midrapitität betragen 31.8 für  $K^+$  und 19.3 für  $K^-$ . Diese Ergebnisse sowie die Multiplizitätsverhältnisse  $K^-/K^+$ ,  $K^+/\pi^+$  und  $K^-/\pi^-$  werden sowohl mit den zur Verfügung stehenden Ergebnissen der Experimente NA49, NA44, NA57 und CERES, als auch den Voraussagen eines thermischen Modells verglichen.

Im zweiten Teil wird die Studie zu einem schnellen Übergangsstrahlungsdetektor (Transition Radiation Detector - TRD) vorgestellt. Die Ergebnisse einer Stand-Alone Simulation zur Effizienz der Elektron-Pion Trennung eines TRD mit Gas-Proportionalzähler-Auslese in Abhängigkeit der wichtigsten Parameter des Radiators, als auch des Auslesedetektors werden besprochen. Der simulierte Energieverlust wird mit experimentellen Daten verglichen.







# Contents

<b>1</b>	<b>Heavy ion collisions</b>	<b>5</b>
1.1	Introduction . . . . .	5
1.2	Hot and Dense Nuclear Matter . . . . .	5
1.3	Evolution and Dynamics of a Heavy Ion Collision . . . . .	7
1.4	Probes and observables (how to find the QGP) . . . . .	10
<b>2</b>	<b>Strangeness production in nuclear collisions</b>	<b>13</b>
2.1	Introduction . . . . .	13
2.2	Existing results . . . . .	14
2.3	Strangeness in CERES . . . . .	15
<b>3</b>	<b>NA45/CERES experiment</b>	<b>17</b>
3.1	Target area and trigger setup . . . . .	17
3.2	Silicon Drift Detectors . . . . .	19
3.3	RICH Detectors . . . . .	20
3.4	Time Projection Chamber . . . . .	20
3.5	Tracking . . . . .	22
<b>4</b>	<b>Analysis of the <math>K^+</math> and <math>K^-</math></b>	<b>25</b>
4.1	Charged kaons and CERES - basic facts . . . . .	25
4.2	Reconstruction strategy . . . . .	26
4.2.1	Data and event selection . . . . .	26
4.2.2	Centrality and multiplicity . . . . .	27
4.2.3	Analysis cuts . . . . .	28
4.3	Analysis cuts . . . . .	29
4.3.1	R0 cut . . . . .	30
4.3.2	Number of hits cut . . . . .	30
4.3.3	dE/dx cut . . . . .	31
4.3.4	$\Delta\phi$ R2M cut . . . . .	31
4.3.5	Secondary vertex quality cut . . . . .	32
4.3.6	Secondary vertex position cut . . . . .	33

4.3.7	K0 cut . . . . .	34
4.4	Phase space cuts . . . . .	34
4.4.1	Min $p_T$ cut . . . . .	34
4.4.2	R380 versus $\theta_{R2M}$ cut . . . . .	34
4.4.3	Min opening angle cuts . . . . .	35
4.5	Analysis chain . . . . .	35
4.5.1	User-input . . . . .	36
4.5.2	GEANT transport . . . . .	36
4.5.3	Step2 analyzer . . . . .	37
4.5.4	Step2 and Step3c MC/OMC analysis . . . . .	38
4.5.5	Step4 analysis . . . . .	39
4.6	Invariant mass spectrum . . . . .	39
4.7	Mixed event background . . . . .	39
<b>5</b>	<b>MC Simulations</b>	<b>43</b>
5.1	Introduction . . . . .	43
5.2	Single track efficiency . . . . .	44
5.3	Cut study . . . . .	44
5.3.1	No cuts applied . . . . .	46
5.3.2	R0 cut . . . . .	47
5.3.3	NHits cut . . . . .	49
5.3.4	dE/dx cut . . . . .	50
5.3.5	$\Delta\phi$ R2M cut . . . . .	53
5.3.6	Kaon vertex quality cut - TDTV . . . . .	54
5.3.7	Kaon vertex position . . . . .	55
5.3.8	K0 cut . . . . .	56
5.3.9	Opening angle cut . . . . .	57
5.3.10	R380 versus $\theta_{Local}$ cut . . . . .	59
5.3.11	Summary . . . . .	60
5.4	Cut Study II . . . . .	61
5.4.1	Cut distributions . . . . .	61
5.4.2	Cut stability . . . . .	61
5.4.3	Peak extraction efficiency . . . . .	61
5.4.4	Fit parameters . . . . .	64
<b>6</b>	<b>Final results</b>	<b>67</b>
6.1	Raw yield . . . . .	67
6.2	Transverse momentum spectrum . . . . .	68
6.3	Transverse mass spectra . . . . .	74
6.4	Rapidity spectrum . . . . .	76
6.5	Systematic error estimation . . . . .	76

---

6.5.1	Peak extraction . . . . .	77
6.5.2	OMC correction . . . . .	77
6.5.3	$p_T$ spectra extrapolation . . . . .	77
6.6	Final errors . . . . .	80
6.7	Final spectra . . . . .	82
6.8	Comparison to other experiments . . . . .	84
6.8.1	NA49 and NA44 . . . . .	84
6.8.2	Comparison of $K_S^0$ measurements from CERES and NA57 . . . . .	86
6.8.3	K to $\pi$ ratios . . . . .	87
6.8.4	$K^-$ to $K^+$ ratio . . . . .	88
6.8.5	Thermal model . . . . .	90
6.9	Discussion . . . . .	91
<b>7</b>	<b>Fast TRD development</b>	<b>93</b>
7.1	Motivation and requirements . . . . .	93
7.2	CBM experiment . . . . .	94
7.3	Basic properties of transition radiation and its detection . . .	95
7.4	TRD in the CBM experiment . . . . .	97
7.5	CBM TRD basic layout . . . . .	97
7.6	MC Simulations . . . . .	98
7.7	Results . . . . .	102
7.8	Simulations versus Data . . . . .	108
7.9	Discussion . . . . .	112
<b>8</b>	<b>Appendix - A -</b>	<b>113</b>
<b>9</b>	<b>Appendix - B -</b>	<b>123</b>
	<b>Bibliography</b>	<b>128</b>



# Chapter 1

## Heavy ion collisions

### 1.1 Introduction

Heavy ion collisions offer a unique opportunity to study in the laboratory the properties of strongly interacting matter under extreme conditions. The energy density reached in the central part of a nuclear collision at the SPS energy is  $4 \sim \text{GeV}/\text{fm}^3$  [1]. Such were the densities of the Universe only a few tenths of microsecond after the Big Bang. Particularly exciting is the expectation that beyond certain energy density and/or net baryon density - a new state of matter, a Quark Gluon Plasma (QGP), could exist [2] in which the baryons melt into quasi-free quarks and gluons.

To gain a deeper understanding of the processes taking place during a heavy ion collision is a challenge both in theory and experiment.

Historically the first heavy ion program aiming at the creation of QGP started in 1986 with fixed target experiments at the AGS (Alternating Gradient Synchrotron) at BNL and the SPS (Super Proton Synchrotron) at CERN with center of mass energies of  $\sqrt{s} = 5 \text{ AGeV}$  and  $\sqrt{s} = 17 \text{ AGeV}$ , respectively. First data were taken with beams of relatively light ions:  $14.6 \text{ AGeV } ^{16}\text{O}$  and  $^{28}\text{Si}$  at the AGS and  $60 - 200 \text{ AGeV } ^{16}\text{O}$  and  $^{32}\text{S}$  at the SPS. Later the program continued with heavier nuclei:  $10.8 \text{ AGeV } ^{197}\text{Au}$  at the AGS and  $40, 80, \text{ and } 158 \text{ AGeV } ^{208}\text{Pb}$  at the SPS. Based on the analysis of the Pb data at top SPS energies in the year 2000 CERN released an official announcement on discovery of new state of matter [3].

### 1.2 Hot and Dense Nuclear Matter

The world of high energy physics is described by means of particles and their interactions. For our purpose the main role is played by hadrons like

protons, neutrons, pions etc, composed of quarks that interact via strong interaction. Their properties and behavior are described by the theory of strong interactions, Quantum Chromodynamics (QCD). Quarks are fermions with spin  $\frac{1}{2}$  and come in six flavors;  $u$  (up),  $d$  (down),  $c$  (charm),  $s$  (strange),  $b$  (bottom), and  $t$  (top).

Apart from flavor the quarks are characterized by color (red, green and blue), spin, electric charge ( $1/3$  or  $-2/3$  of the elementary electric charge). The quark masses are free parameters of QCD. Each quark has its antiparticle - an antiquark. Strong interaction between two quarks is carried out by exchanging massless particles - gluons. The main difference of the strong interaction when compared to the electromagnetic (EM) interaction is that gluons in contrary to photons carry a charge of the strong interaction and interact among each other. This rather innocent feature of the strong interaction has serious consequences on the basic properties of the strong force. In contrary to the EM interaction the potential of the strong force  $V_S \sim r$  for larger distances. If two quarks are being pulled apart from each other the energy stored in the field may become large enough that it is energetically more favorable to create a new quark-antiquark pair. Measurable consequence is jet production in high energy particle collisions.

One of the main properties of QCD, known as confinement, is the rather intriguing property of quarks to form only colorless objects. It is a matter of fact that free quarks have never been experimentally observed. The two simplest possibilities of colorless (or white) objects formed by quarks are baryons (3 quarks) and mesons (quark - antiquark pairs). There are predictions for possible pentaquarks, glueballs, or hybrids but have not been observed experimentally yet.

Nuclear matter at the temperature and pressure typical to a nucleus contains only protons and neutrons. Neutron can be stable only when bound inside a nucleus. Now - what happens when two nuclei accelerated to relativistic energies collide? From both experiment and theory we know that such a system, even though for a very short period of time, can reach densities several times higher than the ordinary nuclear matter and its temperature may reach  $\sim 1$  GeV.

Lattice QCD predicts that at the critical energy density of  $\epsilon = 0.7$  GeV/fm<sup>3</sup> the degrees of freedom will change from hadrons to partons (Fig.1.1). In this state the matter will contain quarks and gluons not bound inside the hadrons, but moving freely over the volume of the system.

The two phases of the QCD can be best described in terms of temperature  $T$  and baryonic chemical potential  $\mu_B$ . The corresponding diagram presented in Fig. 1.2 is known as the QCD phase diagram. Different regions in the diagram are relevant to different physics fields and only a rather limited

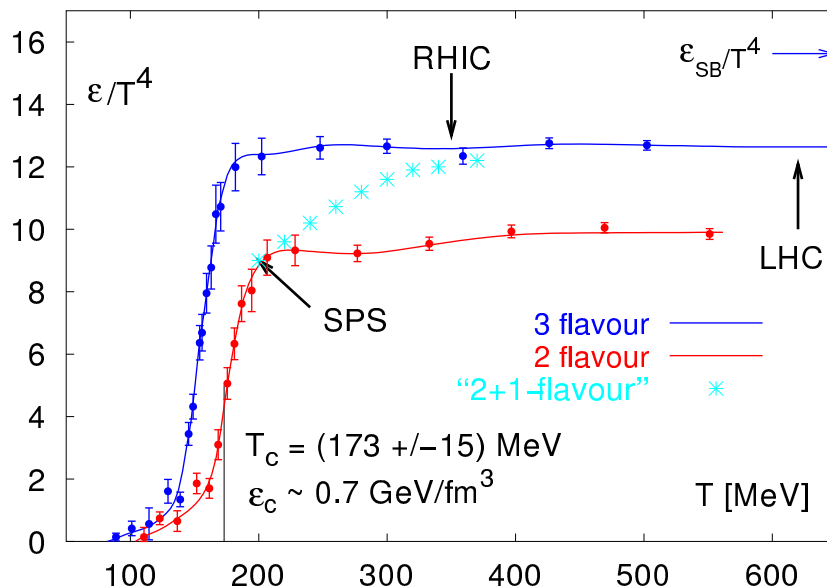


Figure 1.1: *Lattice QCD simulations: dependence of the normalized energy density on the temperature. A steep increase is observed around 173 MeV. [4]*

part of the  $T - \mu_B$  space can be accessed experimentally. The experimental points are extracted from the measured particle yields and interpreted with the thermal model to obtain the temperature of the system at the chemical freeze out (i.e. when the particle abundances are fixed) and from the SPS energies one gets very close to the proposed transition to QGP (lattice QCD calculation).

### 1.3 Evolution and Dynamics of a Heavy Ion Collision

A heavy ion collision evolves through four basic stages: hard scattering, thermalization, expansion and decoupling. In the very early stage of the collision, before the colliding particles lose most of their energy via multiple scattering, the "hard" particles either with large mass or transverse momenta  $p_T \gtrsim 1$  GeV/c are created. If such a hard particle is created near the edge of the reaction zone and moves inwards of the developing fireball it will - thanks to the transverse size of the Pb-Pb reaction zone of about 12 fm - probe the whole process of thermalization, expansion and cooling until it emerges on

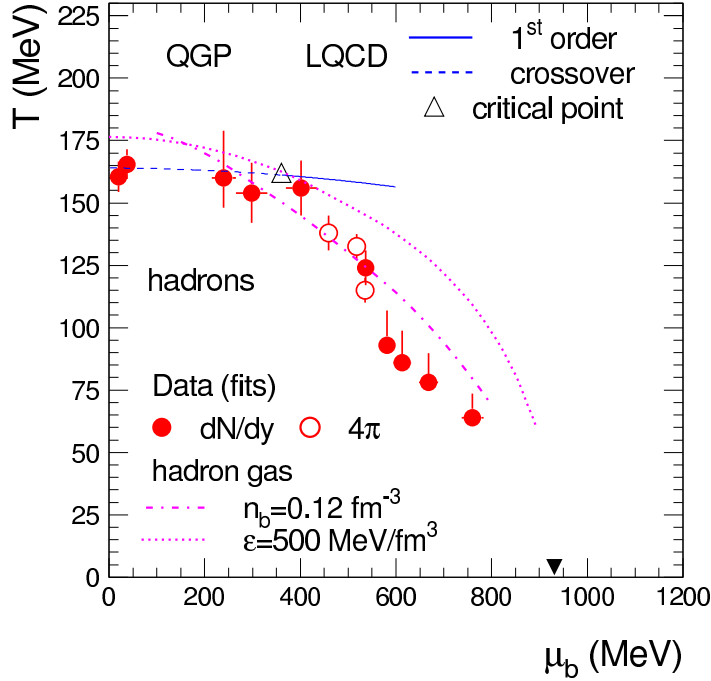


Figure 1.2: QCD phase diagram [5]. Red points represent data results from SIS, AGS, SPS and RHIC.

the other side. The in medium modifications (or even destruction) of such a hard probe can tell us more about the properties of the medium itself.

Thermalization (i.e. thermal equilibrium) in a strongly interacting, highly dynamical and very fast developing (expanding) system is indeed a non trivial observation, but the data on particle spectra and flow strongly support very fast thermalization times of  $\tau \lesssim 1 \text{ fm}/c$  [6], [7].

Pressure gradient of a thermalized system leads to collective (hydrodynamical) expansion to surrounding vacuum. The fireball cools down as its energy density decreases. If in the early stage of the collision matter with partonic degrees of freedom was created then once the energy density during the expansion drops below  $1 \text{ GeV}/\text{fm}^3$  the partons convert to hadrons and the whole system undergoes a phase transition. This leads to a steep drop of the entropy density over a small temperature interval. Since the entropy cannot decrease - the temperature of the fireball remains rather unchanged



while the volume increases. Once the temperature of the fireball decreases to the level that inelastic collisions do not occur anymore, the system reaches chemical freeze out, as the particle yields are fixed and the only processes that modify the yields are the decays of resonances. Still the elastic collisions modify the spectra of the particles. Below a certain temperature the system is so dilute that also the elastic collisions cease (kinetic freeze out), the particles move freely without further interactions.

Important for the characterization of a particular heavy ion collision is the centrality of the collision. According to the spectator-participant model [8] the nucleons from the overlapping region of the two colliding nuclei form a fireball while the rest of the nucleons move away basically undisturbed. The centrality of the collision is defined by the impact parameter  $b$  which is basically the transverse (to the beam) distance between the centers of the nuclei prior to the collision. The impact parameter  $b = 0$  means the most central collision and the impact parameter  $b = r_1 + r_2$  ( $r_1$  and  $r_2$  are the radii of the colliding nuclei) would mean the most peripheral collision.

The impact parameter is not directly measurable. To determine the geometry of the collision measurements of quantities that are strongly correlated to the number of participants are used, such as the number of produced tracks or transverse or forward energy.

Using the Planck units convention ( $\hbar = c = 1$ ) the transverse energy measured in the experiment is defined as:

$$E_T = \sum_{i=1}^n (m_T)_i \quad (1.1)$$

where the  $n$  is number of particles measured and  $m_T$  is the transverse mass:

$$m_T = \sqrt{m^2 + p_T^2} \quad (1.2)$$

where  $p_T$  is the transverse momentum of given particle,  $p_T = p \cdot \sin(\theta)$ , where  $\theta$  is a polar angle in respect to the beam direction.

However a more common approach of measuring the  $E_T$  is based on the measurement of the total energy of the particle  $E$  together with the angle  $\theta$ . The  $E_T$  is then defined as:

$$E_T = \sum_{i=1} E_i \cdot \sin \theta \quad (1.3)$$

where the sum runs either over all particles or corresponds to the cell of the calorimeter.

In principle the particles produced in a nucleus-nucleus collision could be described by their transverse momenta  $p_T$  and polar angles  $\theta$ . More common is to use the transverse momentum and the *rapidity* of the particle. Rapidity  $y$  of a particle is defined as:

$$y = \frac{1}{2} \ln \frac{E + p_z}{E - p_z} \quad (1.4)$$

where  $E$  is energy of the particle and  $p_z$  is the longitudinal momentum.

This variable has interesting properties. Lorentz transform in the longitudinal (beam) direction where  $p'_T = p_T$ , becomes particularly simple:  $y' = \Delta y + y$ .

The energy density reached in a heavy ion collision can be estimated from the transverse energy according to Bjorken formula [9]:

$$\epsilon = \frac{1}{\pi R^2 \tau} \frac{dN}{dy} \langle E_T \rangle \quad (1.5)$$

where  $\langle E_T \rangle$  is the mean transverse energy per particle,  $dN/dy$  is the particle density,  $\tau$  is the formation time and  $\pi R^2$  is the transverse area of the reaction zone. Formation time can not be measured experimentally and is usually estimated to be  $\sim 1$  fm/c. Energy densities at top SPS energy reach values of  $\sim 3$  GeV/fm<sup>3</sup>.

## 1.4 Probes and observables (how to find the QGP)

Obtaining a complete and self consistent description of heavy ion collisions requires understanding properties and dependencies of many processes taking place in course of the reaction. From an experimentalists point of view this means to measure many observables which then can be interpreted within theoretical models.

Whatever processes take part in a heavy ion collision we can only measure the particles that escape to "infinity" and reach the detectors. Indeed, most of the particles we measure were produced in the hadronization stage of the collision and undergo elastic collisions until the kinetic freezeout. This complicates the access to properties of the fireball prior to hadronization. Still,

the properties of the particles produced reflect to some degree the properties of the medium prior to hadronization.

To study the properties of the dense and hot nuclear matter produced in heavy ion collision and to search for QGP, specific probes (taken from ref. [5]) have been proposed [9–12] and are currently studied: i) direct photons [13], ii) low mass dileptons [14], iii) strangeness [15, 16]; iv) charmonium suppression [17], v) jet-quenching [18–24], vi) fluctuations [25, 26].



# Chapter 2

## Strangeness production in nuclear collisions

### 2.1 Introduction

There are several reasons why particles containing strange quarks are interesting observables in heavy ion collisions. The strange quarks (or anti-quarks) are not present in the colliding nuclei prior to collision and therefore all strange quarks and antiquarks observed are produced during the collision itself.

The bare mass of a strange quark  $m_S = 95 \pm 25 \text{ MeV}/c^2$  [27] is of the same order of magnitude as temperature of the fireball and thus the strange particle yields and transverse momentum spectra are sensitive to the details of the reaction mechanism.

Already in 1982 it was noticed [28] that strange particles are an interesting probe for the heavy ion collisions as their production was expected to be sensitive to the properties of the fireball.

Shortly after the importance of strangeness (and its enhancement compared to nucleon-nucleon collisions) in heavy ion collisions was emphasized by Rafelski and Müller [29] who linked the strangeness enhancement (in heavy ion collisions in comparison to scaled proton-proton collisions) to possible transition of hadronic to partonic matter in the evolution of the fireball. It was also proposed that the production of strange quarks in QGP is dominated by a gluon-gluon fusion.

Although later it became clear that the strangeness enhancement itself should not be considered as QGP "smoking gun" because it is also observed at energies that do not suffice to reach the conditions of possible QGP creation [16], the strangeness enhancement signals the production of not yet well

understood QCD states of matter.

## 2.2 Existing results

Strangeness enhancement was for the first time measured in 1990 at SPS energy by NA35 [30] with 200 AGeV  $^{32}\text{S}$  beam on  $^{32}\text{S}$  target. It was shown that multiplicities of neutral strange particles ( $\text{K}^0$ ,  $\Lambda$  and  $\bar{\Lambda}$ ) relative to negative hadron multiplicities grow as a function of centrality when compared to proton - proton data. For the most central collisions the enhancement reached about a factor 2.

As observed later by WA97 in 158 AGeV Pb+Pb collisions [31] the enhancement depends on the strangeness content, growing approximately linearly with the number of strange quarks.

Apart from the production yield of the strange particles, the ratio of strange to non-strange particles and its energy dependence gained a lot of interest in the recent years. The mid-rapidity  $\text{K}^+/\pi^+$  and  $\Lambda/\pi^-$  ratios (Fig. 2.1) show a pronounced peak at the collision energy of  $\sqrt{s} \sim 7$  GeV. This was originally predicted in 1999 [32] with the Statistical Model of early Thermalization (SMET) as a very sharp peak (later addressed as "horn") - a direct consequence of transformation from dense hadronic matter to QGP. The data measured later by NA49 [33, 34] show a non monotonic dependence of the  $\text{K}^+/\pi^+$  on the collision energy. Indeed a thermal model without an explicit phase transition does predict a "bump" at the same energy range (shown in Fig. 2.1). The "horn" versus "bump" is being currently strongly debated [5]. The experimental situation does not allow for a strong conclusion. More measurements are needed to shed more light on this interesting issue. This topic was the main argument for an analysis of charged kaons presented in this thesis as it is based on different kaon reconstruction strategy and has therefore different systematics.

An important information can be extracted from the transverse mass ( $m_T$ ) spectra. Measured  $m_T$  slopes show even at SPS energies rather precise baryon - antibaryon universality, even though at CERN SPS energies significant baryon number asymmetry exists. This was first shown in S - W collisions by the WA85 experiment [35] and was later confirmed by WA97 in Pb - Pb collisions [36] and later by NA57 [37-39] and NA44 [40]. The identity of strange baryon and antibaryon effective temperature is a strong argument that they are produced by the same mechanism and do not suffer re scattering in a dense baryon rich medium after their production [15].

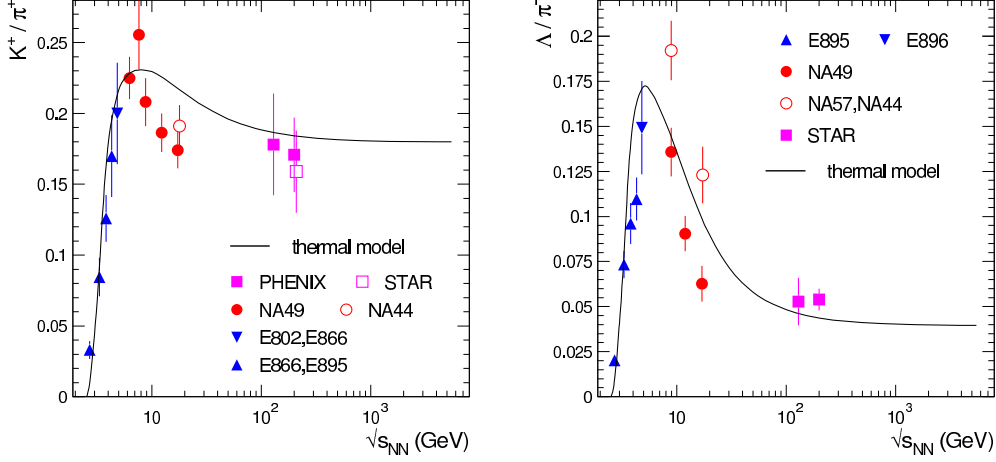


Figure 2.1: *Excitation functions for the  $K^+/\pi^+$  ratio (left) and the  $\Lambda/\pi^-$  ratio (right) [5]. Lines are thermal model calculations.*

## 2.3 Strangeness in CERES

Although the CERES experiment was built to study low mass vector mesons [41, 42] via dileptonic decays, the upgrade with a large radial TPC allowed to measure a wide range of hadronic observables.

Rather unique measurement of the  $\phi$  meson [43] in both leptonic and hadronic channels  $\phi \rightarrow e^+e^-$ ,  $\phi \rightarrow K^+K^-$  (see Fig. 2.2) allowed to solve the so called  $\phi$  puzzle that consisted in a large disagreement between measurements of NA49 (in hadronic channel) and NA50 (in leptonic channel).

An analysis of  $K_S^0$ ,  $\Lambda$  and  $\bar{\Lambda}$  was made within the framework of the PhD thesis of Sylwester Radomski [44]. The measured rapidity spectrum of the  $K_S^0$  and its comparison to the NA49 measurements is shown in Fig. 2.3.

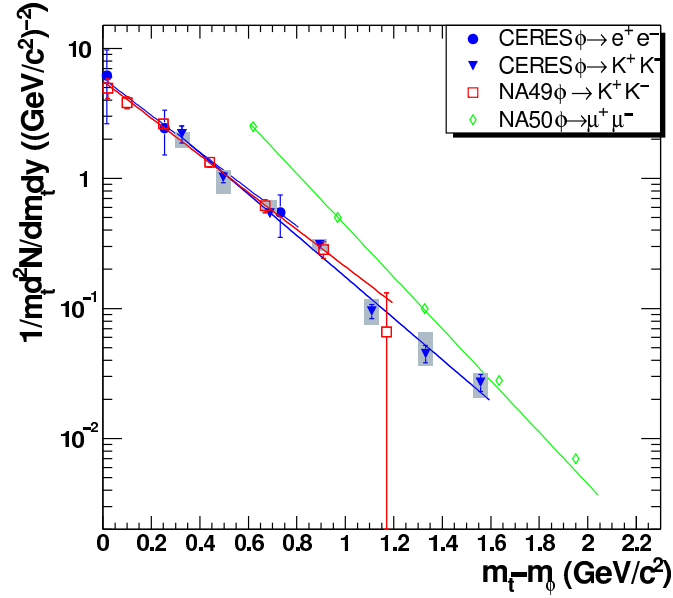


Figure 2.2: *CERES*  $\phi$  meson transverse mass spectra in leptonic and hadronic channels compared to results from NA49 and NA50 [43].

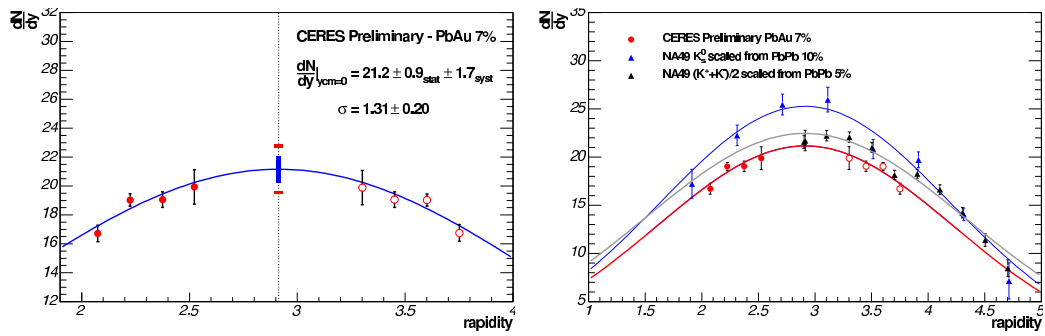


Figure 2.3: *Left*:  $K^0$  rapidity distribution. *Right*: comparison to the NA49 experiment [44].



# Chapter 3

## NA45/CERES experiment

The CERES (Cherenkov Ring Electron Spectrometer) belonged to the second generation of heavy ion experiments at CERN SPS. It was primarily designed to measure  $e^+e^-$  pairs in nucleus-nucleus collisions. CERES detector was operated between 1992 - 2000. During this period the detector did undergo several upgrades. The last one took place in 1998 when a large TPC (Time Projection Chamber) replaced the Pad Chamber to improve the mass resolution in the region of  $\rho, \omega$ , and  $\phi$ . Also, the  $dE/dx$  information could be used to further improve the electron-pion separation. TPC also opened new possibilities for hadronic studies [45] including the topic of this thesis. The spectrometer covers full azimuthal angle and  $8^\circ < \theta_{lab} < 15^\circ$ . During the last upgrade the magnetic system around RICH detectors was disabled and new magnetic system around TPC was installed. The schematic view of the CERES setup after this upgrade is shown in Fig. 3.1.

### 3.1 Target area and trigger setup

As shown in Fig. 3.1 the beam enters from left and passes through the target composed of 13  $25 \mu\text{m}$  thick gold discs separated by 2mm. The geometry of the target was chosen such that the particles produced in heavy ion collision within the acceptance do not cross another target disc. The segmentation of the target reduces the  $\gamma \rightarrow e^+e^-$  conversions and thus reduces the background for the electron analysis.

The CERES trigger system (not shown in the figure) was composed of several dedicated trigger detectors including the Cherenkov counters BC1, BC2 and BC3 used to define the beam trigger and one plastic scintillator MC for centrality determination.

The Beam trigger is defined as a coincidence of two Cherenkov counters

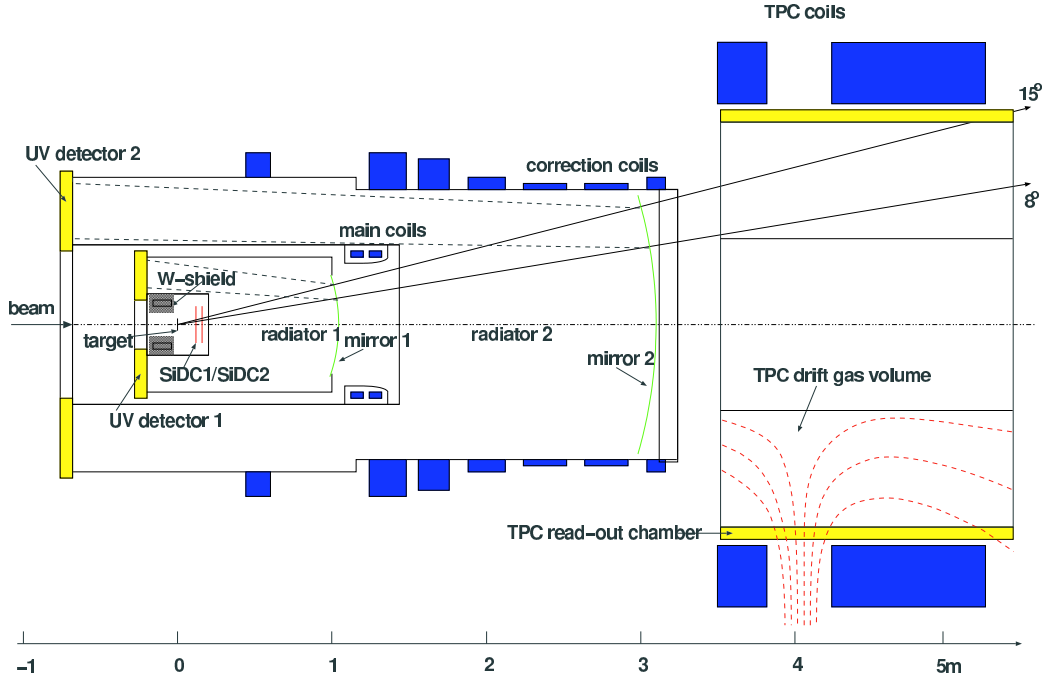


Figure 3.1: Schematic view of the CERES detector.

placed upstream the target:

$$T_{Beam} = BC1 \cdot BC2 \quad (3.1)$$

With the additional anti coincidence with the Cherenkov counter placed just after the target the minimum bias trigger is defined as:

$$T_{mb} = BC1 \cdot BC2 \cdot \overline{BC3} \quad (3.2)$$

The central trigger required a signal from the MC. The MC scintillator had thickness of 1mm and had pseudorapidity coverage of  $2.3 < \eta < 3.5$ . Its signal is roughly proportional to number of particles hitting it and thus it is suitable for centrality measurements.

$$T_{central} = BC1 \cdot BC2 \cdot \overline{BC3} \cdot MC \quad (3.3)$$

Additional beam particles passing the target within several microseconds from the triggered event are source of  $\delta$  electrons. These were suppressed by the trigger system within  $\pm 1 \mu s$  from the triggered nuclear reaction.

## 3.2 Silicon Drift Detectors

Precise vertex reconstruction is carried out by two Silicon Drift Counters SD1 and SD2 (technique proposed by authors of [46]) placed 10.4 and 13.3 cm downstream from the target and covering radii from 4.5 to 42 mm. The SiDC detectors are read out by 360 radially arranged anodes. Besides the vertex reconstruction and tracking the SiDC detectors also measure the pseudorapidity density of charged particles  $dN/d\eta$  [47]. The  $dE/dx$  information from the SiDC detector was used to recognize and suppress close  $e^+e^-$  pairs from  $\gamma$  conversions and  $\pi^0$  Dalitz decays.

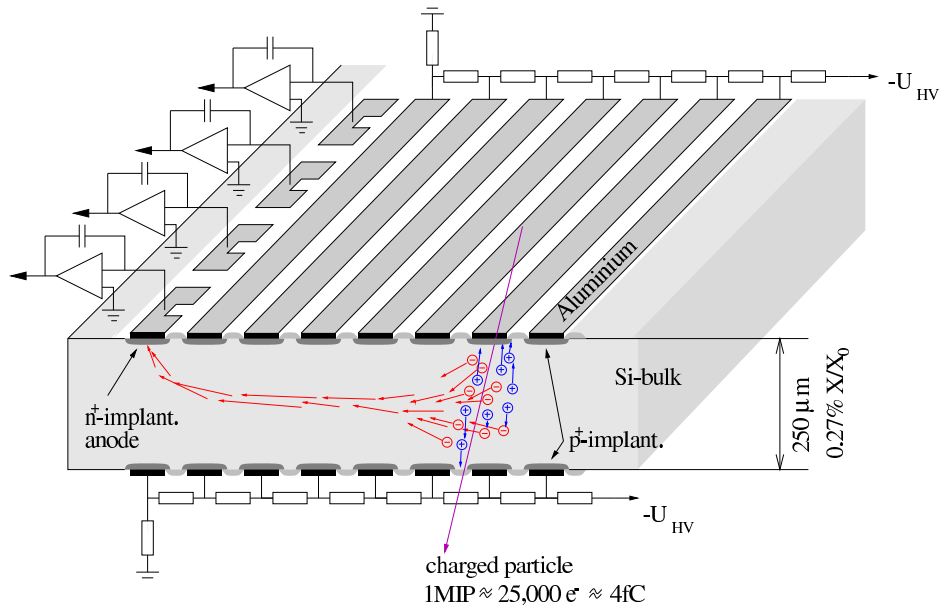


Figure 3.2: Schematic view of a silicon drift detector.

The principle of operation of a silicon drift detector is shown in Fig. 3.2. Electrons produced by charged particle drift towards the read out anode placed on the outer edge of the detector. The drift field is created by a voltage divider on the surface of the wafer. The maximal drift time is about  $3.8 \mu\text{s}$  with a drift field of  $700 \text{ V/m}$ . Small area of the read out anode which implies small capacitance and therefore lower noise, is one of the advantages of this concept.

### 3.3 RICH Detectors

The main task of the Ring Imaging Cherenkov Detectors RICH1, RICH2 is the electron identification. Cherenkov radiation is emitted by charged particles moving faster than the speed of light in a given medium and has a velocity dependent angle:

$$\theta = \arccos\left(\frac{1}{\beta n}\right) \quad (3.4)$$

The photons produced in the radiator are reflected by a spherical mirror onto a ring of radius  $R$  on position sensitive photon detector. By measuring the radius of the projected ring the Lorentz factor  $\gamma$  of the particle can be determined:

$$R = R_\infty \sqrt{1 - \left(\frac{\gamma_{th}}{\gamma}\right)^2} \quad (3.5)$$

where the  $R_\infty$  is radius for particles with  $\gamma \gg \gamma_{th}$  and is defined by the focal length  $f$  of the mirror and the  $\gamma_{th}$ :

$$R_\infty = f \cdot \frac{1}{\gamma_{th}} \quad (3.6)$$

For practical purposes the radius of the ring produced by electron has the value of  $R_\infty$ .

Both Cherenkov detectors have methane  $\text{CH}_4$ , at atmospheric pressure as the radiator gas. Threshold factor of  $\gamma_{th} = 32$  assures hadron blindness of the detector up to pions with momentum 4.5 GeV. The Cherenkov photons are detected by multiwire proportional chambers filled with a He/ $\text{CH}_4$  (94/6) mixture at atmospheric pressure. The conversion of the photons is done via photo-ionization of TMAE (Tetrakis-di-Methyl-AminoEthylen) vapor with a low ionization potential of 5.4 eV.

### 3.4 Time Projection Chamber

The main tracking detector of the upgraded CERES setup is the radial TPC (Time Projection Chamber) located 3.8 m from the target system. Apart from tracking and momentum measurement additional particle identification via specific ionization is possible. Fig. 3.3 shows schematic view of the detector. The sensitive volume is filled with a gas. Charged particles traversing

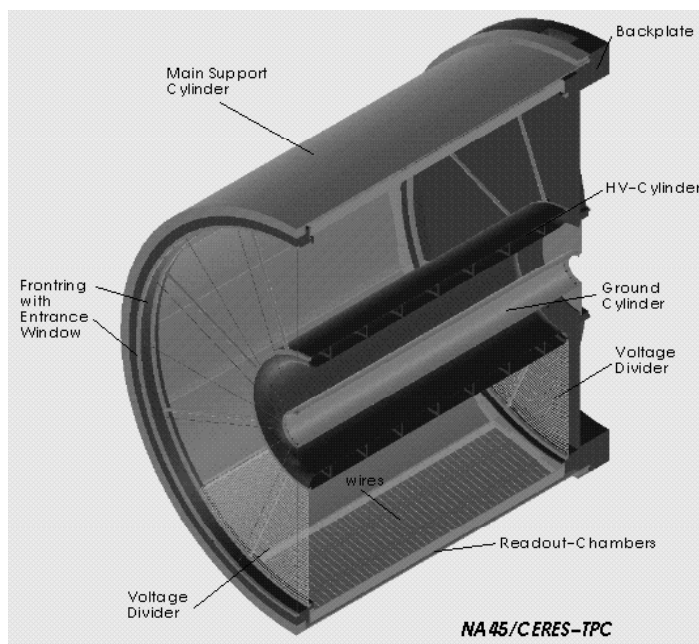


Figure 3.3: *Schematic view of the CERES TPC*

the gas ionize its atoms. Liberated electrons drift in a radial electric field outwards toward the readout chambers located on the outer shell of the cylinder. In the vicinity of the anode wires, due to strong non homogeneous electric field, these electrons are accelerated and produce secondary ionization in an avalanche process. The electrons liberated in the avalanche are produced very close to the anode wires and are collected very quickly. Therefore they induce very small signal. The main part of the signal is induced by the ionized gas atoms which drift towards cathode wires and padplane. The total 3D information about the position of the interaction of the charged track is obtained from the time of the drift of the primary electrons (1 dimension) and the read out pad plane (2 dimensions). The information about the momentum of the track is then reconstructed from the curvature of the track in the magnetic field.

The detector itself has an active length of 2 m. The inner radius is 48.6 and the outer radius 130 cm. The signal readout is provided by 16 MWPCs (Multi Wire Proportional Chamber). Each chamber covers  $22.5^\circ$  in azimuth. Within one chamber the read out itself is done via a segmented cathode (pad plane). Each chamber has 48 pads in azimuthal direction. In the beam direction the TPC is divided in 20 planes. The  $16 \times 48 \times 20 = 15360$  readout

channels are sampled in 256 time bins.

The electric field is radial and points from the central electrode towards the read out chambers. The voltage applied to the central electrode is -22.9 kV. Both ends of the TPC are closed by capton foils with voltage dividers to assure homogeneity of the field. TPC is operated in a semi-radial magnetic field generated by several solenoids.

The sensitive volume of the TPC is filled with a Ne/CO<sub>2</sub> gas mixture with ratio 80/20 at atmospheric pressure. This composition was chosen taking into account several factors. One of the main concerns was to keep the Lorentz angle (finite angle between the directions of the electron drift velocity and the electric field caused by non parallelism of magnetic and electric field lines) small; this required a gas with low mobility. The maximal drift time was 70  $\mu$ s. Another aspects like the total radiation length, the number of created electron-ion pairs, and diffusion were also taken into account.

### 3.5 Tracking

At this point it is important to explain the nomenclature of the CERES tracking. As mentioned already CERES experiment is a dedicated dielectron spectrometer. As all of the light vector mesons ( $\phi, \eta, \rho$ ) have very short lifetimes - their decay products do not differ (geometrically speaking) from the primary tracks created during the collision. The tracking system was tuned to this situation as well as were the basic track parameters.

During the tracking procedure following stored variables are important for the analysis:

- $pcor2$  : momentum obtained from a 2 parameter fit which assume that the track comes from the event vertex.
- $pcor3$  : momentum obtained with a 3 parameter fit without the constrain mentioned above.
- $pcomb$  : combined momentum of  $pcor2$  and  $pcor3$  obtained as weighted average of the  $pcor2$  and  $pcor3$ . In all 3 cases the sign of the momentum keeps the information about the charge of the track.
- $\theta R2M$  : theta of the TPC track projected to the position of the mirror of the second RICH detector (R2M) placed 330 cm from the target. It is assumed that the track comes from target (see Fig. 3.4).
- $\phi R2M$  : phi of the TPC track projected the same way as the  $\theta R2M$ .

- $Xline0, Yline0$  : offsets of the TPC track in the transverse plane at  $Z = 0$  cm (center of the target in the TPC coordinates) - see Fig. 3.5.
- $Xline1, Yline1$  : slopes of the TPC track in the  $xz$  and  $yz$  planes.
- $NHits$  : number of hits on the track.
- $NFitHits$  : subset of hits from the  $NHits$  that was used for the track fitting.

The variables  $Xline1, Yline1$  serve to compute the so called *local* angles of the TPC track in the following way:

$$\theta_L = \arctan(Yline1/Xline1) \quad (3.7)$$

$$\phi_L = \arctan(\sqrt{Xline1^2 + Yline1^2}) \quad (3.8)$$

A track defined by local angles, track offsets and momentum can be subsequently used for secondary vertex analysis and kaon reconstruction.

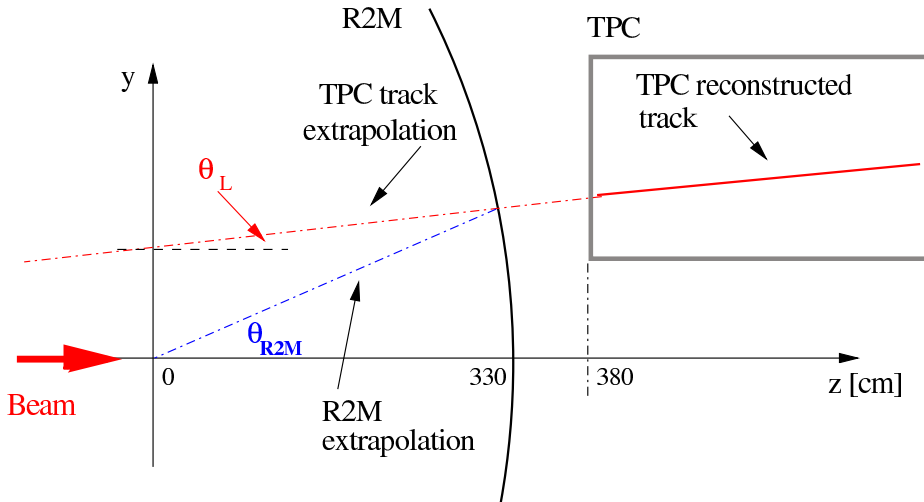


Figure 3.4: Local and R2M angles (for polar angle  $\theta$ ) in CERES experiment. For simplicity only one half of the TPC in the  $yz$  cross section is shown. 0 denotes the target position

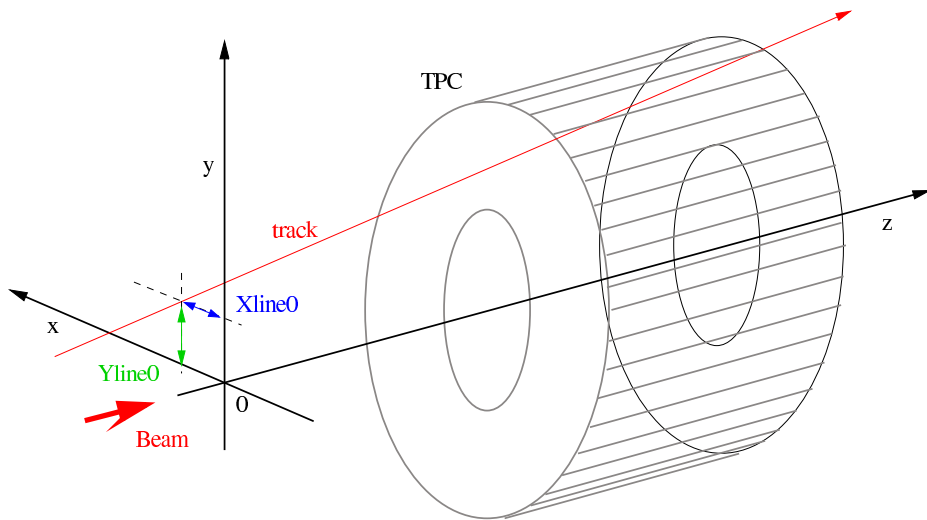


Figure 3.5: TPC track offsets in  $X$  and  $Y$  directions at  $Z = 0$  (in the middle of the target).



# Chapter 4

## Analysis of the $K^+$ and $K^-$

This chapter describes in detail the analysis of the charged kaons via their 3 body decay into charged pions with the CERES experiment using the high statistics run taken in 2000 with 158 AGeV Pb beam on the Au target. Detailed Monte Carlo (MC) study is described in the following chapter.

### 4.1 Charged kaons and CERES - basic facts

The rather large value of the lifetime of charged kaons ( $c\tau = 3.71\text{m}$ ) allows in most cases for a direct measurement. Common way to identify charged kaons is via momentum measurement together with the time of flight and/or  $dE/dx$  measurement. While with CERES setup the former is accomplished with the TPC, the time of flight measurement of the latter is not possible and the  $dE/dx$  resolution is not sufficient for a direct reconstruction. Therefore charged kaons can be reconstructed and identified only via their decay.

Dominant decays of  $K^+$  ( $K^-$  decays are just charge conjugates) are listed in the table 4.1. The only decay with branching ratio larger than 1% that goes entirely into charged particles is the decay into 3 charged pions. The most probable decay ( $K^+ \rightarrow \mu^+ + \nu_\mu$ ) involves neutrino and therefore could be only observed as a kink on the track and would have to happen inside restricted part of the active volume of the TPC to allow the reconstruction of the track of the incoming kaon and outgoing muon. Although possible, such a configuration of the tracks inside the CERES TPC would require separate track finding procedure and would suffer from the shape of the magnetic field.

The analysis presented in this thesis describes the reconstruction of charged kaons via their decay into 3 charged pions.

Although the multiplicity of  $K^+$  per rapidity unit at mid rapidity mea-

decay mode	branching ratio [%]
$\mu^+\nu_\mu$	$63.44 \pm 0.14$
$\pi^+\pi^0$	$20.92 \pm 0.12$
$\pi^+\pi^+\pi^-$	$5.59 \pm 0.031$
$\pi^0e^+\nu_e$	$4.98 \pm 0.07$
$\pi^0\mu^+\nu_\mu$	$3.32 \pm 0.06$
$\pi^+\pi^0\pi^0$	$1.76 \pm 0.024$

Table 4.1: *Dominant decays of the  $K^+$ . Rest of the known decays are below 1% level [27].*

sured by other experiments [33, 48] is rather large of  $dN/dY \sim 30$ , small branching ratio, large decay length ( $c\tau \sim 15\text{m}$  in the lab coordinates) and narrow acceptance of the CERES setup imply strong suppression factors and require a careful reconstruction procedure.

## 4.2 Reconstruction strategy

As mentioned in the previous chapter, only the TPC information is used to reconstruct the charged kaons via their decay into 3 charged pions. This decision was based on the fact that most of the kaon decays happen behind the first SiDC and therefore TPC - SD matching would have to be applied in the anti-matching mode (to suppress the tracks coming from the primary vertex) as most of the pion tracks originating from the kaon decay should not match to a SiDC track. However, as a large fraction of the pions have momentum below 1 GeV/c, random miss matches would be unavoidable what would yield to suppression of the signal. Also - from the point of the simulations, it is difficult to reproduce the SD - TPC anti-matching resulting in increase of the total systematical error. For this reasons it was decided to use the TPC information only.

### 4.2.1 Data and event selection

Data selection was made both on the level of selecting the events with required properties (centrality, separation to other events etc.) and analysis cuts - together with phase space cuts.

Main part of the event selection cuts apart from the cuts applied during the data taking consists of the beam and trigger cuts, centrality cuts and multiplicity in the TPC.

First cut on the event selection comes from the beam triggers BC1 and

BC2. Their signal distributions were calibrated during the step0 production to be centered at 0 and their width equal to  $\sigma = 1$ . The cut was placed at  $B = \pm 4$  in the following way to account for double events [49]:

$$BC1 * BC1 + BC2 * BC2 \leq 4 * 4 \quad (4.1)$$

To prevent overlapping events in the TPC a cut on the time to preceding and following interval is necessary. Already during the data taking this cut of  $\Delta t = 1\mu s$  was applied to all events, with the exception of the first few data units, what can be seen in the Fig. 4.1. During the analysis a cut value of  $\Delta t = 1\mu s$  was applied to account for this missing cut.

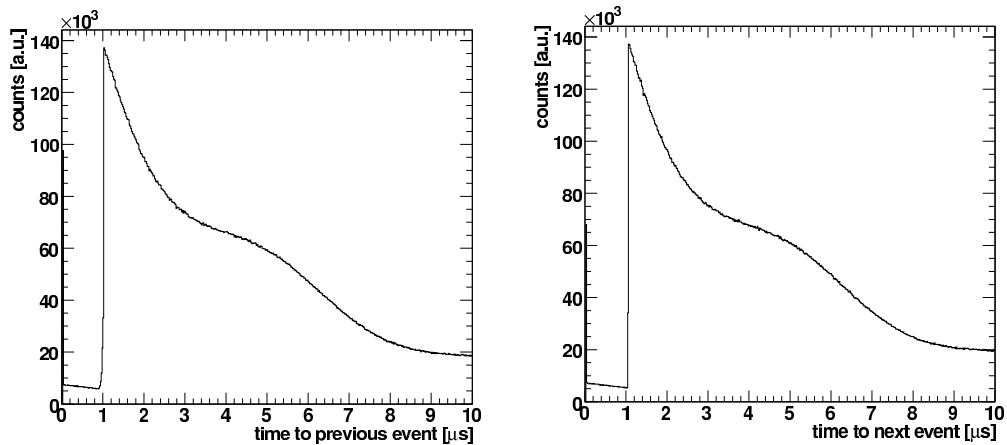


Figure 4.1: *Time to the previous (left) and time to the next (right) event. The cut value of  $1\mu s$  applied during the data taking to the most of the events is clearly visible.*

### 4.2.2 Centrality and multiplicity

An intuitive way to define the centrality is via the impact parameter  $b$  which is defined as transverse distance of the centers of the two colliding nuclei. However it is not directly measurable and one needs to find a different method based on a measurable observable that can be related to the impact parameter.

One possibility is to use a Zero Degree Calorimeter (ZDC) to measure the spectators of the collision directly and then use some model to relate the measured values to the impact parameter.

Another possibility is to assume that the energy dissipated in the collision reflected in the total multiplicity is a measure of centrality. This approach was used in CERES experiment. The nearly linear response of the Multiplicity Counter (MC) to the number of tracks within its acceptance allowed for multiplicity measurement.

The centrality (in %) is defined as a fraction of the geometrical cross section defined from minimum bias events as follows:

$$f_{\sigma}(M) = \int_M^{M_{MAX}} \frac{n(M)}{N} dM \quad (4.2)$$

where  $f_{\sigma}(M)$  is the fraction of the geometrical cross section for a given cut on the multiplicity  $M$ ,  $n(M)$  is number of events with given centrality  $M$  and  $N$  is the total number of events in the minimum bias sample.

It is important to realize that to measure the centrality one does not have to measure the total multiplicity. Still a reasonable coverage is needed to minimize the statistical fluctuations of the number of tracks.

In CERES the multiplicity was measured by the Multiplicity Counter, the TPC and the SD. For this analysis a cut on calibrated MC centrality of 7% was applied. The MC centrality and the correlation of the MC and TPC centrality before the event cuts are shown in 4.2.

TPC multiplicity before and after trigger and MC centrality cuts is shown in 4.3 . To suppress the possibility of two events overlap an upper cut on the TPC multiplicity of 500 was applied.

In total 24.3M events were accepted for the analysis from the total 31.7M events.

### 4.2.3 Analysis cuts

To reconstruct the charged Kaons from the CERES data one could - at least from principle point of view - make 3 particle combinations and carefully subtract background obtained via mixed event technique. However practically it is not possible as 3 track combinations would yield into  $\sim 10^6 - 10^7$  combinations per event with total computing time of several years and signal to background ratio of  $S/B \sim 10^{-7} - 10^{-8}$ .

To overcome this technical problem rather strong cuts need to be applied already at the single track level to decrease the combinatorial background while keeping the kaon signal. The analysis cuts include in addition to single track cuts also pair cuts and cuts on 3 particle combinations (triplet cuts).

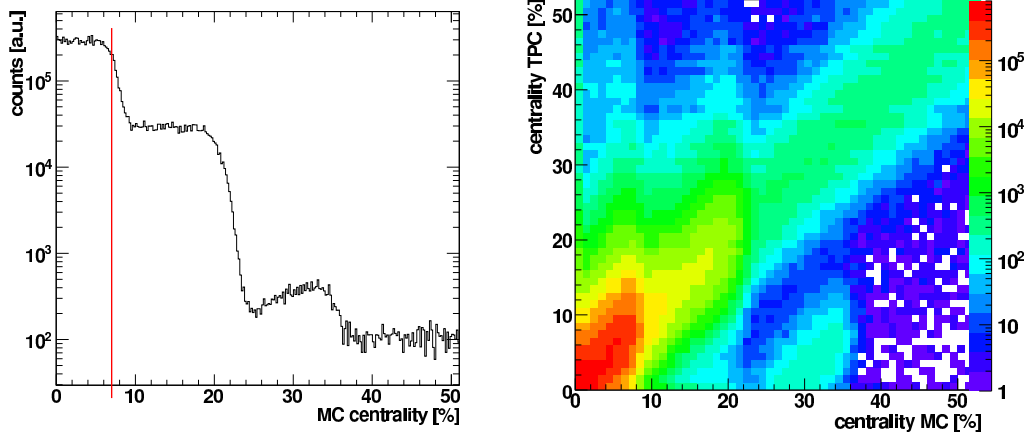


Figure 4.2: *Left: MC centrality. The structure of the distribution reflects different settings of the centrality trigger during the data taking. The red line shows the cut value of 7%. Right: The TPC versus MC centrality.*

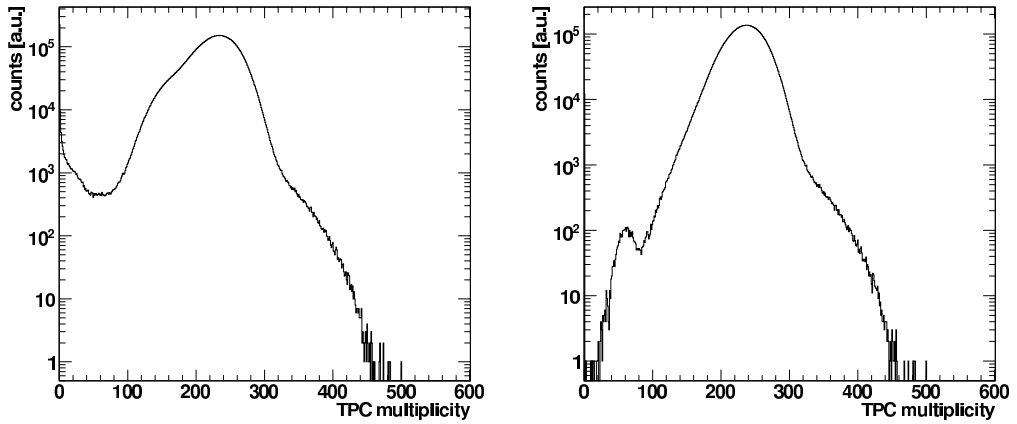


Figure 4.3: *TPC multiplicity before (left) and after event selection and centrality cuts (right).*

### 4.3 Analysis cuts

In this part a brief description of the analysis cuts is given. The values of the cuts are mentioned, but more detailed discussion on their values is shown in the chapter dedicated to Simulations (see Sect. 5).

### 4.3.1 R0 cut

The R0 cut is the most powerful cut for the combinatorial background suppression. It is a cut on the transverse distance of a TPC track in the event vertex plane (see Fig. 4.4). TPC tracks of most of the primary tracks produced during the Pb+Au collision in one of the target discs point back to event vertex in the transverse plane within a few cm. Cutting these tracks away suppresses most of the primary tracks and makes the subsequent 3 track combinations feasible. Of course this influences the kaons as well as there is a chance that one of the daughter pions will point close to the event vertex. As it will be shown in the Simulation chapter this cut suppresses practically all kaons decaying closer than 1.5 m to the event vertex.

The value of the R0 cut is computed as follows:

$$R0 = \sqrt{Xline0^2 + Yline0^2} \quad (4.3)$$

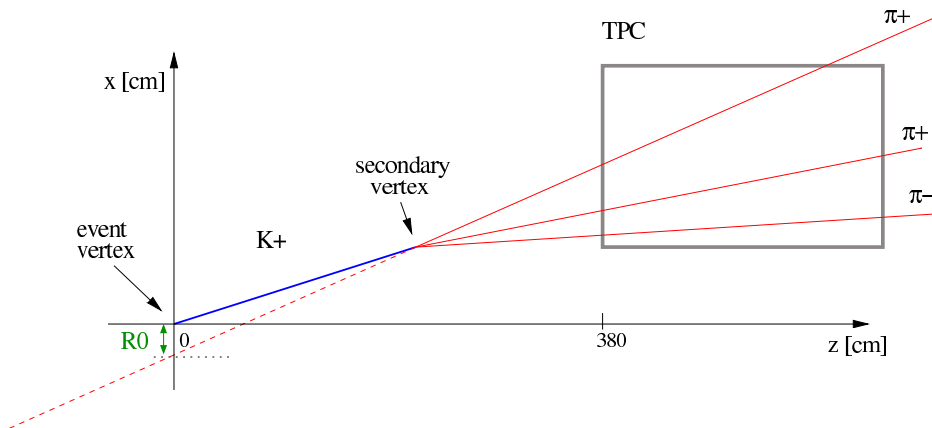


Figure 4.4: Schematic view of the CERES TPC and event vertex in the  $x,z$  plane.

### 4.3.2 Number of hits cut

The CERES TPC is readout-wise divided into 20 planes along the  $z$  axis. This means one track may have up to 20 TPC hits. Indeed the more hits the track has the better will be the determination of its parameters. In this analysis, a cut value of minimum 10 hits on track was required.

### 4.3.3 $dE/dx$ cut

While the CERES setup was not dedicated to hadron physics and the particle identification, was concentrated on electron identification it is still possible to suppress most of the electrons and low momentum protons with a cut on the energy deposition in the TPC. This cut is momentum dependent. The main benefit is the suppression of the conversion  $e^+ e^-$  pairs that occurs mainly in the RICH2 mirror and the front support wheel of the TPC.

### 4.3.4 $\Delta\phi_{R2M}$ cut

This cut relates the azimuth angles of two tracks and it is based on the two basic facts. In the first place - the mass of 3 pions is only by  $\sim 75 \text{ MeV}/c^2$  smaller than the mass of the charged kaon. This implies that even rather modest boost of  $\beta\gamma \sim 5$  the 3 pion tracks form rather narrow cone. Second important point can be seen in the Fig. 4.5. Thanks to the fact that kaons decay far from the primary event vertex (target) the  $\Delta\phi_{R2M}$  is smaller than the  $\Delta\phi_{Local}$ .

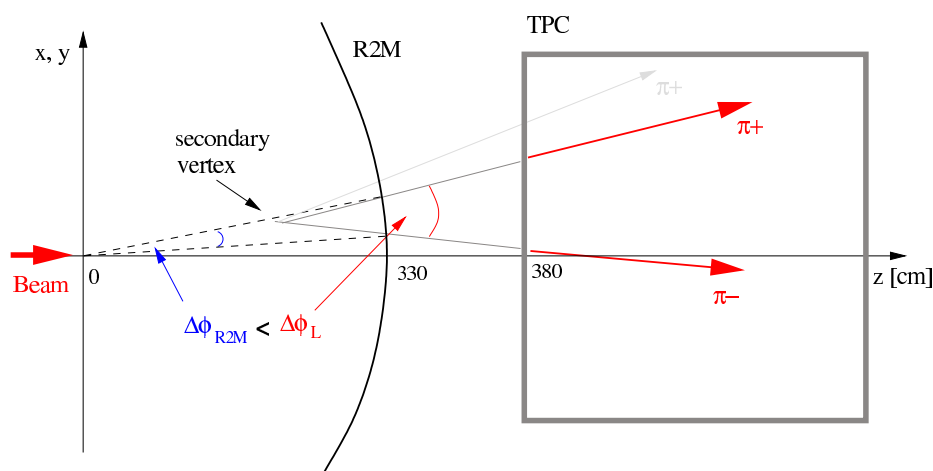


Figure 4.5: Schematic of the the CERES setup including the TPC RICH2 mirror and an event vertex.

$\Delta\phi_{R2M}$  is defined as:

$$\Delta\phi_{R2M} = Abs(\phi_{R2M_1} - \phi_{R2M_2}) \quad (4.4)$$

### 4.3.5 Secondary vertex quality cut

Once all the single and pair cuts have been applied all the remaining tracks are considered to be pions and are combined into triplets. To decide whether a given triplet is a good candidate all 3 tracks have to fulfill a criterion on their closest approach. As at this point still a rather large combinatorial background is present - simplified secondary vertex searching mechanism was used:

First - for all 3 possible 2 track combinations 3 two track vertices are found. For this purpose following parameterization of a track (straight line) is used:

$$\vec{P} = \vec{A} + t\vec{s} \quad (4.5)$$

where  $\vec{P} = (XLine0, YLine0, 0)$  is defined as a point in the transverse plane at the  $Z = 0$  (position of the event vertex in Z in the TPC coordinates),  $t$  is a parameter and  $\vec{s}$  is the slope vector which is defined via the track slopes in x,z and y,z plane called  $XLine1, YLine1$ .

Two track vertex (point of closest approach of the two lines in 3D) can be found analytically and is therefore very fast.

Once all 3 two-track vertices are computed the resulting 3 track vertex is obtained as a geometrical average of the 3 two-track vertices.

The quality measure of the secondary vertex is defined in following way:

$$TDTV = \sqrt{(d_1^2 + d_2^2 + d_3^2)} \quad (4.6)$$

where  $d_1, d_2$ , and  $d_3$  are the distances of the 3 track vertices to each single track. However a simple cut on the TDTV proved to be improper as it led to different efficiencies in the data and the OMC (Overlay Monte Carlo simulations - see section 4.5.3). resulting in dependence of the final mid-rapidity yields on the cut value. Therefore slightly different approach was used.

First the  $maxDTV$  was defined as the maximum of the  $d_1, d_2$ , and  $d_3$  as a function of kaon momentum in 1 GeV/c steps separately for data and OMC. To accomplish this a separate data run with a very weak TDTV cut of only 5cm was produced. The main idea was to suppress less than 1 % of the kaons both in data and OMC by the TDTV cut. The resulting  $maxDTV$  distributions for both data and OMC were integrated and cut positions for values between 50 % to 90 % were identified and stored. The Distribution of  $maxDTV$  for both data and OMC as a function of kaon momentum is



shown in Fig. 4.6. Because of the large combinatorial background it was not possible to reconstruct the  $maxDTV$  distribution for the kaon momentum  $p \in (1, 2)$  GeV/c. The resulting values for this bin were scaled from the next momentum bin based on the OMC.

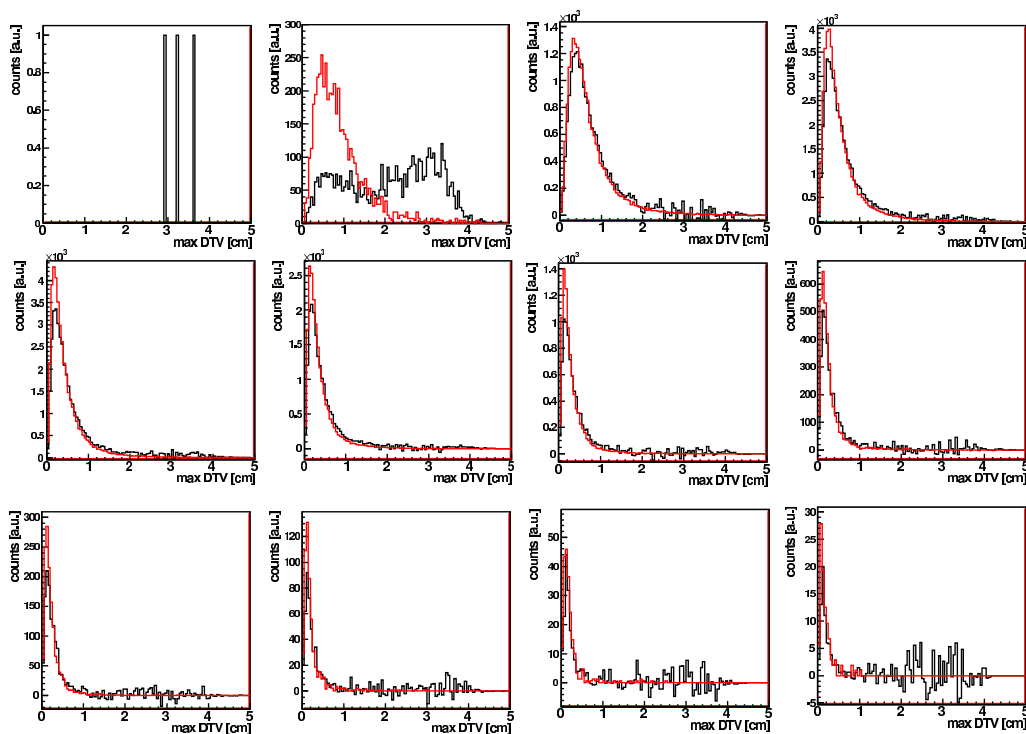


Figure 4.6: *Max. DTV distributions for data (black) and OMC (red) as a function of kaon momentum from 0 to 12 GeV/c.*

### 4.3.6 Secondary vertex position cut

As mentioned before - the very first cut applied - the  $R0$  cut together with the  $\Delta\phi R2M$  cut suppress all kaons decaying closer than 1.5 m from the target what makes this value a very good candidate to suppress remaining random combinations without disturbing the signal. On the other hand it is reasonable to apply an upper limit on the kaon vertex as well, as the reconstruction of the pions with the secondary vertex inside the TPC magnetic field would suffer because of the improper back extrapolation of the tracks.

### 4.3.7 K0 cut

K0 cut is in its nature similar to the R0 cut mentioned above. The only difference is that it is applied to the reconstructed kaon which is required to point to the event vertex in the transverse plane.

## 4.4 Phase space cuts

In addition to the cuts described above a few more cuts were applied to assure that the phase space covered in data, Overlay Monte Carlo (OMC) and mixed event background are the same.

### 4.4.1 Min $p_T$ cut

One of the cuts that is usually applied is to suppress tracks below some value of transverse momentum. The reason for this is that low  $p_T$  tracks (and for given rapidity low momentum tracks) suffer strongly from multiple scattering what is problem for the tracking on its own. Additionally this amplifies any imperfections in the chain of the simulations and may lead to problems on the level of correction factors that are obtained with the OMC. In CERES experiment values between 100 - 200 MeV/c have been commonly used. It was found that for values above 50 MeV/c this cut rapidly suppresses the signal what, as shown in the Chapter 5 lead to fluctuations of the final result and below this value the cut had very small impact. Based on these facts the final decision was not to apply this cut.

### 4.4.2 R380 versus $\theta$ R2M cut

Acceptance in the polar angle  $\theta$  of the CERES TPC is rather well defined for the primary tracks (coming from the primary vertex). Usually one applies a cut close to the edges of the acceptance where different edge effects make it difficult to fully reconstruct the behavior of the detector with the OMC. For the primary tracks are the R380 (radius at which the track enters the TPC what is at  $Z = 380$  cm) and the  $\theta$ R2M essentially the same variables.

For tracks that have originated away from the event vertex are these two variables still correlated - but not sufficient enough to allow for edge effect suppression and consequent proper OMC description of the detector response with only one of the two. For this reason a combined cut was applied.

### 4.4.3 Min opening angle cuts

The main purpose of this cut is to take into account the finite two track resolution of the TPC. In other words - below certain opening angle - two tracks originating from the same point will not be resolved by the TPC. Even if this effect would be properly simulated with the OMC, still one unsolved issue would remain - the mixed event background. In the mixed event - two tracks coming from two different events will be recognized even if their opening angle is equal to 0.

Because of the reasons mentioned above cuts on the  $\Delta\phi$  and  $\Delta\theta$  are applied. Two charged tracks inside a magnetic field, depending on their charge and relative position, either open up or approach (and eventually cross) each other. As it will be shown in the chapter 5 these two configurations (named sailor and cowboy in [50]) require different cuts and are therefore treated separately.

## 4.5 Analysis chain

The analysis consists of the Monte Carlo (MC) simulations and data analysis. While the data are pre processed and stored in the ROOT files in the *step3c* format, the MC has to be processed from the beginning.

The complete data/MC chain of the CERES simulation framework is composed of several separate subsequent programs with standardized input and output. These steps are as follows:

1. Generation of the signal tracks in form of txt files called 'user-input'.
2. propagation of these tracks by GEANT3 based program producing output in the RAWMC format.
3. Processing the GEANT output files with CERES analyzer code producing the data in the *step2* format
4. Conversion of the MC data format from the *step2* to *step3c*. At this point also the data analysis starts. Both data and MC analysis is done with the same program. Data and MC are after applying basic cuts that reduce most of the combinatorial background stored again in a ROOT tree in a *step4* output format - a simple data class.
5. Final analysis stage subdivided into several small macros.

### 4.5.1 User-input

This section (together with GEANT transport and step2 analyzer) is relevant only for the MC production. The primary  $K^+$  mesons are generated with Boltzmann distribution in transverse momentum with temperature  $T = 230$  MeV and Gaussian distribution with a width  $\sigma = 1.2$  in rapidity of  $y \in (1.4, 3.0)$  [51, 52].

Because of the low branching ratio of the  $K^+ \rightarrow \pi^+\pi^+\pi^-$  and a very long lifetime of the kaon of  $c\tau = 3.71$  m only a very small fraction of kaons would yield into 3 pion tracks in the TPC in the subsequent steps of the MC chain.

Therefore the decay of the kaon is computed at this stage so that the output file contains not the kaon tracks but the decay products (pions) themselves. The kinematics of the decay of  $K^+ \rightarrow \pi^+\pi^+\pi^-$  is performed with the method of the ROOT [53] package *TGenPhaseSpace*. With subsequent geometrical cuts - namely requiring that the decay vertex of the kaon has to take place within  $Z \in (0, 450)cm$  and that each of the decay products has to enter the TPC (defined by a cylinder with inner and outer radius) the efficiency of the subsequent steps in the MC chain improves dramatically. The  $p_T$  vs.  $y$  distribution within the selected rapidity range of kaons before and after geometrical cuts is shown in Fig. 4.7.

The fact that the kaon has a long lifetime smears the border between geometry factor and following reconstruction factor. The reason is that the geometrical cuts have to be slightly "loose" to assure that no artificial reduction of the TPC sensitive phase space is done. This approach yields into low apparent reconstruction efficiencies. To estimate the reconstruction efficiency a separate study was done in a very confined part of the phase space.

An important part of this first MC level is a generation of a calibration file that holds number of generated and (after geometrical cuts) accepted kaons in given predefined  $[p_T, y]$  bins.

The binning of the phase space was after some iterations defined in a following way. The rapidity interval of  $y \in (1.8, 2.6)$  was divided into 8 bins with a width of 0.1 rapidity unit. Transverse momentum intervals were defined with width of 0.1 GeV/c up to  $p_T = 1$  GeV/c and with a width of 0.2 GeV/c for the  $p_T > 1$  GeV/c.

The output files contain 3000 events each with 3 pions (decay products of one  $K^+$ ) per event.

### 4.5.2 GEANT transport

Again - only for MC tracks produced in the previous step. During this step all tracks included in the "user-input" files are transported through the full

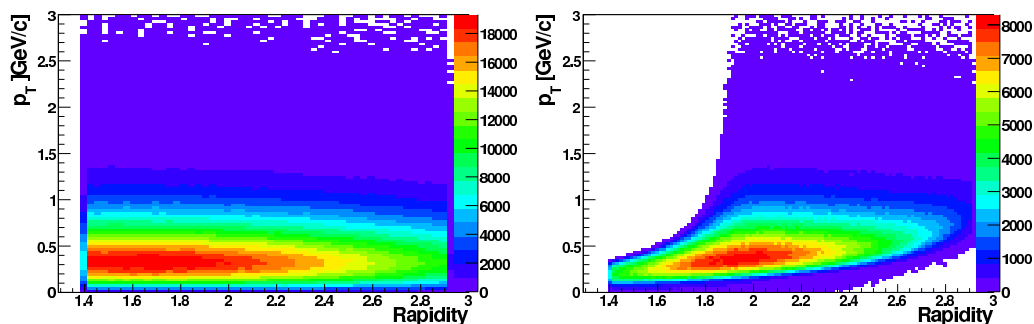


Figure 4.7: *Distribution of kaon transverse momentum versus rapidity before (left) and after (right) geometrical cuts.*

CERES setup. Output files contain data in the format of DIGI hits. The number of events per file remains the same as for the user-input files.

At this stage the interaction of the particles with the material of the detector is computed, as well as the decays of the particles. Subsequently the response of the read out electronics is simulated and stored in the output file.

### 4.5.3 Step2 analyzer

At this level of processing the MC input the decision is taken whether only the MC tracks will be further analyzed or they will be mixed with real RAW data to produce the Overlay Monte Carlo (OMC). This allows MC tracks reconstruction in a high track density environment which is present in the data analysis. In fact - the clean MC was only used for fast studies. All following results (if not stated otherwise) are produced with the OMC technique. Technically this means that the MC output of GEANT transport is mixed with a real raw data event on the level of electronic channels at the read out. To save storage and computing time only data hits in a given window around the MC hits are added. However it is important to realize that when analyzing the OMC, one looks only at the tracks that could be associated with GEANT input tracks.

The output of the Analyzer code is stored in ROOT files and has the same structure as the data at the step2 level.

#### 4.5.4 Step2 and Step3c MC/OMC analysis

The output of the step2 can be directly analyzed. To access the MC tracks that were mixed with data tracks a dedicated matching procedure has to be executed both on the hit and track level. Finally a decision whether given MC track was properly reconstructed is based on the "purity" of the given track which is defined as the fraction of MC hits from the all hits that were assigned to the given track:

$$P = nHits_{MC}/nHits_{all} \quad (4.7)$$

Purity distribution of the purity of pion tracks that originated from MC  $K^+$  is in Fig. 4.8. The MC track is considered reconstructed if the purity  $P > 0.5$ .

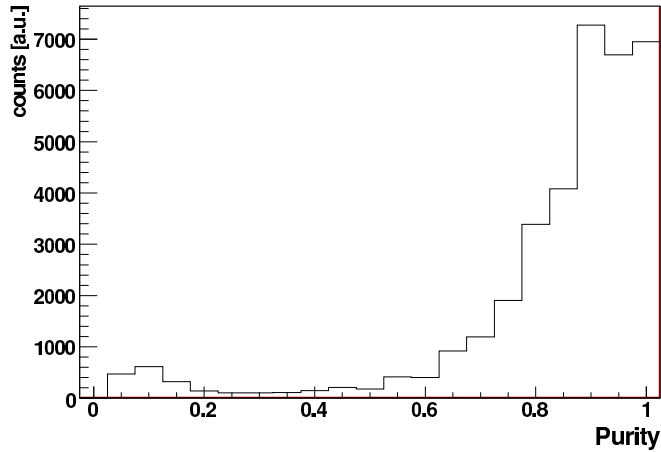


Figure 4.8: *Purity of the reconstructed pion in the Overlay Monte Carlo.*

Comparison of the reconstructed MC tracks and the original input GEANT tracks (or the "exact" tracks) is done on the level of the step2 while the full GEANT information about the MC tracks is still accessible. Because to run the step3c production of the full OMC of 9M  $K^+$  events about 200 days of computing power (standard 3 GHz CPU PC) the basic GEANT information about the reconstructed MC tracks is stored.

Data analysis starts at this level as the CERES data are stored in the step3c format. As in the case of the MC, the data analysis made at this level is very basic and kaon candidates are stored after basic cuts and the

final selection is made during the next step. The time needed to process the step3c data is comparable to full OMC step3c analysis.

#### 4.5.5 Step4 analysis

The main advantage adding one more step to the total analysis chain was to improve the flexibility of the data analysis. After the basic but powerful data reduction, the time required to run the whole data and OMC output of the step3c takes only about 15 minutes of CPU time.

During this stage the final cut studies are done and histograms with all single kaon or single pion based entries are filled and evaluated.

## 4.6 Invariant mass spectrum

The energy and the momentum of the reconstructed kaon is obtained from the sum of 3 pion 4-momentum vectors:

$$E = E_1 + E_2 + E_3 \quad (4.8)$$

$$p = p_1 + p_2 + p_3 \quad (4.9)$$

where  $p_i$  and  $E_i$  are measured momentum vectors and energy of the pions. The energy of the pion is obtained as  $E = \sqrt{m_0^2 + p^2}$ , where  $m_0$  is the rest mass of the charged pion. Invariant mass of the kaon is then obtained as:

$$m_K = \sqrt{E^2 - p^2} \quad (4.10)$$

To obtain the raw data results presented below all the analysis cuts were used. Their final values are shown in the Table 4.2. Evaluation of these cuts is given in the section 5.

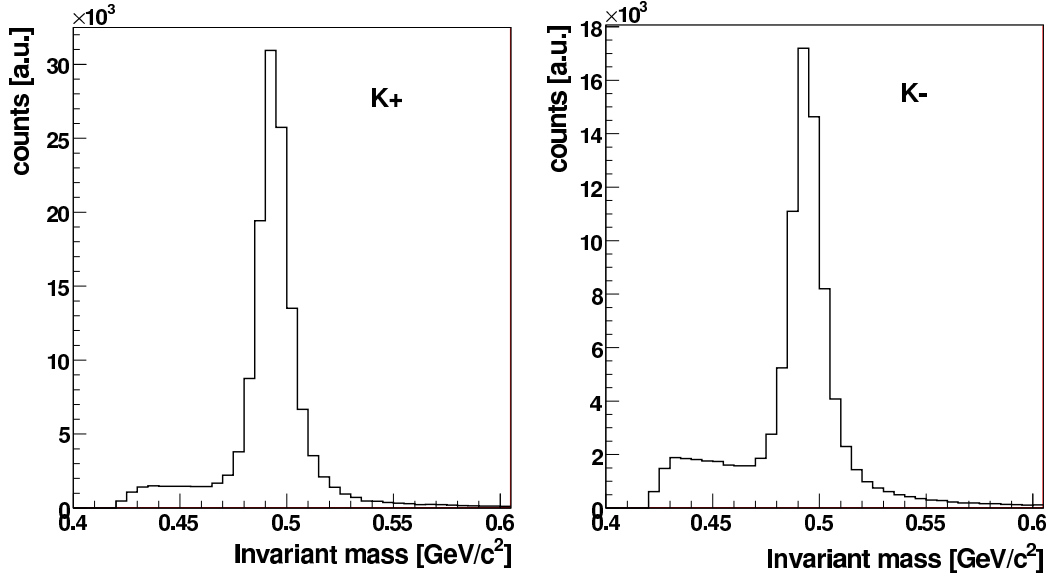
The invariant mass spectra for  $K^+$  and  $K^-$  integrated over all phase space are shown in Fig. 4.9.

## 4.7 Mixed event background

Thanks to a strong background suppression with numerous analysis cuts the  $S/B$  (signal-to-background ratio) was of around  $S/B \sim 10$  with exception

cut		value
R0	<	5 cm
NHits	$\geq$	10
dE/dx	<	(250 + 47·p) for p < 1.5 GeV/c
	<	320 for p > 1.5 GeV/c
$\Delta\phi$ R2M	<	0.3 rad
TDTV	<	80%
VertexZmin	=	150 cm
VertexZmax	=	370 cm
K0	<	4 cm
$\Delta\phi$ Local	>	0.07 (0.12) rad
$\Delta\theta$ Local	>	0.02 rad

Table 4.2: Default values of the analysis cuts.

Figure 4.9: Invariant mass distributions of the  $K^+$  (left) and the  $K^-$  (right).

of a few low  $p_T$  bins. Under such conditions can be the estimation of the background - although still necessary - done in a more relaxed way.

To estimate the shape of the combinatorial background the mixed event technique was used. The fact that the kaons were reconstructed from 3 daughter particles allowed in principle 2 different approaches. First - taking each particle from different event ( $1 \oplus 1 \oplus 1$ ) or taking two particles from one event and the third particle from second event ( $2 \oplus 1$ ). For the final analysis



---

the second method was chosen. Opposite charged particles were taken from first event and the third particle from a second event. Such an approach allowed to describe (up to some extend) possible two particle correlations that would be present in the same event combinatorial background.

To produce sufficient amount of mixed event background such that it would not significantly contribute to the statistical error on the signal extraction 5 events were mixed at a time. The selection of the events for the mixed background production were the same as the selection of events for the same event analysis.



# Chapter 5

## MC Simulations

### 5.1 Introduction

To be able to compute the absolute number of kaons out of the raw data yields a knowledge of the efficiency of the experimental setup is needed. As this can not be obtained with the data analysis itself a separate approach in which an "absolute" knowledge of the processes is known has to be applied. The complexity of the experimental apparatus does not allow to compute efficiency factors analytically and therefore a dedicated Monte Carlo simulation program is used.

The efficiency correction factors can be divided into two basic parts - the geometrical acceptance and the reconstruction efficiency. Geometrical acceptance is in principle much simpler and is defined by the geometrical shape of the detector. The reconstruction efficiency involves detailed simulation of the response of the detector and as such can be further divided into separate factors.

The basis of the reconstruction efficiency is the single track efficiency. Reconstruction efficiency for the kaon is more complicated for two reasons. First, the kaon decays far from the target what adds one more variable to the phase space (apart from  $p, \phi, \theta$ ) that would have to be explored to evaluate all edge effects. Second, the kaon reconstruction efficiency is composed of 3 track efficiencies what would "smear" the clear edge effects. For this reason the efficiency corrections were made on the level of kaons in the transverse momentum and rapidity bins. Still, the single track efficiency remains one of the main measures of the detector performance.

## 5.2 Single track efficiency

The estimation of the single track efficiency can be done in several ways and depending on the assumption the resulting numbers will change. Here described TPC single track efficiency was done in a "puristic" way. The aim was to estimate the efficiency as a function of the track momentum and azimuth angle far from all possible edge effects.

Following setting were used to generate the pion MC tracks:

- random distribution in  $\phi$  (azimuth) angle.
- fixed polar angle of  $\theta = 0.18$  rad.
- 45 different  $p$  (momentum) values with binning of 0.1 up to  $p = 1$  GeV/c, 0.2 for  $1.0 < p < 5.0$ , and 0.5 for  $5.0 < p < 10.0$  GeV/c
- 10.000 pions were generated for each momentum bin

After standard transport with GEANT based application the MC track were processes as an Overlay MC with step2 analyzer. Requirement on 7% centrality for the underlying data event was applied. To be able to estimate the effect of the detector performance itself also a clean MC was produced. In both cases 15 MC hits on reconstructed track were required.

Resulting single track efficiency as a function of momentum angle is shown in Fig. 5.1. Tracking efficiency for the pion tracks with momentum larger than 1 GeV/c the tracking efficiency is about  $\epsilon = 95.7\%$ . When compared to the single track efficiency obtained with the clean MC (Fig. 5.2) the difference of about 1.3% can be assigned to the effect of high track density environment in the central Pb+Au collision. The clean MC single track efficiency shows the tracking efficiency of the TPC itself.

Fig. 5.3 shows the single track efficiency for tracks with momentum  $p > 1$  GeV/c as a function of the polar angle. Clearly visible is the structure of the TPC read out. The large dip at  $\phi = -3.3$  rad is caused by one inactive raw of read out cards during the data taking.

## 5.3 Cut study

The reconstruction of charged kaons presented in this thesis is based on series of cuts as they were shortly presented in chapter 4.2. Here the single cut distributions in data and OMC and development of the shape of the invariant mass spectrum in data and efficiency of these cuts in OMC are

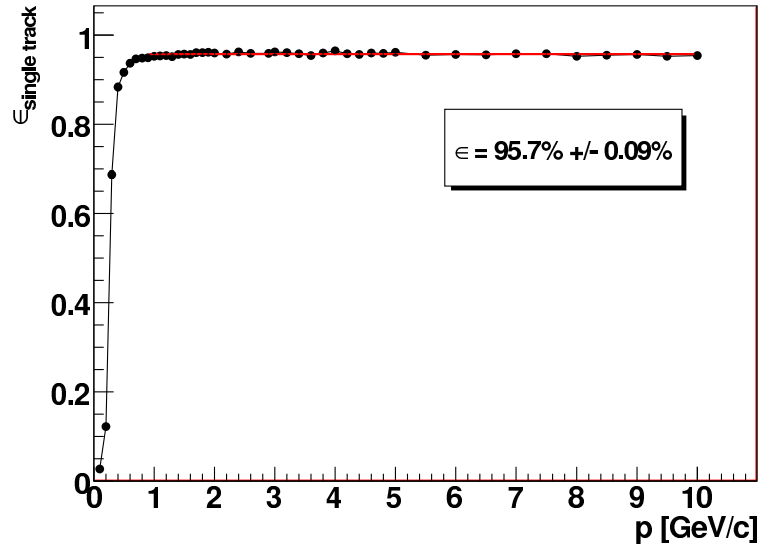


Figure 5.1: *TPC single track efficiency as a function of momentum in OMC.*

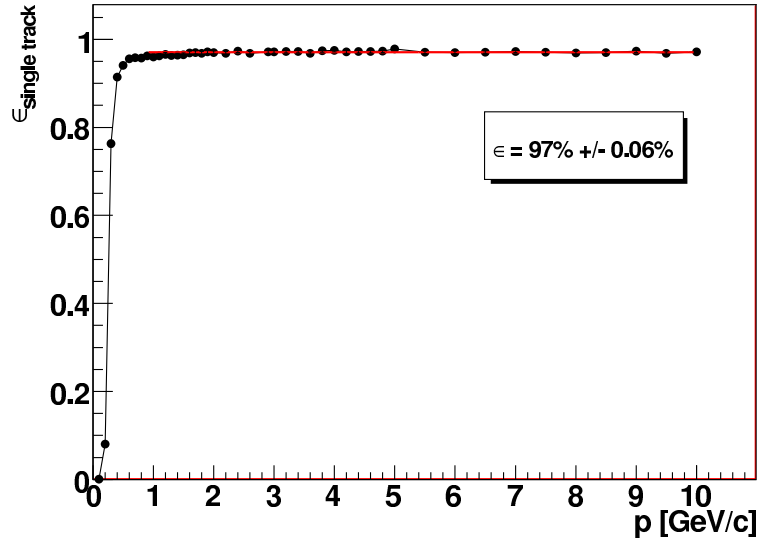


Figure 5.2: *TPC single track efficiency for clean MC as a function of momentum .*

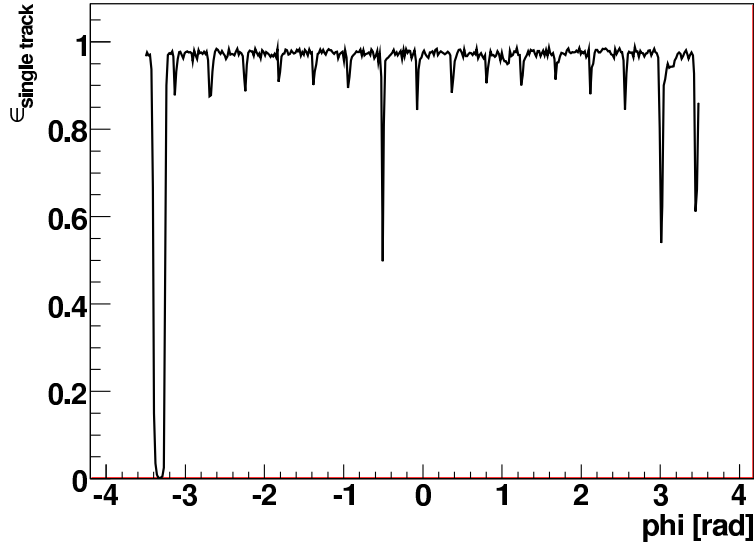


Figure 5.3: *TPC single track efficiency for tracks with momentum  $p > 1$  GeV/c as a function of azimuth angle.*

presented. In all the following cut distributions the actual cut value is shown as a red line.

The following invariant mass spectra include all phase space covered by the TPC. Each subsequent cut study includes the previous cuts. Please note that because of the very high combinatorial background the number of data events is different for each cut starting at only one data event (no cuts applied) up to 24M events (all cuts applied). Because of this reason the number of entries in the data invariant mass distributions are not directly comparable. The efficiencies of the cuts are summarized at the end of the chapter.

### 5.3.1 No cuts applied

Without applying any analysis or phase space cuts practically the only component of the kaon invariant mass distribution are random 3 particle combinations. The kaon invariant mass distribution is shown in the Fig. 5.4.

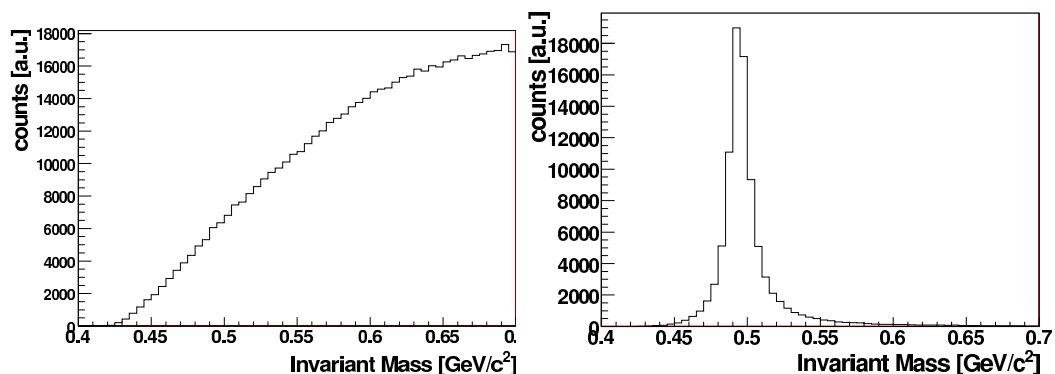


Figure 5.4: *Invariant mass distribution in the data (left) and OMC (right) without any cuts applied.*

### 5.3.2 R0 cut

The first cut applied is the cut on the transverse distance of single tracks to target. The R0 distribution in the data and OMC is shown in Fig. 5.5. This cut results into very large background suppression, but suppresses about 50% of the signal as well. As any single particle cut, this cut comes with a third power. In other words - if one of the 3 pions does not pass the condition - the kaon is rejected. The shape of the invariant mass after this cut is shown in Fig. 5.6.

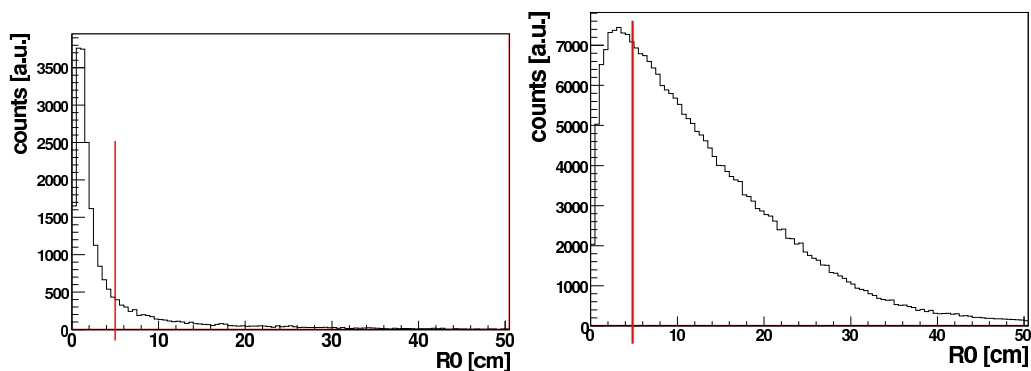


Figure 5.5: *R0 distribution for data (left) and OMC (right). Red line represents the cut value.*

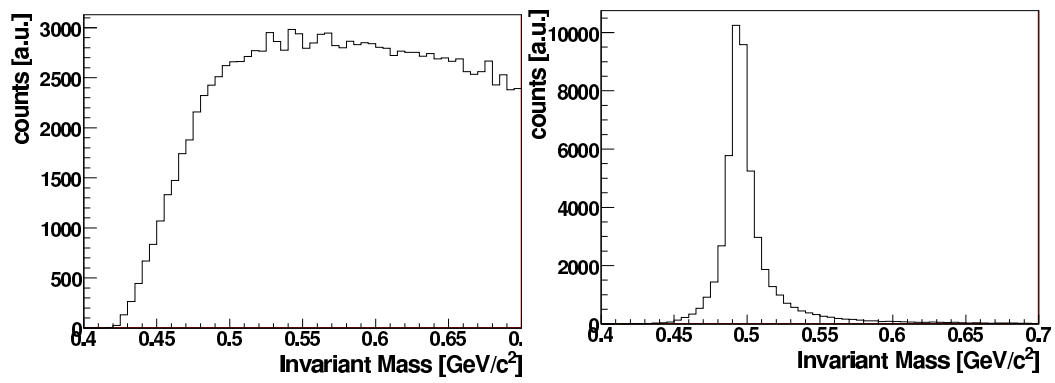


Figure 5.6: *Invariant mass distribution after R0 cut. Data (left) OMC (right).*



### 5.3.3 NHits cut

Minimal cut value on the number of hits on the track is applied already during step2 production where a track is accepted only if it has 7 or more hits. Final cut value on number of hits of  $N_{hits} \geq 10$  was chosen to obtain tracks with properly estimated track parameters. As shown later the number of hits on track is rather well, but not perfectly described in the OMC what also had an impact on the final value of the cut. The distribution of NHits is shown in Fig. 5.7. Invariant mass distribution both for data and OMC after this cut is shown in Fig. 5.8.

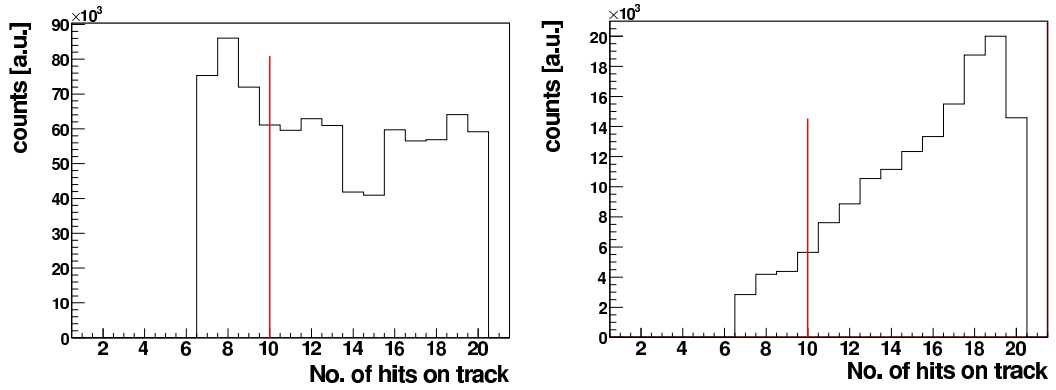


Figure 5.7: *Distribution of the number of hits for data (left) and OMC (right).*

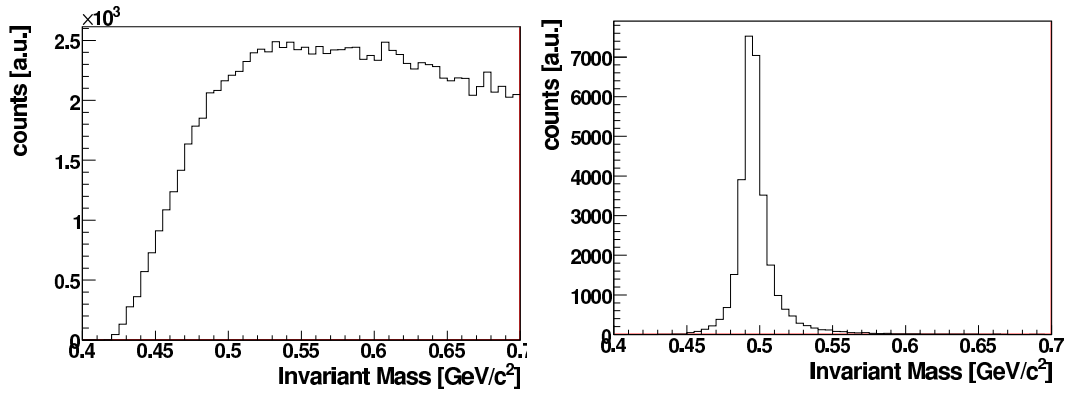


Figure 5.8: *Invariant mass distribution after NHits cut. Data (left), OMC (right).*

### 5.3.4 $dE/dx$ cut

This cut relies on the fact, that especially for low momentum tracks the difference in the energy loss of a pion and an electron is large enough to apply a momentum dependent cut which allows to suppress many of the conversion electrons and positrons that are produced in the R2M and in the front support wheel of the TPC.

However before this cut can be applied the simulated  $dE/dx$  losses need to be scaled to the data. This is accomplished in a following way. Both measured and simulated  $dE/dx$  losses are fitted around the maximum as a function of momentum (in 0.2 GeV/c bins) and positions of the maxima of the  $dE/dx$  distributions are extracted. Subsequently the correction factors are obtained as a ratio of the obtained pion  $dE/dx$  peak positions. The resulting  $dE/dx$  correction factors (shown in bottom left panel in Fig. 5.9) are then applied to the OMC. Only after this correction the  $dE/dx$  cut can be applied.

The  $dE/dx$  cut removes very little signal but strongly suppresses the background in the low mass region. The resulting invariant mass distributions are shown in Fig. 5.10.

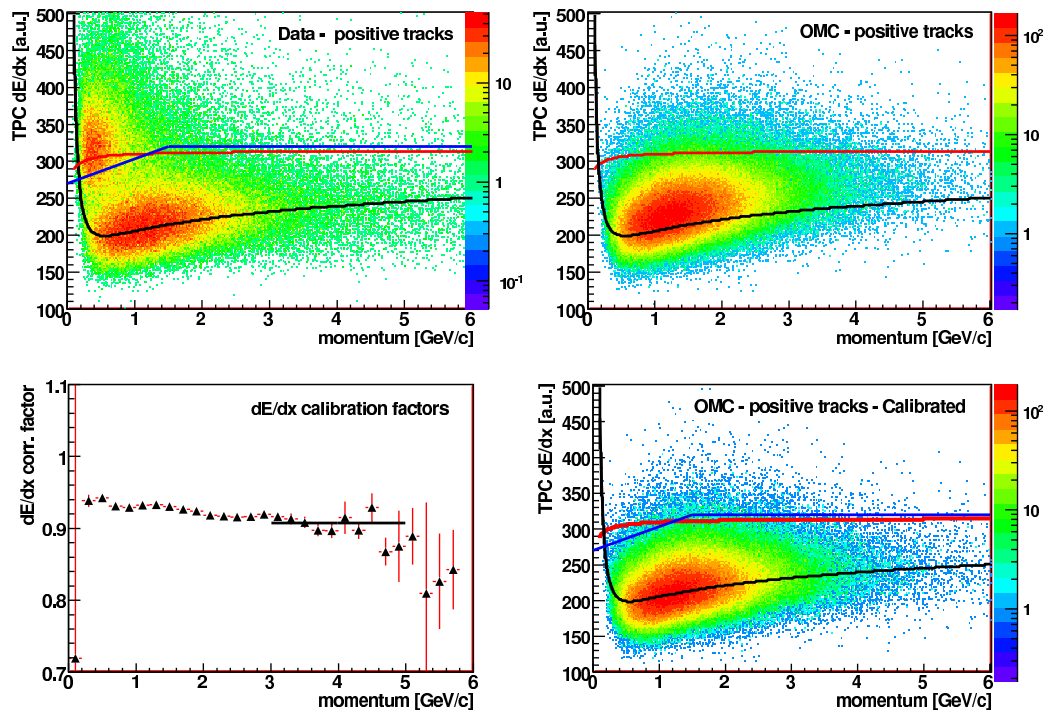


Figure 5.9: Top left:  $dE/dx$  distributions of positive single tracks in the Data after applying most of the analysis cuts. Electrons are clearly visible. Top right:  $dE/dx$  for positive tracks in the OMC before correction. Bottom left:  $dE/dx$  correction factors as function of momentum. Bottom right: OMC  $dE/dx$  after applying the correction. Full lines - parameterized energy loss of a pions (black) and electrons (red). The blue line shows the  $dE/dx$  cut.

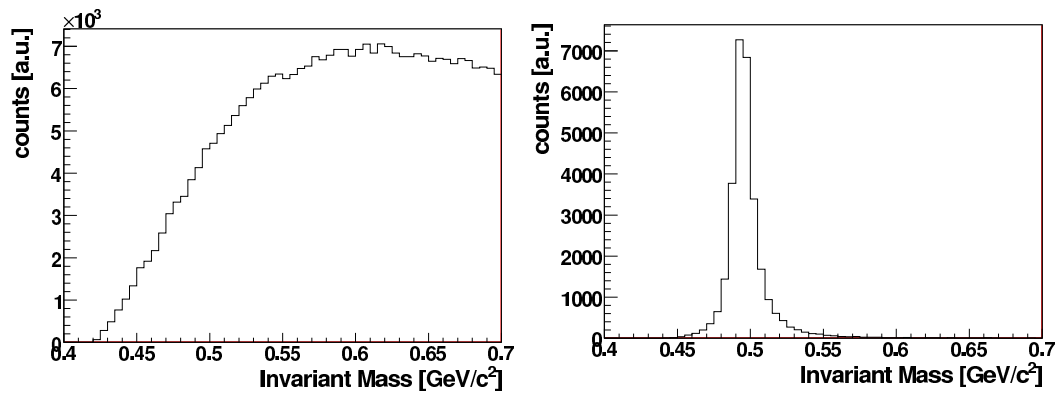


Figure 5.10: *Invariant mass distributions after  $dE/dx$  cut. Data (left), OMC (right).*

### 5.3.5 $\Delta\phi$ R2M cut

Thanks to the geometry and kinematics of the kaon decay together with the R2M angle definition in the CERES experiment (as described before) the cut on the difference of the azimuth angle between two tracks allows to suppress the background further. The Fig. 5.11 shows the difference of the  $\phi$  R2M angles between any 2 tracks from the triplet. The effect on the invariant mass distributions is shown in Fig. 5.12.

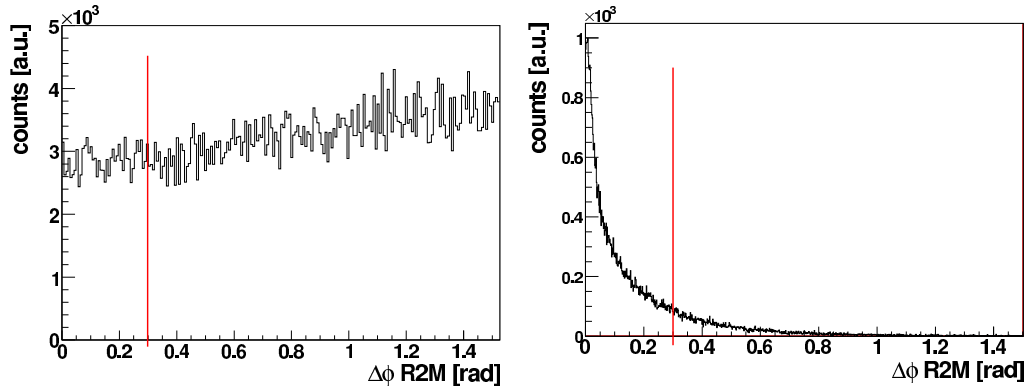


Figure 5.11:  $\Delta\phi R2M$  distributions for the data (left) and OMC (right).

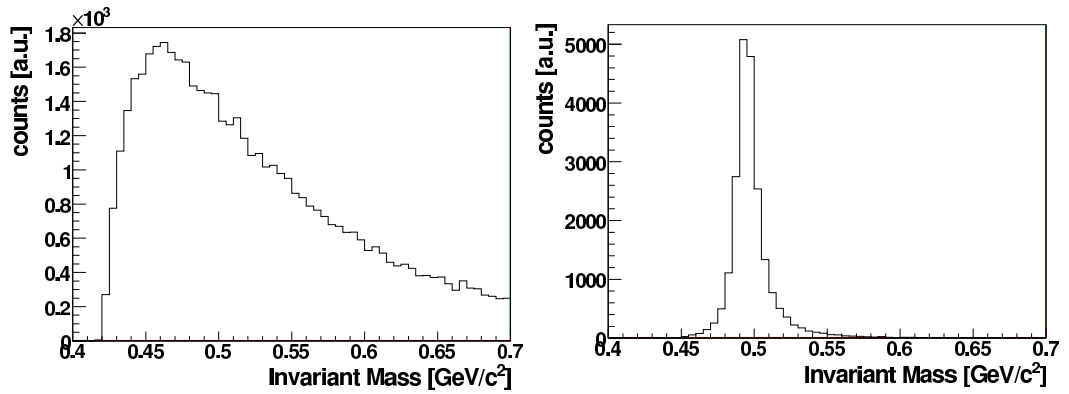


Figure 5.12: Invariant mass distributions for the data (left) and OMC (right) after  $\Delta\phi R2M$  cut.

### 5.3.6 Kaon vertex quality cut - TDTV

The TDTV cut fully relies on the TPC tracking capabilities. It is a powerful triplet cut and suppresses about 90 % of the background. Only after this cut the signal peak emerges from the combinatorial background. Simplified representation of the application of this cut is shown in Fig. 5.13. The actual value of the cut is momentum dependent as described in 4.3.5. Invariant mass distributions after this cut are shown in Fig. 5.14.

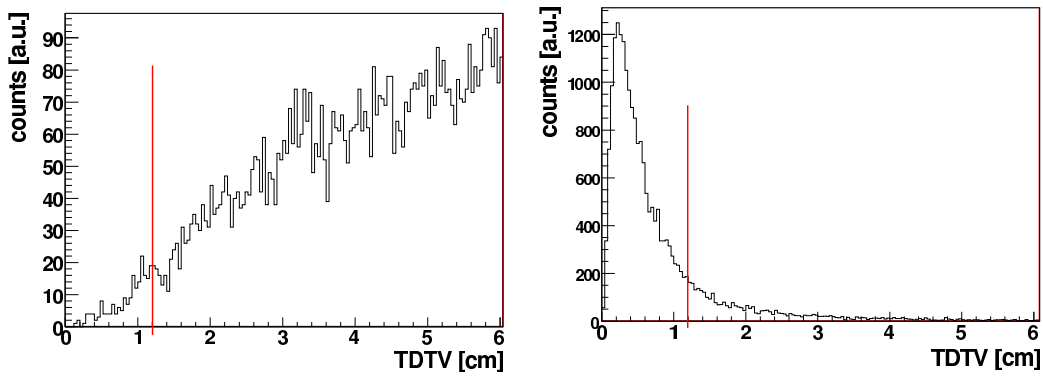


Figure 5.13: *TDTV distributions for the data (left) and OMC (right).*

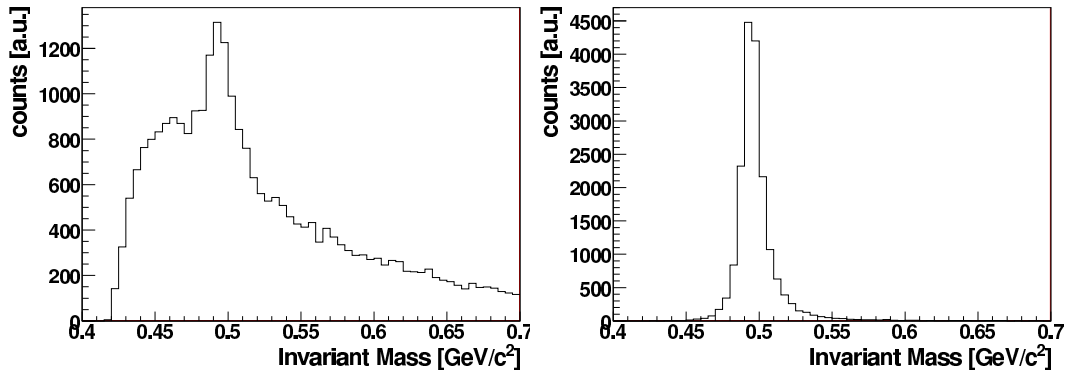


Figure 5.14: *Invariant mass distributions for the data (left) and OMC (right) after the TDTV cut.*

### 5.3.7 Kaon vertex position

As already mentioned the R0 cut together with  $\Delta\phi$ R2M cut suppress nearly all the kaons with secondary vertex position in Z below 100 cm (see Fig. 5.15). The lower cut value of Z = 150 cm suppresses very little signal while suppresses remaining random background combinations. The upper value of the cut at Z = 370 cm excludes kaons decaying inside the TPC magnetic field where the track parameters reconstruction would be incorrect as the tracking software of the CERES TPC assumes the track has passed the whole magnetic field. The sharp edge of the OMC kaon vertex Z distribution is caused by the cut applied during the user-input generation. The invariant mass distributions after VertexZ cut are shown in Fig. 5.16.

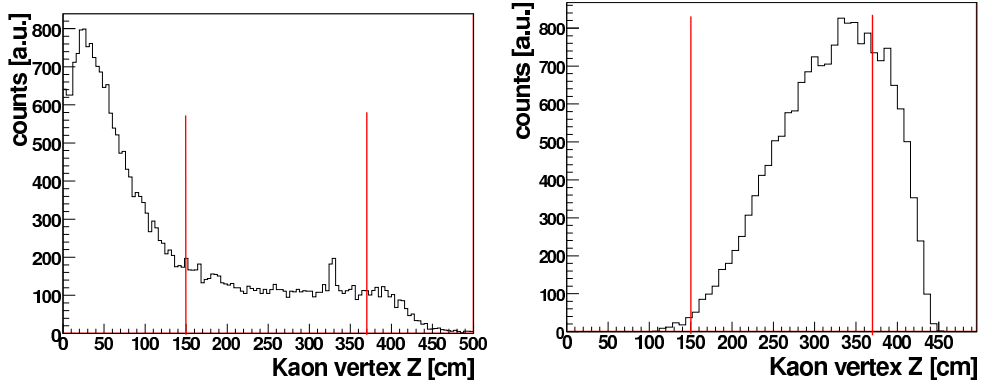


Figure 5.15: *Distributions of the Z component of the reconstructed kaon secondary vertex for the data (left) and OMC (right).*

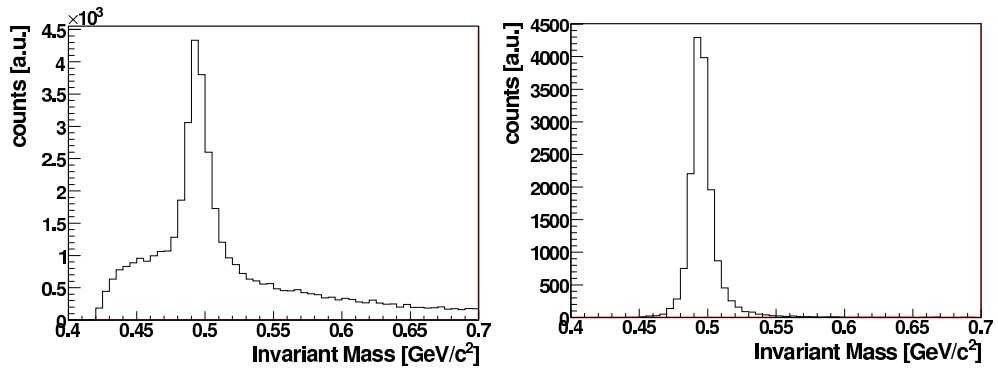


Figure 5.16: *Invariant mass distributions after the VertexZ cut for the data (left) and OMC (right).*

### 5.3.8 K0 cut

$K_0$ , or transverse distance of the reconstructed kaon to the target allows to suppress most of the remaining random combinations. The "true" kaons are requested to point to the primary vertex. The width of this distribution reflects the tracking resolution of the TPC and the method applied. At this stage the shape of the  $K_0$  distribution in the left panel of the Fig. 5.17 clearly shows the "true" kaons and combinatorial background component. Invariant mass after the  $K_0$  cut is shown in Fig. 5.18.

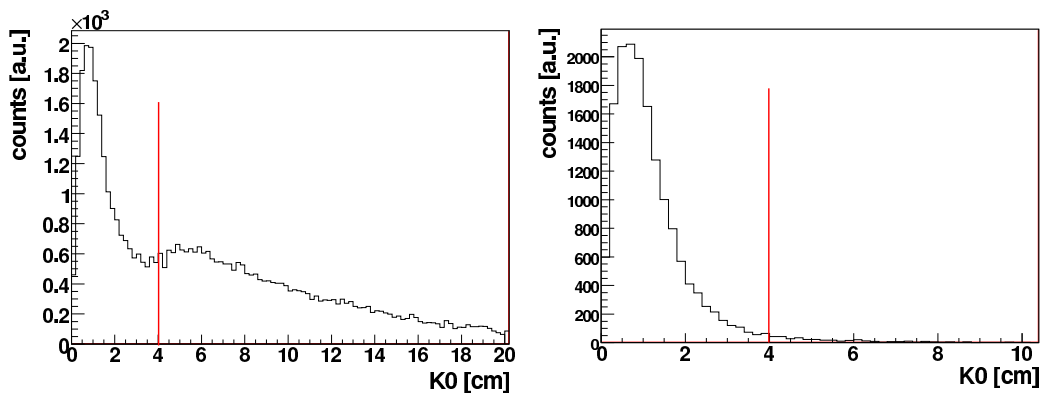


Figure 5.17:  $K_0$  distributions for the data (left) and the OMC (right).

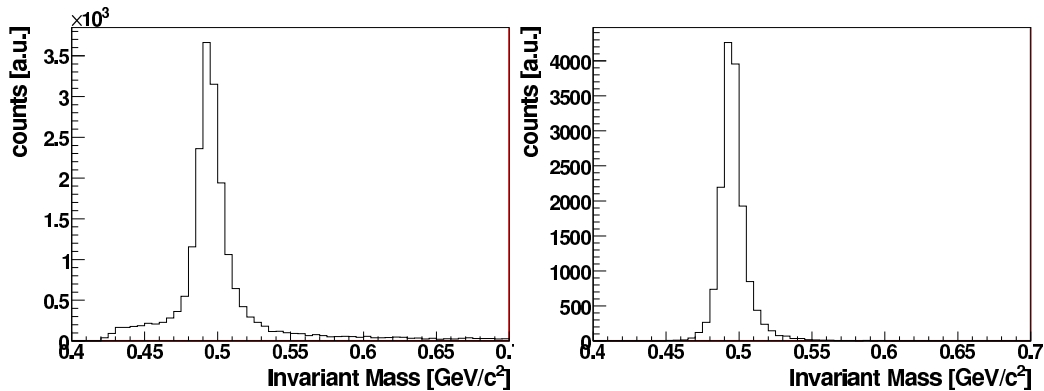


Figure 5.18: Invariant mass distributions for the data (left) and the OMC (right) after the  $K_0$  cut.



### 5.3.9 Opening angle cut

To account for the final two track resolution of the TPC the minimal angle for each pair of two tracks was required. In reality - it is not only the angle between two tracks that is limited by the resolution - also the distance of the two tracks inside the TPC matters. Because the range of the kaon secondary vertex was approximately 150 - 400 cm one would expect the dependence of the minimal opening angle between two tracks.

In our case not directly the opening angle was used, but rather the differences in the azimuthal ( $\Delta\phi$ ) and polar ( $\Delta\theta$ ) angles separately. The distribution of these two angles for two topologies (sailors and cowboys) for both data and OMC for 3 bins in the secondary vertex of the kaon are shown in Fig. 5.19.

The full data statistics did not allow precise estimation of the cut and therefore the cut values were estimated with the OMC.

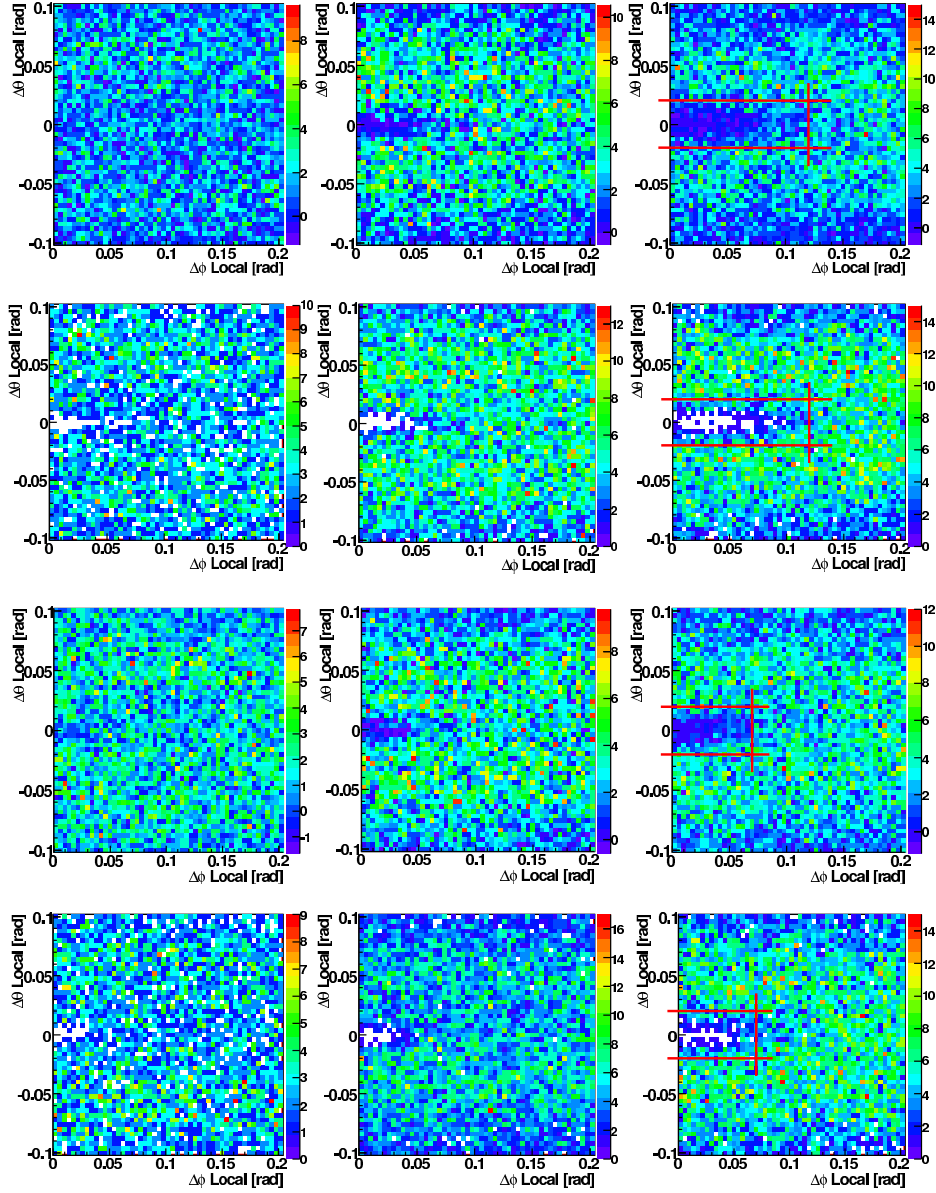


Figure 5.19:  $\Delta\theta_{Local}$  versus  $\Delta\phi_{Local}$  for: 1. row: data cowboys, 2. row: OMC cowboys, 3. row: data sailors and 4. row: OMC sailors. Columns represent 3 bins in kaon secondary vertex  $Z \in (150, 250, 320, 400)$ . Red lines represent the cut values. Only same charge (positive) pairs were used.

### 5.3.10 R380 versus $\theta_{\text{Local}}$ cut

This cut is an analogy to the cut on  $\theta_{\text{R2M}}$  (polar angle) cut for tracks that originate from primary vertex. It was shown in previous CERES data analysis [43, 44, 50] that an upper and lower limit has to be applied on the polar angle as for track with  $\theta$  close to the edge of the acceptance the description of the OMC does not reproduce the data well anymore. The main reason for this effect are the regions close to the inner/outer radius of the TPC where edge effects are hard to describe in full detail.

Because the kaon decays at large distances from the event vertex and its decay products do not point to the event vertex a cut on the polar angle only is not an optimal solution. Therefore a two dimensional cut - radius at which the track enters the TPC (named R380) versus the local polar angle - was introduced. In the Fig. 5.20 the regions at small and large R380 where the reproduction of the Data with the OMC is not good can be clearly seen.

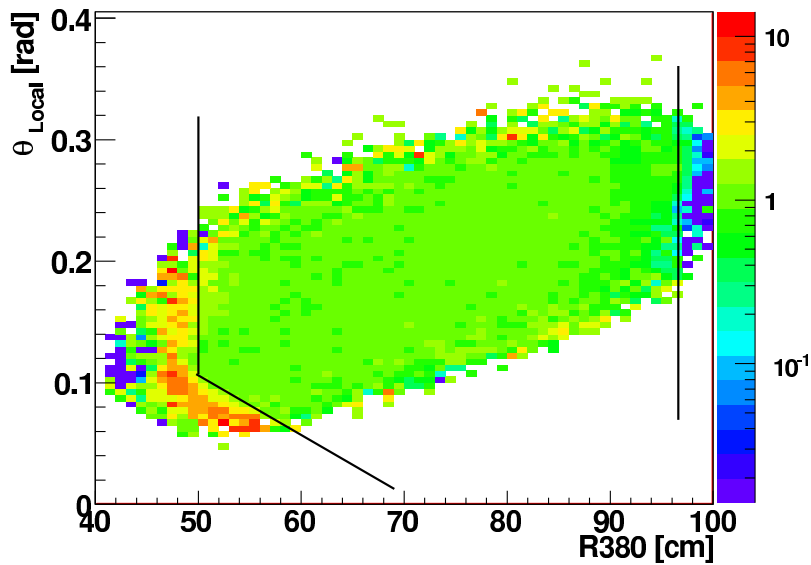


Figure 5.20:  $\theta_{\text{Local}}$  angle of a single track versus the radius at the entrance to the TPC. The data shown is the ratio of (Data-MixBG) to scaled OMC, so the expected value of the ratio is 1. The black lines show the cut position.

### 5.3.11 Summary

Overview of the effects of the cuts on the combinatorial background in the data and signal in the OMC is presented in Fig. 5.21. The total background suppression of  $\sim 10^8$  is a rather impressive number. However along with a strong background suppression also a suppression of the reconstructable signal by a factor 4 was unavoidable.

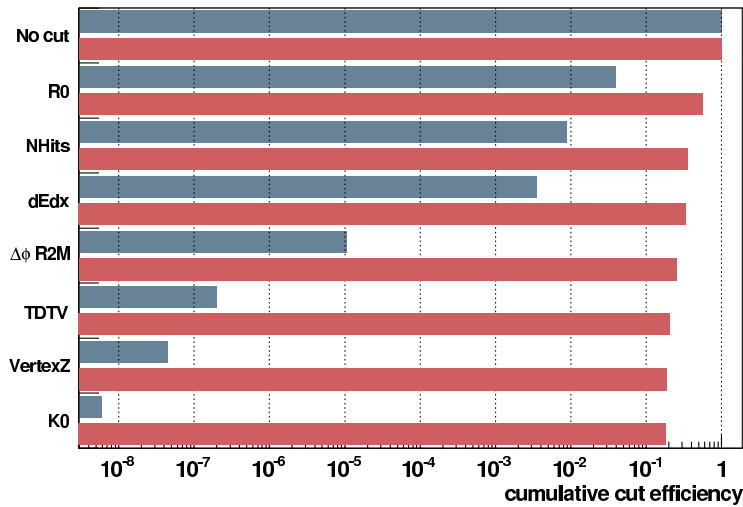


Figure 5.21: *Efficiency of the analysis cuts for the combinatorial background in the data (upper blue bands) and signal in the OMC (lower red bands). The effects of the cuts accumulate from the top (no cuts applied) to bottom (all cuts applied).*

## 5.4 Cut Study II

### 5.4.1 Cut distributions

The comparison of the data with the OMC can be done in several ways. Although it is not possible to reconstruct with the OMC all cut distributions and compare them with data (because of small S/B ratio in the data), it is possible to plot these distributions after the cuts were applied.

Fig. 5.22 shows the comparison of the cut distributions between data and OMC for 6 of the cuts. The OMC (red) distributions were scaled to data (black) via integral. The comparison of the  $dE/dx$  distributions is shown as a ratio of the  $(Data - MixedBG)/OMC$  where the OMC was scaled to the data so the expected ratio is 1.

Overall the agreement is good with a slight exception of  $nHits$  cut. Although the level of disagreement between the Data and OMC is similar, the impact of the disagreement (as shown in the next section) is much stronger for the cut on the number of hits. The reason is that it is a single track cut and even a small disagreement becomes very apparent. For this reason the value of the cut was set to 10.

### 5.4.2 Cut stability

The value of each given cut is not only determined via optimizing the significance of the signal, but also by the stability of the given cut. To study the influence of the single cut variation on the final  $dN/dY|_{Y=0}$  one cut at a time was varied around its default value while the rest of the cuts were kept at their default values.

The results for  $K^+$  and  $K^-$  are presented in Fig. 5.23 and 5.24. Cut values marked by the arrows have been placed at points where the signal is stable with the exception of the maximum position of the kaon vertex  $Z$ . Here the cut value was constrained from the upper side by elimination the decays inside the TPC magnetic field which starts at around  $Z = 380$  cm. Further study could shed some light on this issue.

### 5.4.3 Peak extraction efficiency

To extract the peak 3 different signal extraction procedures were applied:

- **ver.1** : Fit of the spectra with a Gauss function plus a polynomial of 4th order.

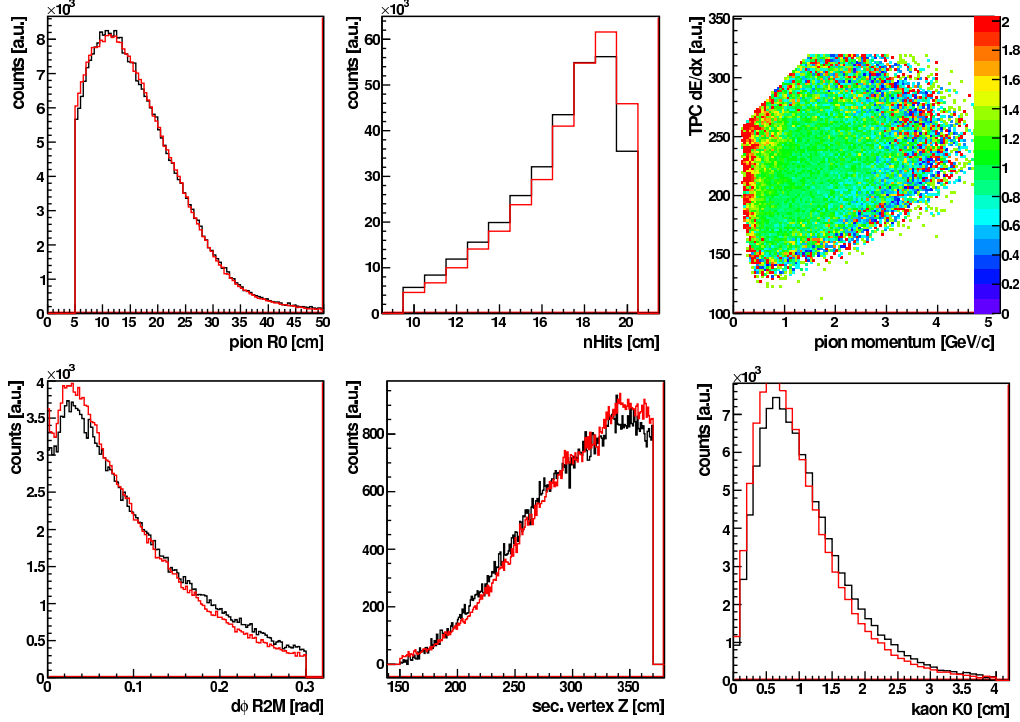


Figure 5.22: Comparison of the cut distributions for data (black) and OMC (red) in the order from top-left to bottom-right:  $R_0$ , Number of hits on track,  $dE/dx$  as a function of pion momentum,  $\Delta\phi R_{2M}$ ,  $Z$  component of the secondary vertex and  $K_0$ .

- **ver.2** : Fit of the spectra after mixed event background suppression with gauss function only. The number of entries in the invariant mass distribution is obtained from the fit function. This method was used to obtain the final  $p_T$  spectra.
- **ver.3** : Sum of the spectra after mixed event background suppression - the range of the sum was defined by a fit with gauss function.

Because the shape of the signal is not a perfect Gaussian a correction factor was applied via comparison of an integral of the fit function within a  $2\sigma$  that should include 95% of the signal with content of the peak in the OMC. In most cases the correction was around 5%. The same approach was applied to summing of the OMC and data spectra. But to be able to apply this approach the shape of the OMC invariant mass spectra needs to reproduce the shape of the invariant mass in data. Comparison of the data

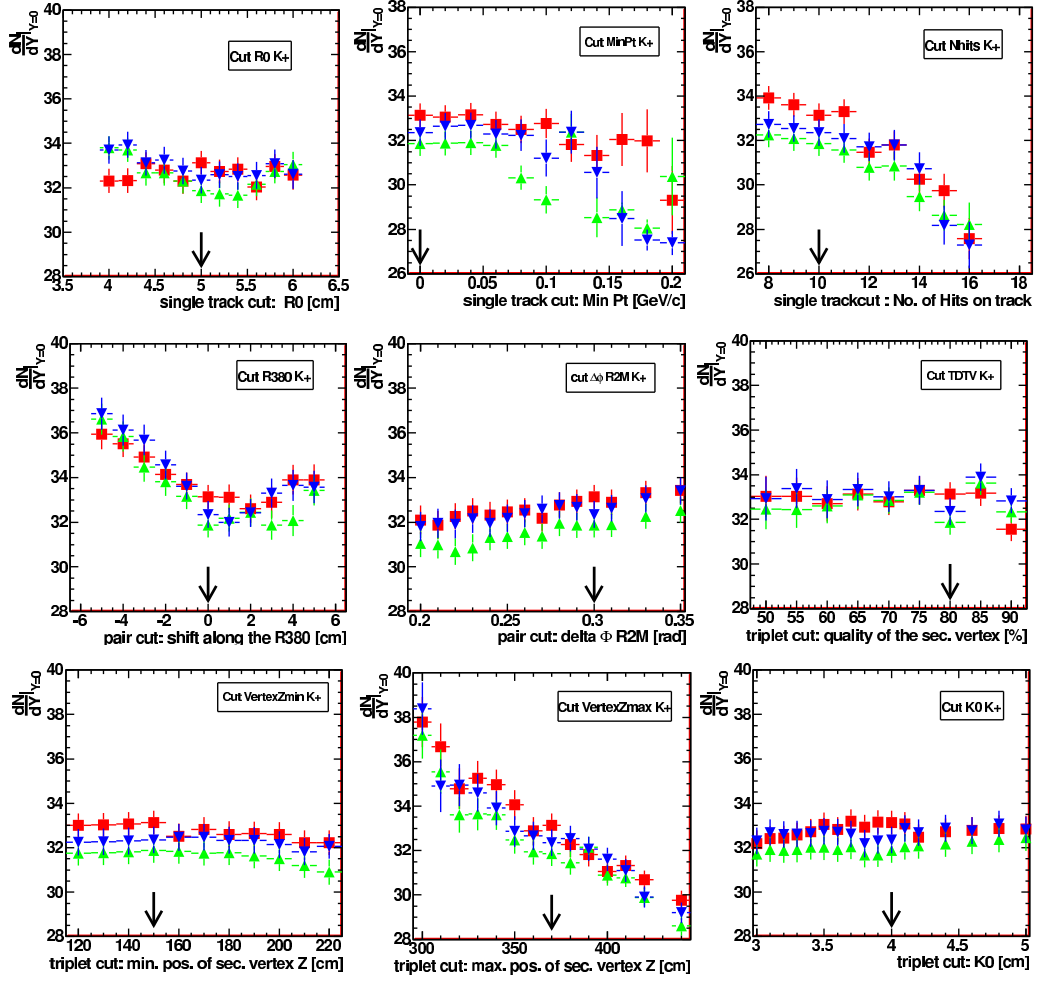


Figure 5.23:  $K^+$ : Cut stability check for 9 basic cuts. Different symbols present different signal extraction methods: fit of data with gauss + polynomial (blue  $\blacktriangledown$ ), fit of the signal after mixed event background subtraction with gauss only (green  $\blacktriangle$ ) and sum of the data after mixed event background subtraction (red  $\blacksquare$ ). Arrows represent the default cut values.

spectra to scaled (via integral) OMC spectra summed with scaled mixed event background is shown in Appendix A.

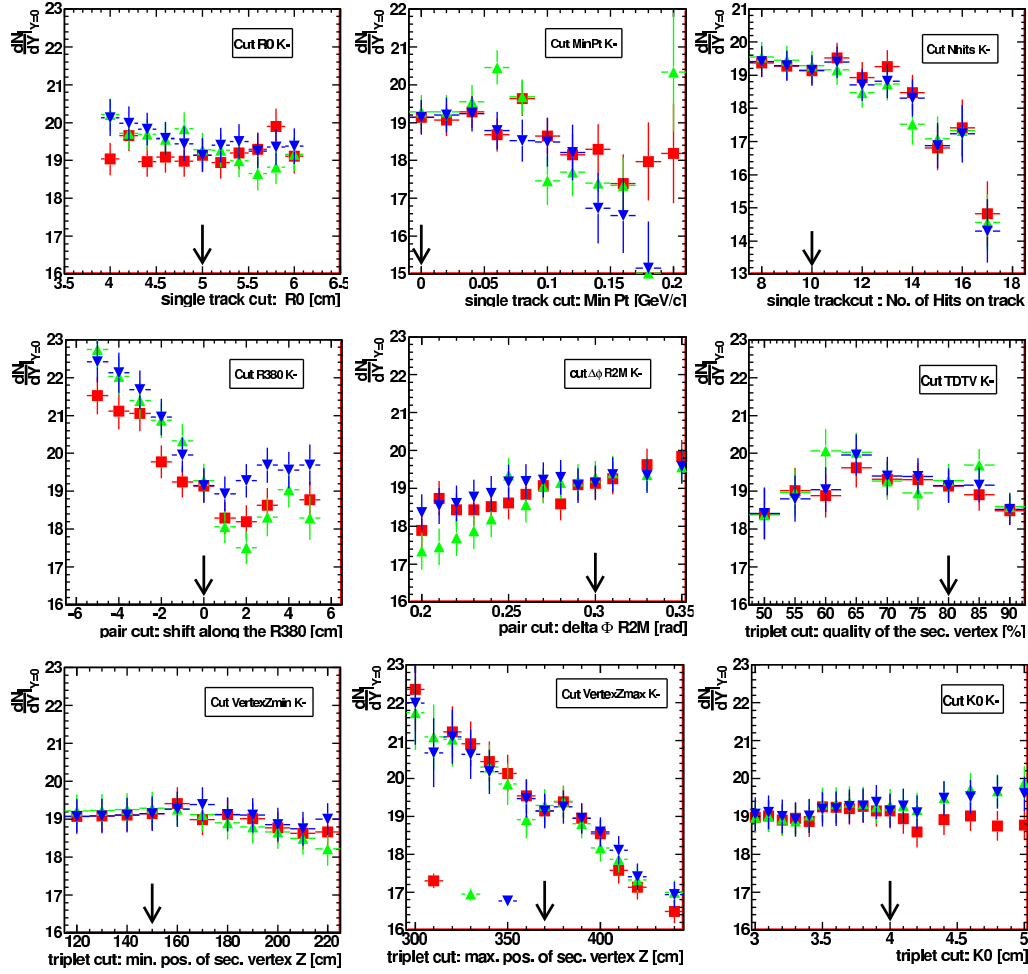


Figure 5.24:  $K^-$ : Cut stability check. Symbols present different signal extraction methods (see Fig. 5.23).

#### 5.4.4 Fit parameters

Another important comparison of the data and OMC are the fit parameters of the signal extraction - the mean value and the sigma. The mean value is the reconstructed invariant mass of the kaon and can directly be compared to the PDG value of  $m_{K^+} = m_{K^-} = 493.677 \pm 0.016 \text{ MeV}/c^2$  [27]. The width of the distribution reflects the resolution of the momentum measurement.

The distributions of the mean value and the width as a function of  $p_T$  for all rapidity units are shown in Fig. 5.25. The agreement between data  $K^+$  and  $K^-$  is rather good what implies good quality of the charge symmetry in



the reconstruction.

While OMC and data value of the mass of the kaon agree very well and in the low  $p_T$  the agreement with PDG value is very good, the slope of the  $p_T$  dependence is very pronounced and shows a clear dependence on the rapidity. This can be explained by the bias in the momentum reconstruction. The momentum reconstruction is based on measurement of a radius of a track in the magnetic field. While for low momentum tracks the error on the radius will yield approximately in symmetrical distribution of the momentum resolution, for the high momentum tracks (tracks with a shape close to straight line) the reconstructed momentum is on average larger than the true momentum of the track.

The extracted width of the kaon invariant mass shown in the lower part of the Fig. 5.25 shows only minor dependence on the  $p_T$ , but increases rather strongly with the rapidity. This effect is assigned to relative momentum resolution which deteriorates with the momentum of the track.

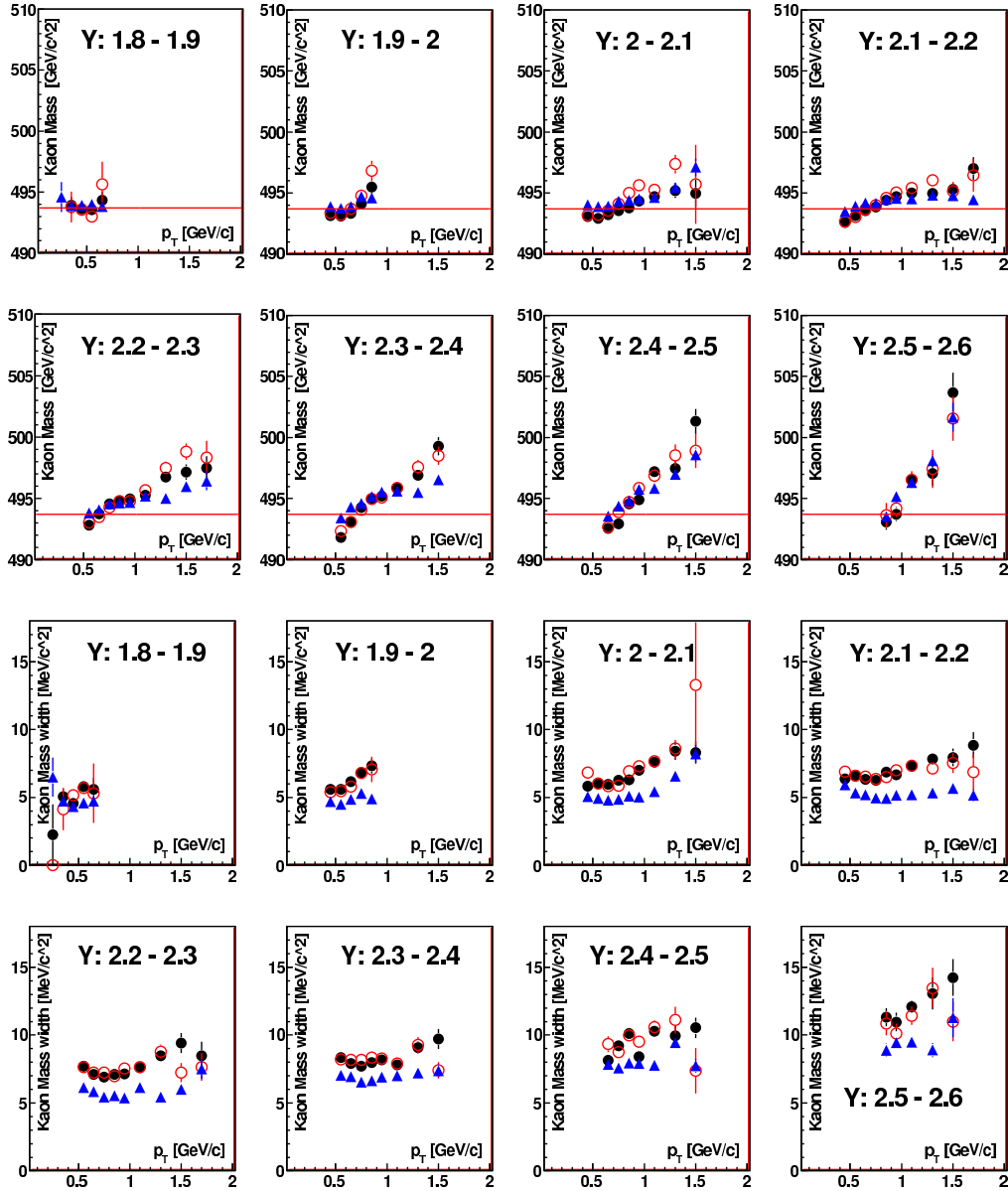


Figure 5.25: Comparison of mean value and width of the  $K^+$  invariant mass fit. Upper part: Mean value of the fit for data  $K^+$  (black  $\bullet$ ), data  $K^-$  (red  $\circ$ ) and OMC  $K^+$  (blue  $\blacktriangle$ ). The red line indicates the PDG value of the mass of the  $K^+$ . Lower part: Extracted width of the invariant mass peak. Please note the fixed range of the distributions in both cases.

# Chapter 6

## Final results

Once the correction factors obtained with the help of OMC are known, the corrected results can be produced. The signal extracted in  $p_T$  -  $y$  bins is used to obtain the  $p_T$  distributions. Further analysis of the  $p_T$  spectra is than used to obtain the rapidity spectra and the mid-rapidity yield.

Before the obtained results can be compared to other existing measurements or theoretical predictions the systematical error has to be estimated.

### 6.1 Raw yield

Very basic result that shows the shape of the invariant mass for the whole  $p_T$ - $y$  phase space can be used to estimate the total number of kaons reconstructed and gives the impression of the shape of the signal and the background. The integrated invariant mass distributions of  $K^+$  and  $K^-$  are shown in Fig. 6.1 together with scaled mixed event background. In total approx. 102k  $K^+$  and 55k  $K^-$  reconstructed in 24.3 million Pb+Au 7% most central events.

Important for the stability of the analysis is very good description of the shape of the invariant mass distribution by the Monte Carlo simulations. That this condition is fulfilled rather well can be seen in the Appendix A where invariant mass spectra of the  $K^+$  in  $[p_T, y]$  bins together with scaled mixed event background and scaled OMC signal are shown.

The shape of the invariant mass distribution (when compared to the Gaussian function that was used for the signal extraction) shows more pronounced tails and slight shoulder on the right side of the peak. This feature is rather well described with the OMC and is assigned to non symmetrical distribution of the momentum reconstruction.

The slight excess of the mixed event background over the same event background in the low mass region is pronounced only in the low  $p_T$  region

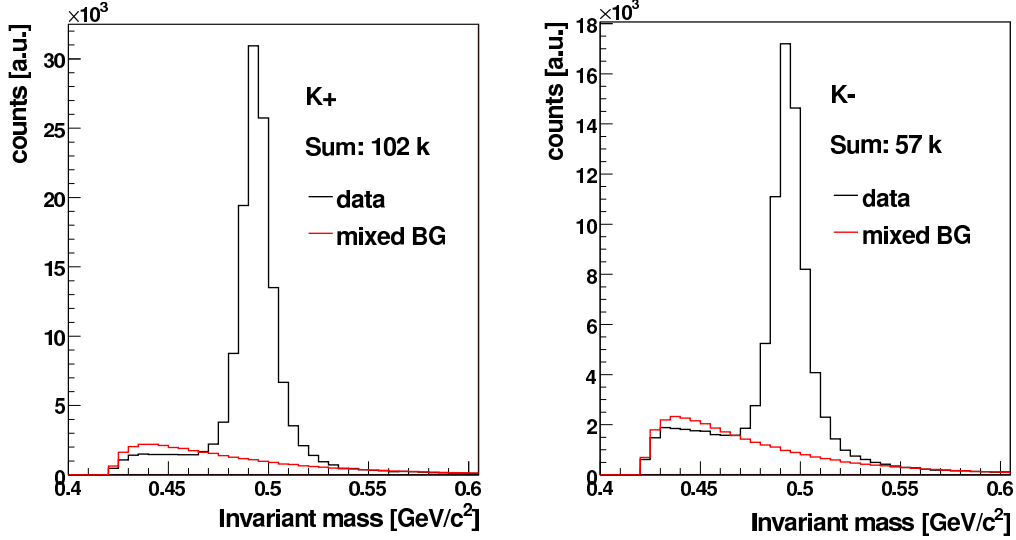


Figure 6.1: *Integrated invariant mass distribution of the  $K^+$  (left) and  $K^-$  (right). The red line shows the estimation of the combinatorial background with the mixed event technique. Total amount of the reconstructed kaons is quoted.*

of the signal and is assigned to remaining particle correlations that are not present in the mixed event background like Coulomb interaction, etc.

## 6.2 Transverse momentum spectrum

Corrected transverse momentum spectra for  $K^+$  and  $K^-$  are shown in Fig. 6.2 and Fig. 6.3 respectively. The correction factors obtained with the OMC are shown in Fig. 6.4.

The lowest  $p_t$  points for which correction factors lies on a very steep slope were not included in the fit.

To estimate the yield per rapidity unit an extrapolation procedure of the spectra towards the  $p_T = 0$  GeV/c was necessary. The commonly used method based on fitting the spectra with Boltzmann function was employed. The choice was based on the fact that it is the simplest approximation of the shape of the  $p_T$  spectra and depends only on two parameters - yield and temperature, where the temperature parameter is directly related to the temperature of the thermal source in  $p_T$  and describes the slope of the spectra.

More elaborated approaches (as later mentioned Blast wave model) take

into account another physics effects that are present in the  $p_T$  spectra as for example transverse and longitudinal flow. However - to obtain reliable fits with these models good quality of the data especially at low  $p_T$  is required.

Commonly known form of Boltzmann function is following:

$$\frac{dN^2}{dp_T dy} = A \cdot p_T \cdot \exp\left(-\frac{\sqrt{m^2 + p_T^2}}{T}\right) \quad (6.1)$$

where  $A$  is scale and  $T$  is temperature. This form is not optimal for the data fitting because the integral - the total yield - depends on both parameters and so does the error of the integral. The formula can be transformed such that the scale parameter is divided into two parts: the total yield  $N$  and the temperature dependent factor  $1/C(T)$  which can be found via integration:

$$C(T) = \int_0^{p_T^{max}} p_T \cdot \exp(-m_T/T) dp_T \quad (6.2)$$

The new form of the Boltzmann distribution is then:

$$\frac{dN^2}{dp_T dy} = N \cdot \frac{p_T \cdot \exp(-m_T/T)}{[T(m_0 + T)\exp(-m_0/T) - T(m_T^{max} + T)\exp(-m_T^{max}/T)]} \quad (6.3)$$

Now the integral  $N$  and the temperature  $T$  are directly the parameters of the fit. The remaining number introduced during the integration  $m_T^{max}$  can be removed via limit:

$$\lim_{m_T^{max} \rightarrow \infty} T(m_T^{max} + T)\exp(-m_T^{max}/T) \rightarrow 0 \quad (6.4)$$

The final form of the Boltzmann distribution used for the fitting is following:

$$\frac{dN^2}{dp_T dy} = N \cdot \frac{p_T \cdot \exp(-m_T/T)}{T(m_0 + T)\exp(-m_0/T)} \quad (6.5)$$

Fig. 6.5 shows the temperature obtained from the fit for different rapidity bins. The dependence on the rapidity is rather strong and experiences rather unphysical decrease for the highest rapidity bins in the case of the  $K^+$ . While the shape of the temperature spectra for  $K^+$  and  $K^-$  seems rather large,

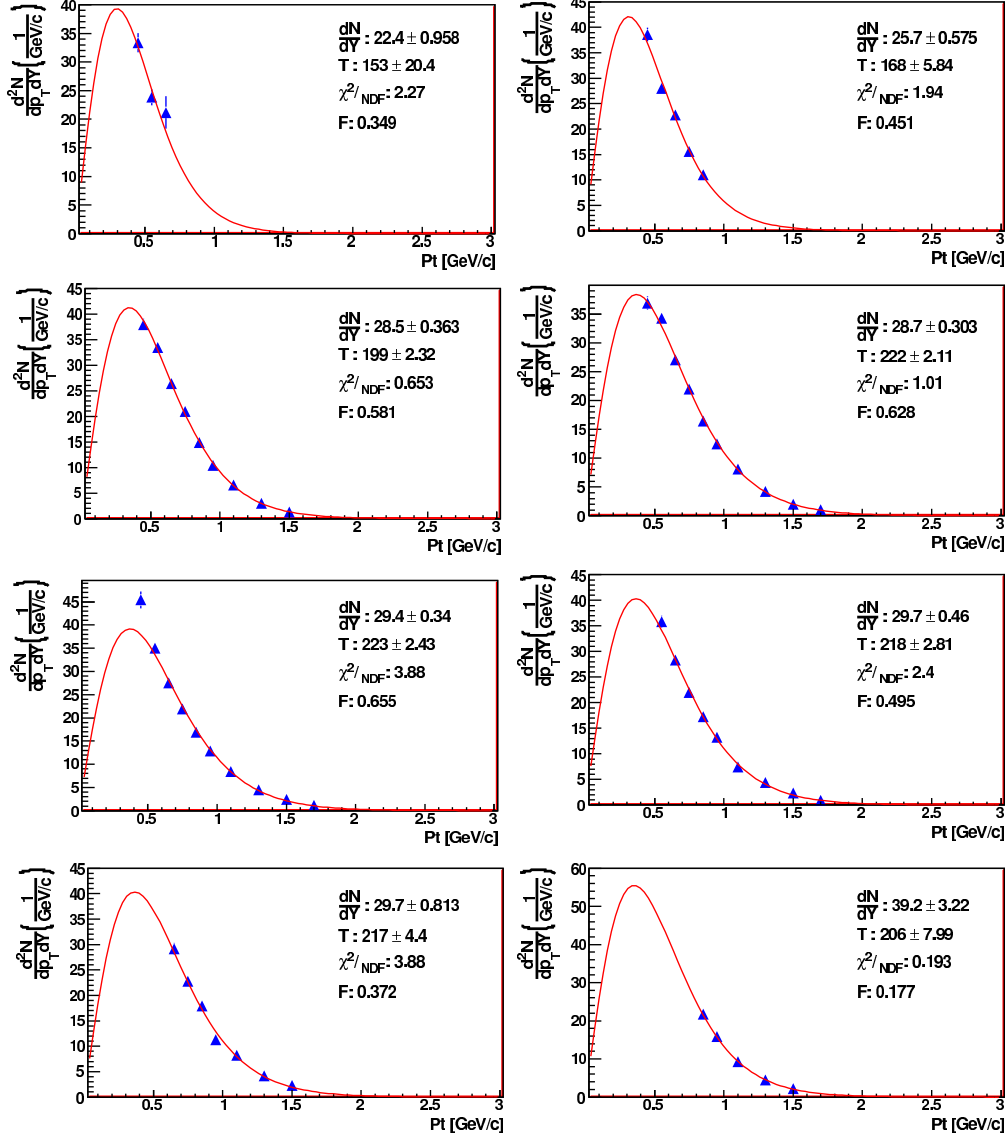


Figure 6.2:  $K^+$  transverse momentum spectra in 8 rapidity bins ordered from the lowest (top left) to highest (bottom right). Data are fitted with Boltzmann function. Quoted values are integral, temperature,  $\chi^2/NDF$  and a factor  $F$  expressing the fraction of the integral carried out by the data points.

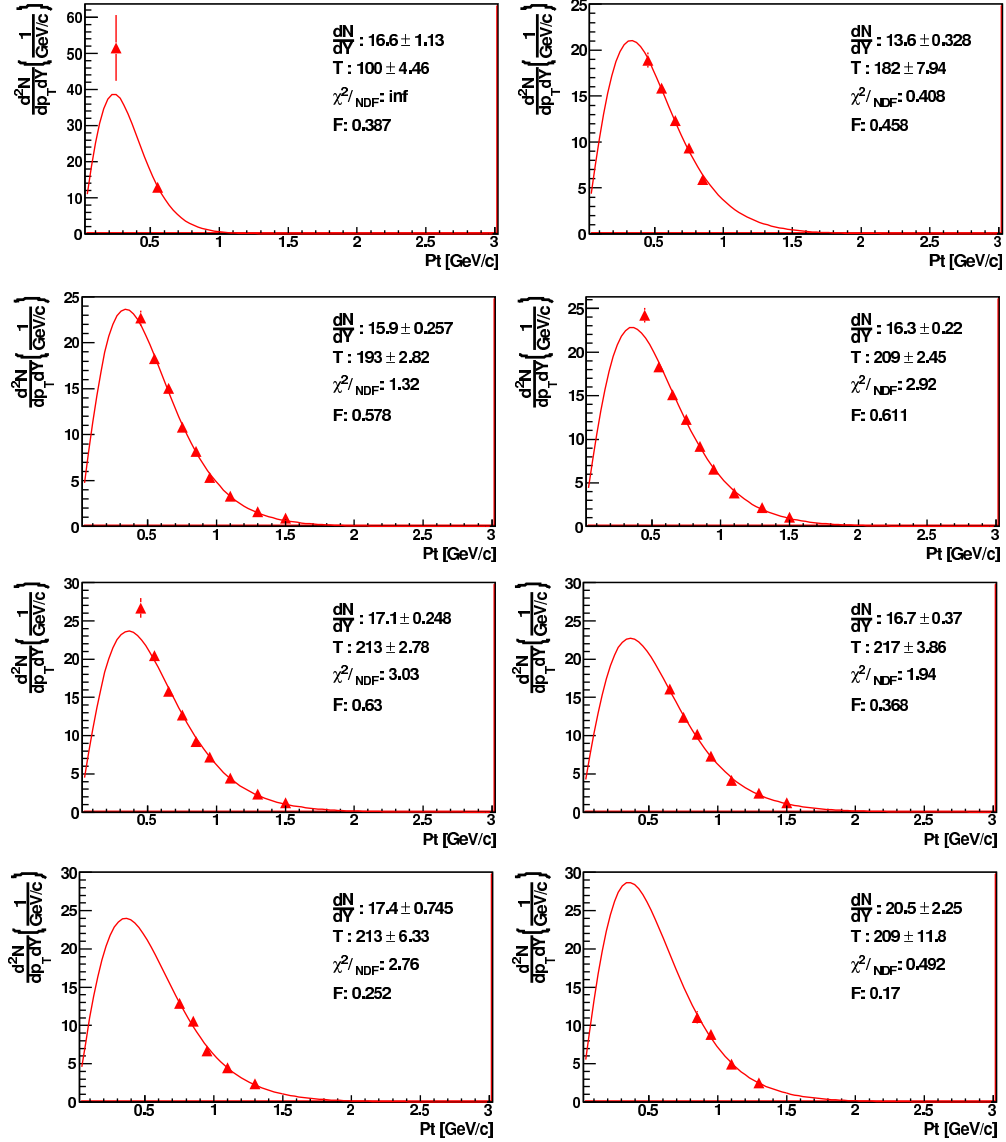


Figure 6.3:  $K^-$  transverse momentum spectra in 8 rapidity bins ordered from the lowest (top left) to highest (bottom right). Data are fitted with Boltzmann function. Quoted values are integral, temperature,  $\chi^2/NDF$  and a factor  $F$  expressing the fraction of the integral carried out by the data points.

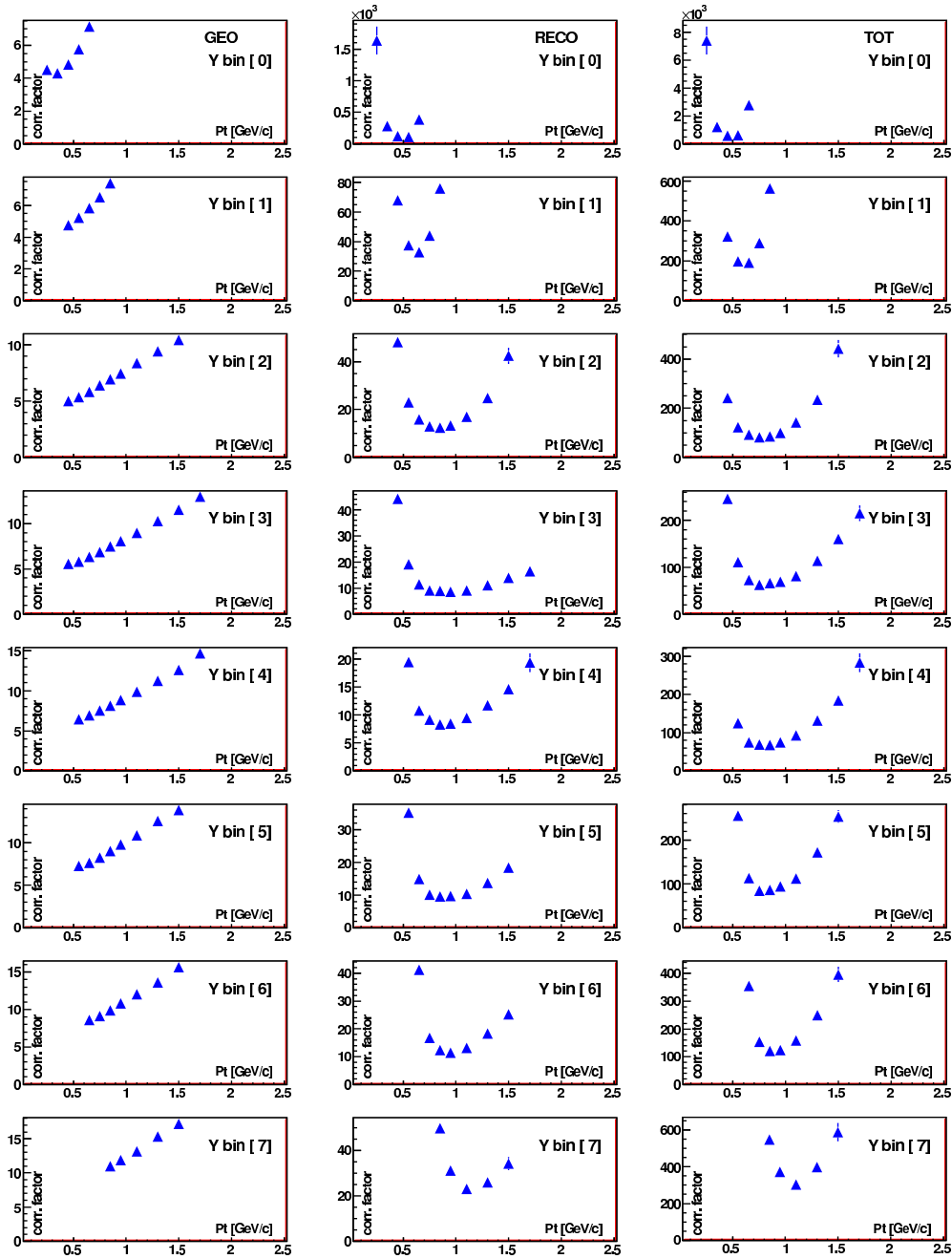


Figure 6.4: Geometrical (left), Reconstruction (middle) and Total (right) correction factors for all rapidity bins. Each rapidity bin is one row. Lowest rapidity bin is on the top, highest on bottom.



the bins where the most of the statistics is located agree within 10 - 20 MeV. Still the strongly pronounced dependence imply possible uncorrected systematical effects. In the section 6.5 will be shown that systematical error on the temperature is on the level of 10 - 20 MeV. The average value is around 220 MeV for  $K^+$  and 215 MeV for  $K^-$ . These two values agree within the errors quoted.

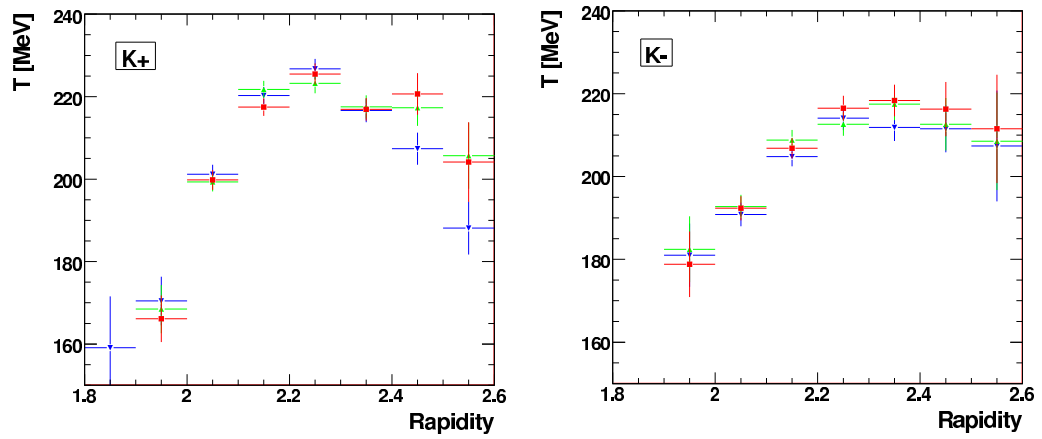


Figure 6.5: *Temperature of the Boltzmann fits for the  $K^+$  (left) and  $K^-$  (right) for 3 different signal extraction methods.*

### 6.3 Transverse mass spectra

While  $p_T$  and  $m_T$  spectra are just a different representations of the same data, different properties are visible when both are displayed. In the  $m_T$  spectra the slope parameter of the spectra that is extracted as a temperature of the Boltzmann fit is most visible. Fig. 6.6 shows the  $m_T$  spectra for both  $K^+$  and  $K^-$ . The spectra were fit with exponential function:

$$\frac{1}{m_T} \frac{d^2N}{dm_T dy} = A \cdot \exp\left(-\frac{m_T}{T}\right) \quad (6.6)$$

where  $A$  is a scale and  $T$  slope of the spectra. The  $m_T$  spectra served only as a check and are not used for further analysis.

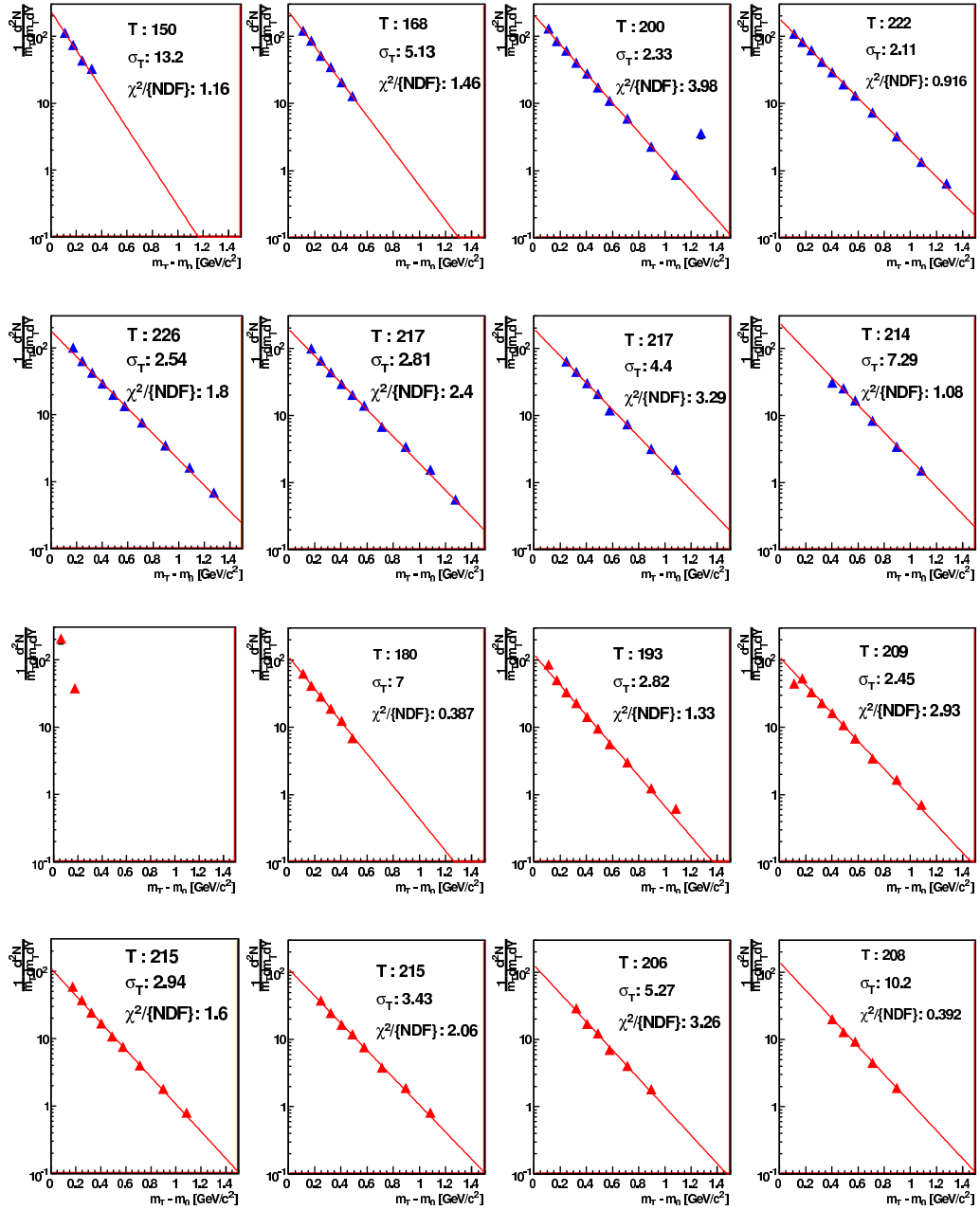


Figure 6.6: Transverse mass spectra for the  $K^+$  (up) and  $K^-$  (down) for 8 rapidity bins.

## 6.4 Rapidity spectrum

Corrected rapidity distributions of the  $K^+$  and  $K^-$  are shown in Fig. 6.7. The errors shown are statistical only. Because the range of the rapidity covered by the measurement is rather narrow the shape of the rapidity distribution as well as the total yield in  $4\pi$  can not be reliably evaluated. The spectra were fitted by a single Gaussian function. The values of the fit were used to evaluate the yields at mid rapidity.

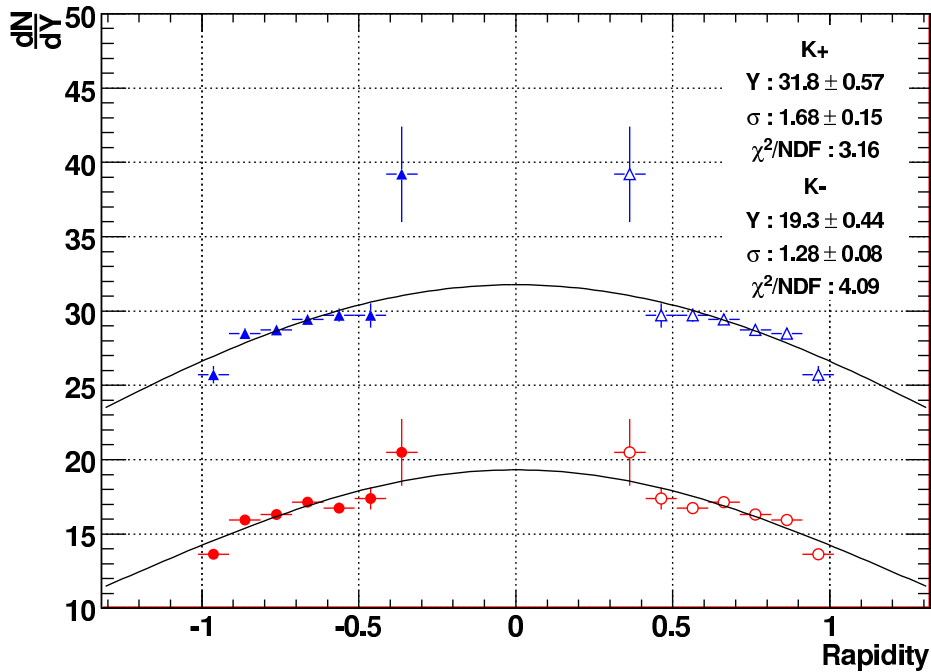


Figure 6.7: Corrected yield spectra for the  $K^+$  (blue  $\blacktriangle$ ) and  $K^-$  (red  $\bullet$ ). The empty symbols indicate the reflected points around the mid rapidity. The errors shown are statistical only. The parameters of the Gaussian fit are quoted.

## 6.5 Systematic error estimation

To be able to evaluate the meaning and impact of the results the systematic error has to be estimated. Given the analysis procedure as described in the

chapters above the following main sources of the systematical errors were identified:

1. Peak extraction.
2. OMC correction.
3. Extrapolation of the  $p_T$  spectra down to  $p_T = 0$  GeV/c.

### 6.5.1 Peak extraction

The uncertainty of the peak extraction procedure has two main sources. One is the shape of the invariant mass peak and the other is the shape of the background below and in the vicinity of the invariant mass distribution. Although the Gaussian function used in 2 of the 3 signal extraction methods does not describe the shape of the signal perfectly the shape of the invariant mass is very well described with the OMC (as shown in Appendix A).

Three different peak extraction methods were used to estimate the systematical error of the peak extraction. In Fig. 6.8 the influence of the different signal extraction methods is manifested as the difference in the mean values of the reconstructed mid rapidity yields.

### 6.5.2 OMC correction

The price paid for the large background suppression is the number of cuts needed to obtain a clean signal. Careful estimation of the influence of different cuts on the final result is therefore obligatory.

To check the stability of the final result each cut was varied around its default position and the distribution of the resulting  $K^+$  and  $K^-$  yields at mid rapidity. The results are presented in Fig. 6.8. The  $dN/dY|_{Y=0}$  distributions were fit around their maximum in the range  $\pm 3$ .

### 6.5.3 $p_T$ spectra extrapolation

The geometry of the CERES TPC together with the topology of the kaon decay did not allow to reconstruct the low  $p_T$  kaons. The extrapolation of the  $p_T$  spectra showed to be the main source of the systematical error of the final kaon yield.

Two different approaches were used for systematic error estimation, Boltzmann fits with fixed temperature and Blast-wave fits with fixed expansion velocity.

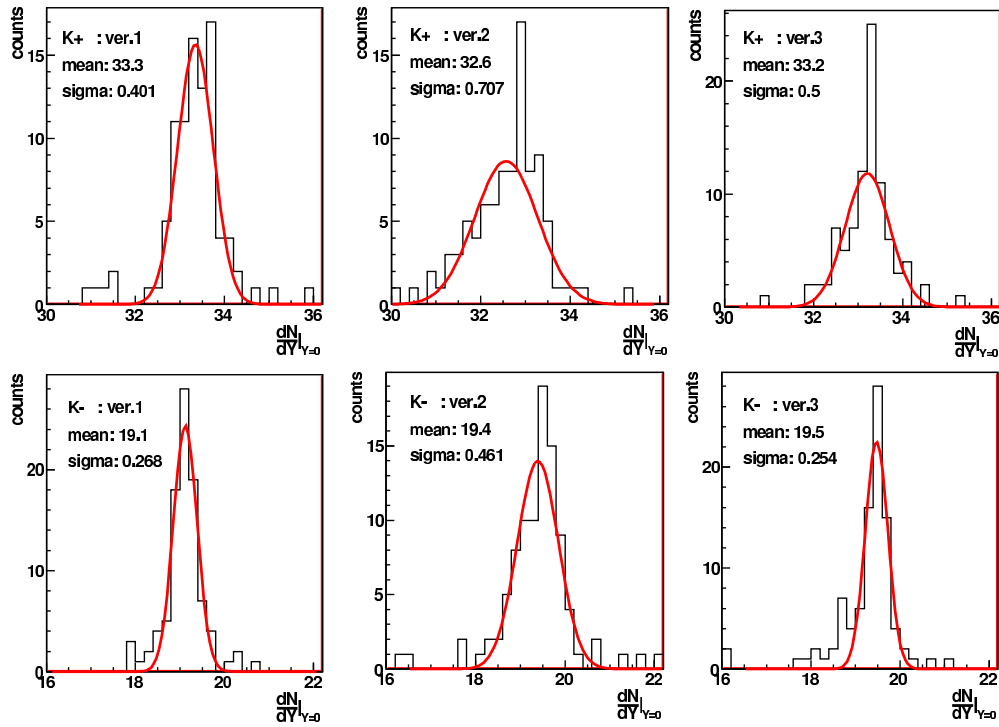


Figure 6.8: *Mid-rapidity yield as a function of different cut combinations for 3 different signal extraction methods for  $K^+$  (upper row) and  $K^-$  (bottom row). Shift of the peak position reflects the influence of the different signal extraction procedures. The width of the distributions reflects the variation of the mid-rapidity yield for cut variations.*

Blast-Wave [54] model predicts a double differential cross section for a given particle species in the form:

$$\frac{dN^2}{p_T \cdot dp_T dy} = A \int_0^{R_G} m_T \cdot K_1\left(\frac{m_T \cosh y_T}{T}\right) \cdot I_0\left(\frac{p_T \sinh y_T}{T}\right) r dr \quad (6.7)$$

where  $y_t = \tanh^{-1}(\beta)$ ,  $K_1$  and  $I_0$  are modified Bessel functions and  $A$  is a normalization constant.  $R_G$  is the transverse geometrical radius of the source at the time the particles decouple from the source.

The transverse velocity  $\beta_\perp$  can be parameterized according to a power law:

$$\beta_\perp(r) = \beta_S \left[ \frac{r}{R_G} \right]^n \quad r \leq R_G \quad (6.8)$$

With this type of profile the numerical value of the  $R_G$  does not influence the shape of the spectra but just the normalization constant. The parameters that are extracted from the fit are then only the thermal freeze-out temperature and surface transverse flow velocity  $\beta_S$ . Assuming uniform particle density an average transverse expansion velocity can be obtained:

$$\langle \beta_\perp \rangle = \frac{2}{2+n} \beta_S \quad (6.9)$$

where  $n$  is the exponent from the equation (6.8).

The final form of the fitting function is then:

$$\frac{dN^2}{p_T \cdot dp_T dy} = A_j \cdot m_T \cdot K_1\left(\frac{m_T \cosh y_T}{T}\right) \cdot I_0\left(\frac{p_T \sinh y_T}{T}\right) r dr \quad (6.10)$$

where  $y_t = \tanh^{-1}(\langle \beta \rangle)$ . This formula can be easily rewritten for transverse mass fits because of the relation of  $p_T$  and  $m_T$ :

$$p_T \cdot dp_T = m_T \cdot dm_T \quad (6.11)$$

In the following part the order parameter  $n$  was set to 1.

The two main parameters of the fit  $\beta_S$  and  $T$  are fixed by different part of the spectra. While the  $T$  is the slope of the spectra as in the case of the Boltzmann function, the  $\beta_S$  describes the behavior of the spectra in the low  $p_T$  part and because of the missing phase space cannot be reliably estimated.

The estimation of the systematical error on the extrapolation of the  $p_T$  spectra was done in the following way. Each  $p_T$  spectrum was fitted with different fixed values of the parameter  $\beta_S$  ranging from 0 to 1 (see Appendix B). Feasible range of  $\beta_S$  was estimated with best populated rapidity bins as  $\beta_S \in (0.2, 0.7)$ . The value of this parameter obtained from a free fit was around  $\beta_S = 0.45$  what compares well to existing results at top SPS energies [54]. Given the nature of the Blast-wave function only the lower limit of the  $p_T$  spectra extrapolation could be estimated with this approach.

Another method was based on fitting the  $p_T$  spectra with Boltzmann function with fixed temperature of 210, 220, and 230 MeV. While the fits with  $T = 220$  MeV were very close to the nominal values the fits with 210 and 230 MeV were used as another source for upper and lower limit on the  $p_T$  spectra extrapolation. As a final check all  $p_T$  spectra were fitted separately with fixed temperature over a broad range to estimate the systematical error on the  $p_T$  extrapolation bin by bin. Fit of the rapidity spectra with systematical errors only confirmed the systematical error estimation based on the previous methods.

## 6.6 Final errors

To estimate the total systematic error originating from the 3 main sources discussed above the possible correlations among them need to be considered. While the systematic error on the  $p_T$  spectra extrapolation is predominantly guided by the range covered by the data and the extrapolation methods and is therefore assumed not to be correlated with the other two sources.

To estimate the systematical error from the signal extraction and OMC correction the results obtained in a systematical study presented in Fig. 6.8 were evaluated in a common way for all 3 signal extraction methods. The final systematical error was estimated as the RMS of the common distributions as shown in Fig. 6.9 and was estimated to 3% both for  $K^+$  and  $K^-$

The final systematical errors of the yield at mid rapidity for  $K^+$  ( $K^-$ ) were estimated as follows:

- Signal extraction & OMC correction : 3% (3%)
- $p_T$  extrapolation: 5% (7%)
- total systematical error : 8% (10%)

The total systematical error was obtained as a sum of the two main components.



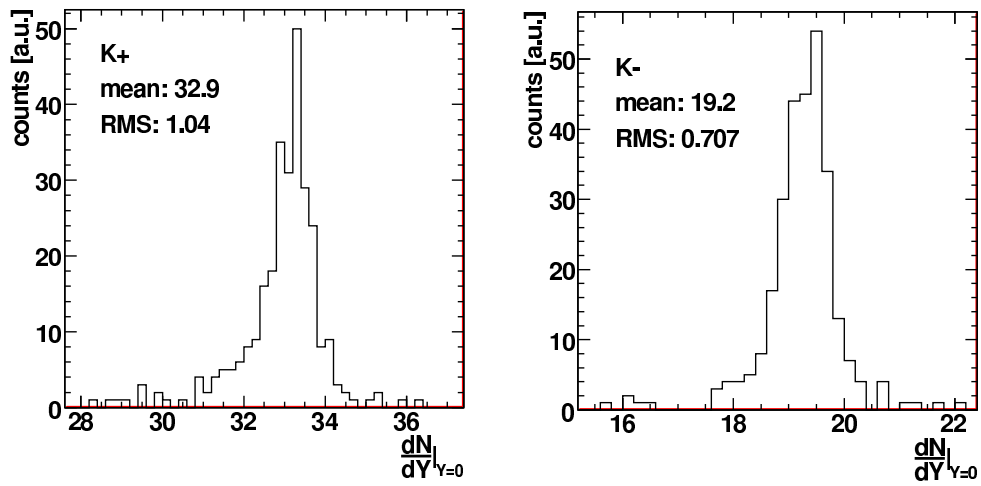


Figure 6.9: Cumulative distribution of the extrapolated mid-rapidity yields for the  $K^+$  (left) and the  $K^-$  (right). Each entry represents one particular cut combination. The mean value and the RMS are quoted.

## 6.7 Final spectra

After the systematical errors estimation the final rapidity spectra for the  $K^+$  and  $K^-$  are presented in Fig. 6.10 and Fig. 6.11, respectively. From the left part of the figures can be clearly seen that the systematical error dominates over the statistical error. As shown before, the main contribution to the systematical error is the extrapolation of the  $p_T$  spectra.

The shape of the spectra can be described by a gauss distribution. The yield at  $dN/dY = 0$  was extracted with fitting a gauss function to one side of the distribution with a fixed mean value  $\langle Y \rangle = 0$ .

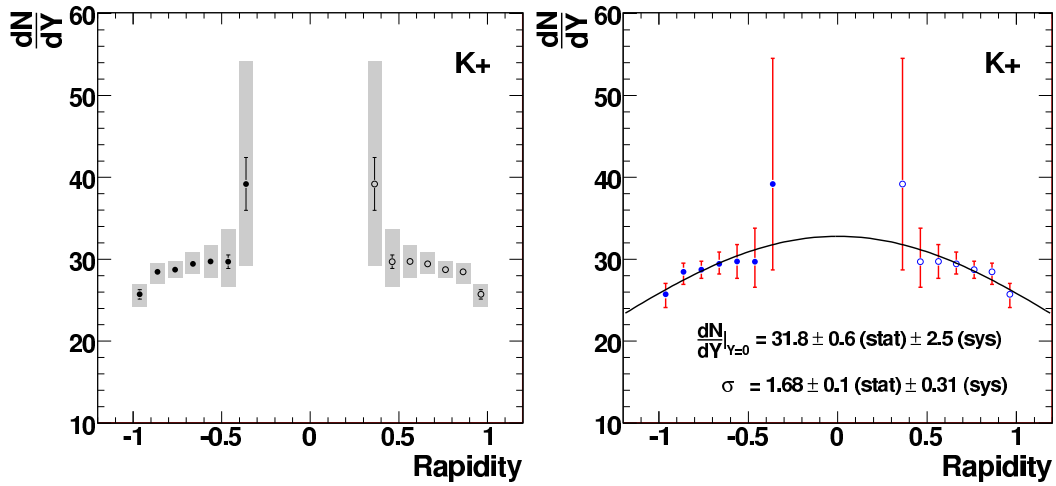


Figure 6.10: *Final  $K^+$  spectra: Left: Statistical (black lines) and systematical (grey bars) errors. Right: Final spectra with total error bar. Quoted is the yield at mid rapidity and width of the Gaussian fit.*

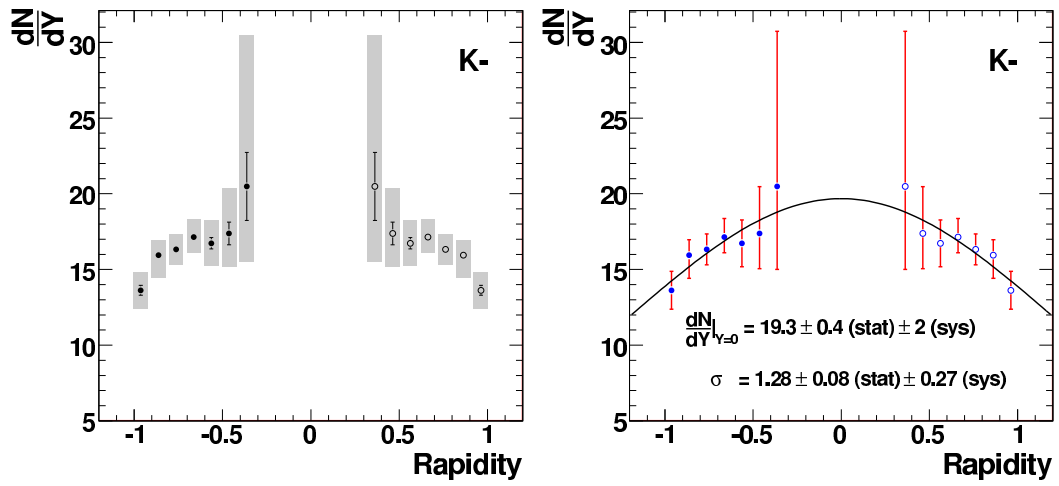


Figure 6.11: *Final  $K^-$  spectra: Left: Statistical (black lines) and systematical (grey bars) errors. Right: Final spectra with total error bar. Quoted is yield at mid rapidity and width of the Gaussian fit.*

## 6.8 Comparison to other experiments

The data at the top SPS energy concerning the the particle yields and particle ratios at mid rapidity are measured by NA44 [48], NA49 [33, 55–58], NA57 [38, 59] and CERES [44]. While only NA44 and NA49 measured charged kaons, the comparison to  $K_S^0$  measurements by NA57 and CERES can still be done.

Before comparison of the results presented to other experiments or theoretical predictions can be made, one has to assure that different systems and different centralities used in different experiments are scaled properly. The scaling of the results is based on the participant model also known as Glauber model [60–62]. The number of participants for different systems and centralities were obtained using the web interface implementation [63] of this model.

experiment	system	centrality [%]	N participants
NA44 , NA57	Pb+Pb	3.7	364
NA49	Pb+Pb	5	357
CERES	Pb+Au	7	336

Table 6.1: *Number of participants obtained with Glauber model for top SPS energy for different systems and centralities.*

All following comparisons will be made for the top SPS energy of 158 AGeV, therefore no scaling is needed to compensate for different CMS energies.

### 6.8.1 NA49 and NA44

NA49 is the only experiment that measured both  $K^+$  and  $K^-$  over a broad rapidity range at the top SPS energy. The reconstruction technique is based on the  $dE/dx$  measurements. The rapidity covered ranges from -0.2 to 1.8. The comparison of the rapidity distributions for  $K^+$  and  $K^-$  of NA49 and the results presented in this thesis is shown in the Fig. 6.12. Because of the slightly different system sizes (Pb+Pb versus Pb+Au) the NA49 points were scaled by factor 0.94 obtained with the Glauber model.

NA44 spectrometer was designed to measure one and two particle momentum distributions near mid rapidity. Because of the geometry the  $p_T$ - $Y$  phase space is not smoothly populated. Each measurement at given momentum and polar angle of the particles measured results into a narrow window in the  $p_T$ - $Y$  plane. The NA44 yields of  $K^+$  and  $K^-$  were scaled by a factor 0.92 (based on the number of participants).

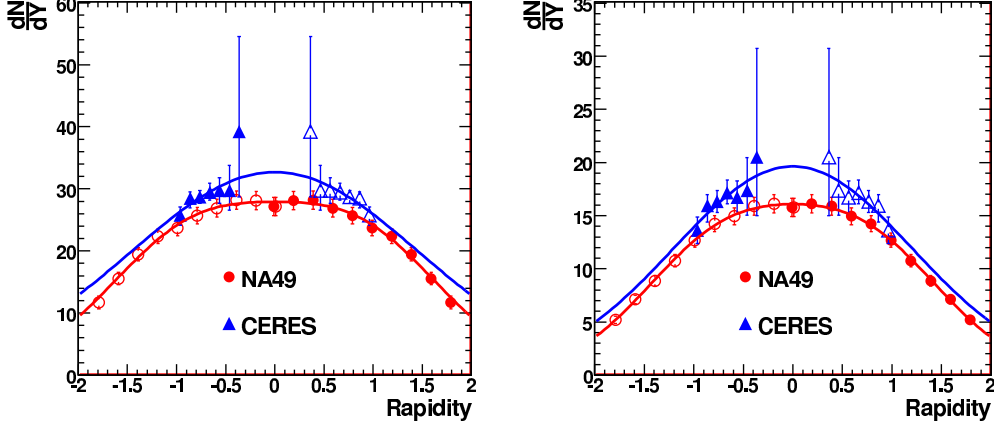


Figure 6.12:  $K^+$  (left) and  $K^-$  (right) rapidity distribution comparison between NA49 (red) and this result (blue). The error bars show statistical and systematical errors added in quadrature for both experiments.

The yields at mid rapidity and widths of the data are shown in the Table 6.2.

exp.	system	results
NA49	$K^+$	$27.8 \pm 0.3$ (stat) $\pm 1.5$ (sys)
NA44	$K^+$	$25.5 \pm 0.2$ (stat) $\pm 1.4$ (sys)
CERES	$K^+$	$31.8 \pm 0.6$ (stat) $\pm 2.5$ (sys)
NA49	$K^-$	$15.8 \pm 0.2$ (stat) $\pm 0.8$ (sys)
NA44	$K^-$	$14.2 \pm 0.5$ (stat) $\pm 0.9$ (sys)
CERES	$K^-$	$19.3 \pm 0.4$ (stat) $\pm 2.0$ (sys)
NA49	$K^-/K^+$	$0.566 \pm 0.008$ (stat) $\pm 0.04$ (sys)
NA44	$K^-/K^+$	$0.557 \pm 0.020$ (stat) $\pm$
CERES	$K^-/K^+$	$0.556 \pm 0.008$ (stat) $\pm 0.01$ (sys)

Table 6.2: Comparison of the results on charged kaons yields and ratio to yields of NA49 and NA44.

The errors on the results of all three experiments are dominated by systematical errors. Within the errors quoted the results of kaon yields of NA49 and CERES are consistent, although the role of the interpolation of the mid-rapidity yield should be considered. NA49 uses a double gauss fit to describe the flatter mid rapidity part of the spectra. To fit the CERES data only a single gauss fit was employed as rather narrow acceptance did not allow

for more detailed fit functions. Still, one could argue that some flatterings is visible close to mid rapidity, however, quantitative conclusions can not be drawn because of large errors. Still, a double gauss fit would yield somewhat smaller values at  $y=0$  and cosequently to better agreement between CERES and NA49.

The difference in yields between NA44 and CERES is at the level of 1.5  $\sigma$ . Concerning the ratios all experiments agree very well.

### 6.8.2 Comparison of $K_S^0$ measurements from CERES and NA57

Because of the isospin symmetry between  $u$  and  $d$  quarks the yields of  $K^+$ ,  $K^-$ ,  $K_S^0$  and  $K_L^0$  can be compared in a simple relation.

$$N(K_S^0) + N(K_L^0) = N(K^+) + N(K^-) \quad (6.12)$$

Because the  $K^0$  consists of 50%  $K_S^0$  and 50%  $K_L^0$  and in most experiments only  $K_S^0$  are reconstructed the more common way to compare the Kaon yields is following:

$$N(K_S^0) = \frac{N(K^+) + N(K^-)}{2} \quad (6.13)$$

$K_S^0$  at to top SPS energy were measured by CERES [44] and NA57 [59]. While the centrality used in the analysis of  $K_S^0$  in the CERES is the same as the centrality of the analysis presented here, the NA57 data were taken at 3.7% centrality at Pb+Pb so their results and spectra are scaled by a factor 0.92.

The spectra of scaled charged kaons to CERES and NA57 neutral kaons are shown in Fig. 6.13.

exp.	system	results
NA57	$K_S^0$	$28.0 \pm 2.2$ (tot)
CERES	$K_S^0$	$21.2 \pm 0.9$ (stat) $\pm 1.7$ (sys)
CERES	$(K^+ + K^-)/2$	$25.6 \pm 0.3$ (stat) $\pm 1.6$ (sys)

Table 6.3: Comparison of the results of scaled charged kaons yields to NA57 and CERES results on neutral kaons.

Comparing of the CERES results on charged kaons to NA57 yields in two observations. While the yields do agree within the errors, the shape of the

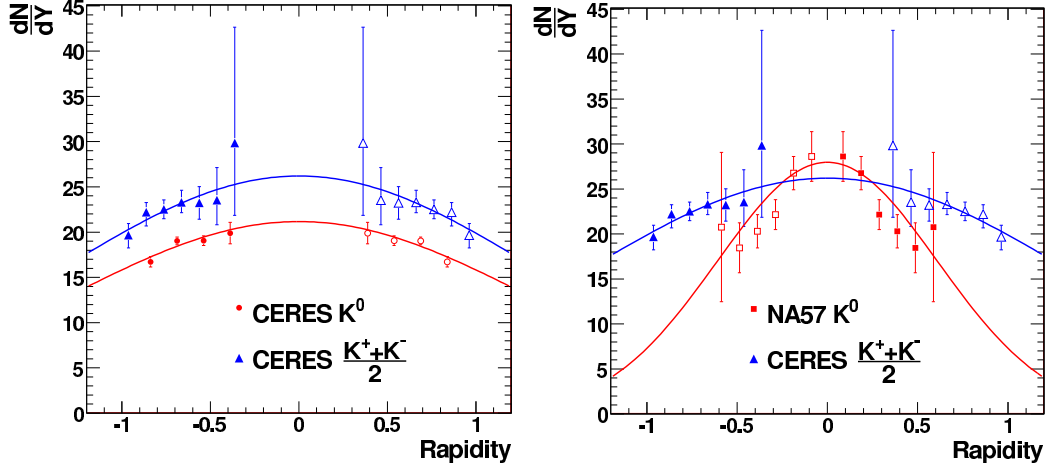


Figure 6.13: Comparison of the scaled rapidity distributions for charged kaons to  $K_S^0$  distributions from CERES (left) and NA57 (right).

spectra is very different. Within the rapidity range common to both experiments the data points do partially agree although a systematic difference in the slope is visible.

Results of the charged and neutral kaons within CERES experiment disagree on the level of  $1.5 \sigma$ . While the shape of the spectra is very similar, the absolute values differ by nearly 20%.

### 6.8.3 K to $\pi$ ratios

To be able to compute the  $K^+/\pi^+$  ( $K^-/\pi^-$ ) ratios, first the number of pions at mid-rapidity has to be estimated. This estimation was based on the NA49 measurement [33] of charged pions. The pion yields are scaled by a factor 0.94 based on Glauber model. Expected  $\pi^+$  ( $\pi^-$ ) multiplicities for CERES at mid-rapidity are  $dN/dY(\pi^+) = 160 \pm 10$  and  $dN/dY(\pi^-) = 165 \pm 10$ .

Using these values as an input together with measured mid-rapidity yields of  $K^+$  and  $K^-$  results into following ratios:

- $K^+/\pi^+ = 0.199 \pm 0.02$
- $K^-/\pi^- = 0.117 \pm 0.014$

The errors quoted contain statistical and systematic errors added in squares.

Comparison to the existing data in the form of excitation function is shown in Fig. 6.14.

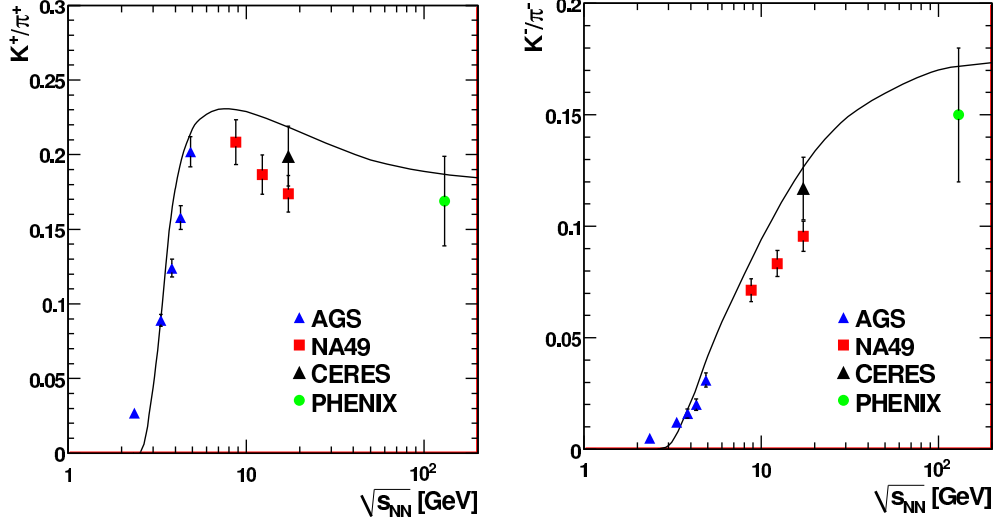


Figure 6.14: Excitation function of the  $K^+/\pi^+$  (left) and  $K^-/\pi^-$  (right). Result of this measurement is shown as ( $\blacktriangle$ ). Other data [64] [65] (AGS), [33] (NA49), [48] (NA44), [66] (PHENIX). The line presents the thermal model calculations [67].

#### 6.8.4 $K^-$ to $K^+$ ratio

The main advantage of particle ratios is that large fraction of the systematical error cancel out - especially for charge conjugate ratios.

The  $K^-$  to  $K^+$  ratio as a function of rapidity is shown in Fig. 6.15. The fluctuations of the ratio are rather large. The systematical error was estimated via different signal extraction procedures. The value of the total  $K^-$  to  $K^+$  ratio was estimated with constant line fit:  $K^-/K^+ = 0.556 \pm 0.008(\text{stat}) \pm 0.01(\text{sys})$ .

The  $K^-/K^+$  ratio as a function of  $\sqrt{s}$  is shown in Fig. 6.16. The reason for the strong energy dependence at lower energies is the quark content of  $K^+$  ( $u\bar{s}$ ) and  $K^-$  ( $\bar{u}s$ ) and reflects the quark-to-antiquark ratio inside the fireball. While  $K^-$  contains two quarks that were not present in the system prior to collision, the  $K^+$  contains only one "new" quark. Also the production of the  $\Lambda$  baryon ( $uds$ ) competes with  $K^-$  production, while the  $\bar{\Lambda}$  ( $\bar{u}\bar{d}\bar{s}$ ) is strongly suppressed because it contains 3 "new" quarks.



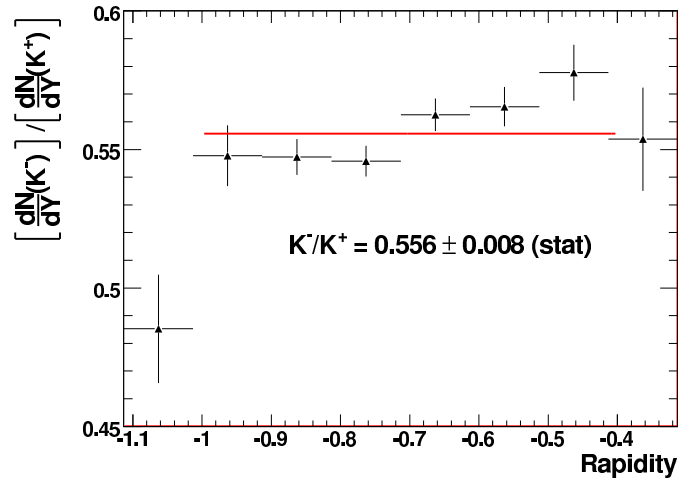


Figure 6.15:  $K^-$  to  $K^+$  ratio as a function of rapidity.

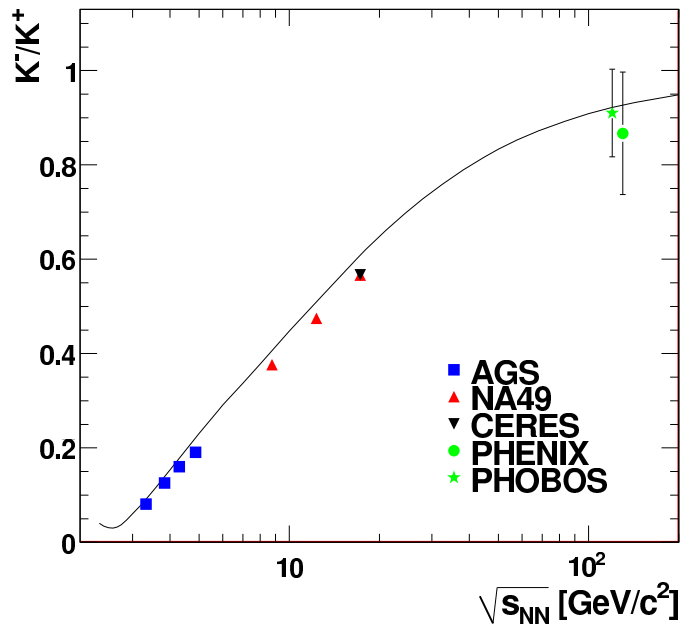


Figure 6.16: Excitation function of the  $K^-$  to  $K^+$  ratio. The line presents the thermal model calculations [67].

### 6.8.5 Thermal model

Fit of the thermal model to most of the existing data at the top SPS energy is shown in Fig. 6.17. The fit values of the two parameters temperature and baryochemical potential are:  $T = 160 \pm 5$  MeV ,  $\mu_b = 240 \pm 18$  MeV.

The yields of charged kaons together with scaled charged pion yields can be compared to the thermal model prediction in the means of 3 particle ratios:  $K^-/K^+$ ,  $K^+/\pi^+$  and  $K^-/\pi^-$ .

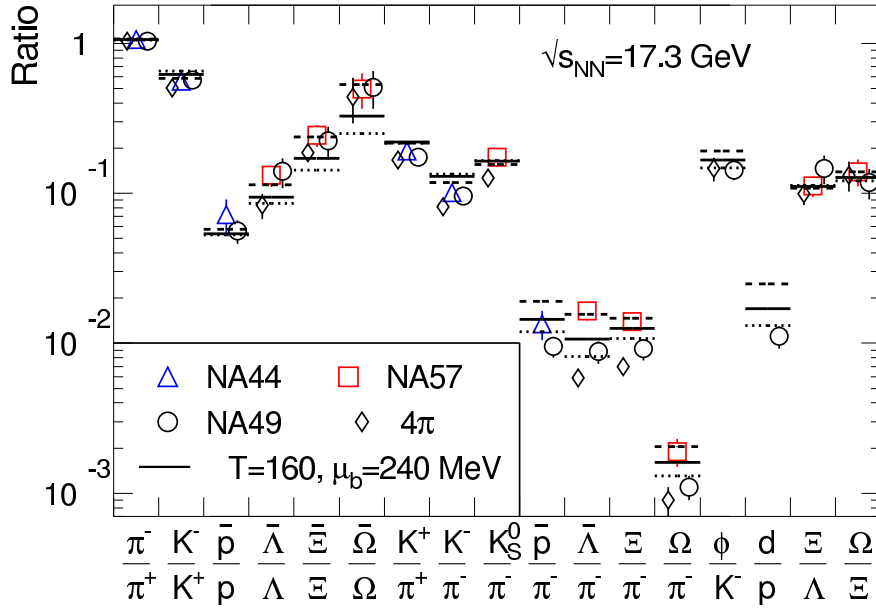


Figure 6.17: *The ratios of hadron yields at mid rapidity compared with a thermal model fit at the top SPS energy. Full line shows the combined fit to NA44, NA57 and NA49 measurements. [67].*

The comparison of the thermal model prediction to the measured yields is shown in the table 6.4

ratio	TM fit	measurement
$K^-/K^+$	0.623	$0.556 \pm 0.008$ (stat) $\pm 0.01$ (sys)
$K^+/\pi^+$	0.221	$0.199 \pm 0.02$ (tot)
$K^-/\pi^-$	0.129	$0.117 \pm 0.014$ (tot)

Table 6.4: *Comparison of the particle ratios to the fit value of the thermal model (global fit for NA44 + NA57 + NA49).*

The differences between the thermal model fits and results on charged

kaons are about  $3\sigma$  for the  $K^-/K^+$  ratio. This is partially due to the small error of the measurement. Overall, as shown in Fig. 6.16 the thermal model describes the measured data of  $K^-/K^+$  ratio rather well.

The measured  $K/\pi$  ratios do agree with the thermal model prediction within the  $1\sigma$  error. However it should be mentioned that the same level of agreement is observed with results of NA44 and NA49. While the measurement of the  $K/\pi$  ratios is dependent on the input of another experiment (NA49) and larger systematical errors could be argued, the  $K^-/K^+$  ratio is a rather well defined measurement with small systematical errors.

It needs to be mentioned at this point that the current situation at the top SPS energy is somewhat complicated because as shown in [67], the thermal fits of the two separate data sets (NA44 + NA57 versus NA49) give somewhat different results. On the other hand the uncertainties of the experimental data do not allow for a strong conclusion on physics beyond the thermal model predictions.

## 6.9 Discussion

The main motivation for the analysis presented in this thesis was to provide a measurement of charged kaon yields based on a different method and therefore with different systematic error sources than the commonly used approach based on  $dE/dx$  and TOF measurements. Reconstruction of the charged kaons via their decay into 3 pions in the environment of a heavy ion collisions is rather unique approach and was up to now used only by NA35 [68]. The requirement for such a measurement is large statistics because the geometrical and reconstruction efficiency is rather low at about 4 (2.5) reconstructed  $K^+$  ( $K^-$ ) per 1000 central Pb+Au collisions. The main source of the systematical error of the kaon yields is the extrapolation of the transverse momentum spectra to  $p_T = 0$ .

The obtained results were compared to the existing experimental results at the top SPS energy in the terms of mid rapidity yields and particle ratios, as well as to a thermal model predictions. The values for the mid rapidity yields of  $K^+$  and  $K^-$  are partially consistent with NA49 and inconsistent with NA44 of the level of  $1.5\sigma$ . The shapes of the kaon spectra in CERES and NA49 agree rather well.

Comparison of scaled  $K^+$  and  $K^-$  yields to  $K_S^0$  measurement is not consistent with CERES results on the level of  $1.5\sigma$  and agrees rather well with NA57 result. However, the shapes of the spectra lead to very good agreement within the CERES results and strong disagreement between CERES and NA57 measurements.

The  $K^-/K^+$  ratio is consistent with NA49 and NA44 measurements. The rather large variation of the yields of charged kaons obtained with CERES, NA49 and NA44 but on the other hand a good agreement of the  $K^-/K^+$  ratios leaves a question mark on the possible underestimation of the systematical errors in different experiments. Rather conservative approach to the estimation of the systematical errors on the results presented in this thesis was used to minimize the risk of the underestimation of the systematical errors.

The difference on the  $K^-/K^+$  ratio between the thermal model prediction and result presented here is approximately  $3\sigma$ , but as mentioned before this does not represent a serious discrepancy in this case. The result on  $K^+/\pi^-$  ratio is in agreement with existing data and the thermal model prediction. Because of rather large errors no strong conclusion can be drawn and the question about the  $\sqrt{s_{NN}}$  dependence of the  $K^+/\pi^-$  remains open.

# Chapter 7

## Fast TRD development

### 7.1 Motivation and requirements

One of the main tasks of the detectors in the particle physics experiments is identification of the particles produced in the collision. For different energies and particle species different techniques are applied. Usually an identification of electrons (and positrons) from the charged pions which make up about 85% of the particles produced in the collision is needed. On the other hand the electrons are often the probes for rare particles, so a high pion suppression of about 100 - 1000 is usually required.

There are several physics processes used for electron - pion separation. The most common are:

- Ionization losses in a gas chambers - this method usually does not give a very high separation and is limited to maximal momentum of 2 - 4 GeV/c because of relativistic rise of the energy losses of pions. For good performance rather large detectors are needed.
- Shower detectors in which the full energy of the electron is deposited (Electro-magnetical calorimeters - ECAL). This method is based on the fact that electron (event though it does not interact strongly) is very light what yields in large interaction cross sections. ((Hadrons because of their large mass do not deposit a large fraction of their energy in the electromagnetic interaction and therefore produce shower only in the hadron-nucleus interaction. As the cross section of this process is rather small hadrons have to pass much more material to produce a shower - usually in a dedicated hadron calorimeter located behind the ECAL)))
- Cherenkov radiation in a so called RICH (Ring Imaging Cherenkov) detectors - may yield very high electron - pion separation (pion sup-

pression by a factor 100 and more). At higher momenta (depending on the gas composition) 6 - 10 GeV/c muons and pions start to reach super luminal velocities (in the gas medium) and produce Cherenkov radiation as well.

- Transition radiation produced by a particle when crossing a boundary of two different dielectric media. Reasonable yields (of order of  $\alpha$  per boundary crossing) and energies of the produced radiation (few keV X-rays) are reached only for ultra relativistic particles with  $\gamma > 1000$ . For electrons this means energies of 2 GeV/c and larger. For pions the threshold is around 100 GeV/c what is also an approximate limit for this method.

From the list above can be seen that none of the methods alone covers whole momentum range so usually more than one detector capable of electron pion separation is used when a precision measurements of rare probes (e.g.  $J/\Psi$ ) should be done. For the CBM experiment three of the mentioned techniques - RICH, TRD and ECAL should serve to this purpose.

Apart from physics requirements the detector needs to fulfil many criteria to be suitable for the modern particle physics experiment. Large multiplicities and high interaction rates especially in heavy ion experiments demand very fast detectors with high granularity hand in hand with high detection efficiencies and low material budget (in terms of radiation length).

Different experimental conditions indeed imply a different design of a given detector. In the following chapters the development studies of a fast Transition Radiation Detector for a CBM (Compressed Baryonic Matter) experiment [69] which will be a part of the future FAIR (Facility for Anti-proton and Ion Research) facility in Darmstadt and should come to an operation around 2015, will be discussed.

## 7.2 CBM experiment

CBM is a fixed target experiment which will study ion collisions with the beam energy range of 2 - 35 AGeV (GeV per nucleon).

In comparison to contemporary high energy particle experiments at the Relativistic Heavy Ion Collider (RHIC) at BNL and at the (future) Large Hadron Collider (LHC) at CERN which produce the matter with very high temperatures, but very low baryochemical potentials, the energy range of the CBM experiment allows to reach the highest baryon densities achievable nowadays in laboratory.

The main physics goal of the CBM experiment is to study the equation-of-state of nuclear matter under very high (energy) density. This includes the search for the phase boundary between hadronic and partonic matter, the critical endpoint and the search for signatures of the onset of the chiral symmetry restoration at high net-baryon densities.

The experimental observables are the yields and phase-space distributions of newly created particles and their correlations and fluctuations. The different particle species probe different stages of the fireball depending on their mass, energy, production mechanism, interaction cross sections and decay channels.

Particles containing heavy quarks are created in the early stage of the heavy ion collision. The charmed hadrons are of particular interest as the FAIR energies are close to the threshold for the charm-anticharm pair production. Therefore the yield and phase-space distributions of the charmed hadrons are expected to be particularly sensitive to the conditions inside the early fireball.

The CBM detector itself is supposed to allow to exploit the physics potential of nucleus-nucleus collisions at FAIR. Basic properties include large geometrical acceptance both for hadrons and leptons. A key feature will be the capability to perform measurements of the rare probes such as D-mesons and charmonium requiring high interaction rates up to  $10^7$ Hz. Multiplicities up to  $\sim 1000$  charged particles per gold-gold central collision are expected. Such conditions require unprecedented detector performance in terms of read-out speed and radiation hardness.

A schematic view of the CBM setup is shown in Figure 7.1. Following the beam direction the main components of the CBM experiment are; Silicon Tracking Station (STS) - multilayer silicon pixel/strip detector placed in a dipole magnet of bending power 1 Tm. STS is followed by Ring Imaging Cherenkov Detector (RICH) after which come 3 stations of the Transition Radiation Detector (TRD), Time Of Flight detector (TOF) and finally the Electromagnetic Calorimeter (ECAL). The length of the whole setup is  $\sim 12$ m.

### 7.3 Basic properties of transition radiation and its detection

Transition radiation (TR) is produced when a charged particle traverses a boundary between two materials of different electrical (optical) properties.

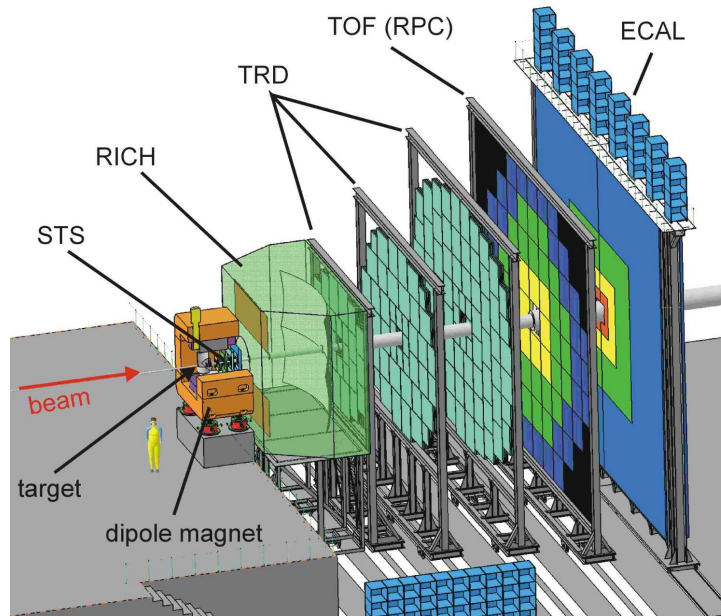


Figure 7.1: Schematic view of the CBM detector

Its existence was first proposed by Frank and Ginsburg in 1945 [70]. It was first measured in the region of visible light and UV and long forgotten afterwards.

In its nature TR is different from energy loss of a particle due to collisions with atoms of the medium where the energy lost is emitted by the particle itself. In case of TR it is the polarization of the medium which is the source of the radiation.

TR is similar to the Cherenkov radiation but with the main difference being the absence of the threshold effect ( $v > c/n$ ). For practical purposes a threshold value of the Lorentz factor  $\gamma = 1000$  ( $\gamma = 1/\sqrt{1 - v^2/c^2}$ ) is considered as below this value the yield of TR produced in the keV range that is used for particle identification falls steeply. This implies that for the particles with energies within 1 - 100 GeV only electrons will produce TR and therefore transition radiation detectors are useful for electron - pion separation in high energy physics.

In practice the most often used media for a radiator are polypropylene foils, fibers or foams placed in gas, usually air. In the case of foil based radiator one speaks of regular radiator, while in the case of fibers or foams the term irregular radiator became common. While it was shown [71] that regular radiator offers better performance in terms of the ratio of the TR



yield per total amount of radiator material, many experiments use irregular radiators mainly for their mechanical properties and easier handling.

As the number of TR photons emitted per one boundary between two different media is proportional to fine structure constant  $\alpha \approx 1/137$  usually  $\sim 100$  foils are used.

## 7.4 TRD in the CBM experiment

Design and physics goals of the CBM experiment impose challenging requirements on all the subdetector systems.

One of the main requirements is ability to handle rates of heavy ion collisions up to 10 MHz. Another concern is the high particle multiplicity especially in the region close to the beam pipe. Intensities of charged particles up to 100 kHz per  $\text{cm}^2$  in Au-Au collision at 25 AGeV beam energy at the position of the first TRD station are expected. Under such conditions the performance of a detector needs to be studied carefully.

There are several physics requirements imposed on the TRD. The main one includes the electron to pion separation by factor 100 or more. Also tracking abilities of the TRD are of high importance as the TRD connects STS tracks to TOF and ECAL detectors and so has a large impact on the particle identification beyond the electron - pion separation.

It is envisaged that the TRD within the CBM experiment will be organized in layers separated into 3 stations. Each station would then contain 3 or 4 separate TRD layers - altogether 9 or 12 layers.

An important issue is also the total cost of the detector. The total area of the detector for the 4 layers per station and 3 stations placed at 4, 6 and 8 meters from the target is  $\sim 350 \text{ m}^2$ .

At the current stage two different designs of the TRD detector within the CBM experiment are being studied. One is the ALICE like TRD [72] MPWC (multiwire proportional chamber) based. The other technology is ATLAS like TRD (ATLAS TRT - Transition Radiation Tracker) [73] with straw tubes. Both designs bring some advantages and disadvantages. In the rest of this part of the thesis the MPWC-based TRD will be studied.

## 7.5 CBM TRD basic layout

From the technical point of view, the layout of a single MWPC based TRD chamber consists of radiator and MPWC itself. In more details the TRD chamber composition looks as follows:

- Radiator:  $\sim 1$  cm of polypropylene (PP) or polyethylene (PE) fibers/foam or PE  $\sim 100$  foil/gap layers.
- Foil: thin aluminized Mylar foil of  $20\mu\text{m}$  which serves as a cathode and also seals the gas volume of the MWPC chamber.
- Gas volume:  $\sim 6 - 10$  mm thick layer of the so called active gas (for a Xe/CO<sub>2</sub> mixture) serves for deposition of the ionization energy losses of the charged particles crossing the chamber and also for absorbing the TR photons created in the radiator.
- Cathode and Anode wires: gold plated tungsten wires of  $20\mu\text{m}$  diameter placed symmetrical in the active gas between the mylar foil and pad plane with a pitch of 2 - 4 mm.
- Pad plane: Sandwich of segmented cathode with a pad size  $\sim 1 - 10$  cm<sup>2</sup> with reinforcement and electronics.

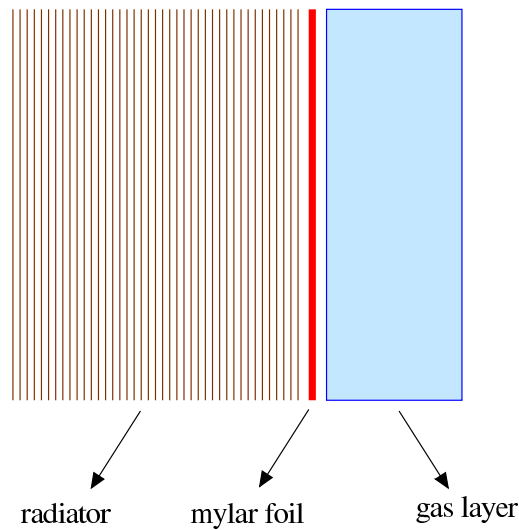


Figure 7.2: *Layout of the simulated TRD*

## 7.6 MC Simulations

Both simulations and measurements are needed to study the feasibility of such a concept.

In the framework of this thesis a stand alone Monte Carlo C++ program was developed to study the electron - pion separation properties for a wide variety of possible radiator - detector configurations.

For the simplicity a following detector structure was used (see Fig.7.2):

- regular radiator composed of polypropylene foils placed in air
- mylar foil
- gas layer - Xe/CO<sub>2</sub> (85/15)

The pad plane, anode and cathode wires were omitted as the simulation did not include the microscopical processes like avalanche processes, space charge, signal induction or electronics response.

For this simulation the following physics processes were included:

- energy deposition of electron and pion in the gas detector via ionization of the gas
- production of transition radiation by an electron in the radiator
- absorption of the transition radiation in the radiator and mylar foil
- absorption of TR in the gas detector
- production of secondary electrons (delta electrons) and possibility that only part of their energy is deposited in the gas volume of the detector.

These simulations did not include the effects of high rates, double track resolution, tracking inefficiencies or TR propagation from layer to layer.

Ionization energy losses were obtained via random sampling the number of primary collisions and of the spectrum of the energy transfer in these collisions.

The number of primary collisions in the gas volume were computed as follows:

$$N_C(p) = lCF(p) \tag{7.1}$$

where  $l$  is the thickness of the gas volume,  $C$  is a constant referring to the number of collisions per mm for MIP (Minimum Ionizing Particle) and was set to 19.3 (GEANT3),  $F(p)$  is the factor relative to MIP obtained via parameterization of the Bethe-Bloch formula (extracted from GEANT3).

It was assumed that the spectral shape of the energy transfer is independent of  $\gamma$  and only the number of primary collisions depends on  $\gamma$ . The parameterization used follows the one proposed by the authors of [74] and

corresponds to Fermi plateau 1.61 times larger with respect to MIP (compared to 1.55 in GEANT3).

A random sampling of parameterized integral spectrum of the energy transfer in primary collisions was used. The lowest value of the energy transfer was set equal to the lowest ionization potential for Xe which is  $I_0 = 12.1$  eV.

If an electron with energy higher than 10 keV was produced, it was considered a  $\delta$ -electron and its range was computed according to [75]:

$$R(E) = AE \left( 1 - \frac{B}{1 + CE} \right) \frac{1}{\rho} \quad (7.2)$$

where  $E$  is the energy of the  $\delta$ -electron,  $A = 5.37 \times 10^{-4} gcm^{-2} keV^{-1}$ ,  $B = 0.9815$ ,  $C = 3.123 \times 10^{-3} keV^{-1}$ ,  $\rho$  is the density of the gas. If the range of such an electron was longer than its trajectory inside the gas volume only a part of the energy of the delta electron was deposited inside the gas volume was added to the total energy losses of the primary particle. All delta electrons were considered to be created in the direction of the primary particle.

For simulations of the TR a regular (foil based) radiator was used. This choice was primarily guided by the better radiation length - to - TR yield ratio [71] and as well by the fact that a regular radiator is easier to simulate.

To obtain energy loss of an electron via TR following parameters are needed: probability to produce a TR photon, spectrum of the TR photons absorbed inside the gas volume and probability of the photon to be absorbed inside the gas volume.

The energy spectrum of TR photons produced by a charged particle with relativistic factor  $\gamma$  in a regular radiator composed of  $N$  foils of thickness  $l_1$  separated by gaps of width  $l_2$  per energy  $\omega$  of the produced TR photons looks as follows[76]:

$$\frac{dW}{d\omega} = \frac{4\alpha}{\sigma(\kappa + 1)} (1 - \exp(-N\sigma)) \times \sum_n \theta_n \left( \frac{1}{\rho_1 + \theta_n} - \frac{1}{\rho_2 + \theta_n} \right) 2[1 - \cos(\rho_1 + \theta_n)] \quad (7.3)$$

where:

$$\rho_i = \frac{\omega l_1}{2c} (\gamma^{-2} + \xi_i^2), \quad \kappa = l_2/l_1, \quad \theta_n = \frac{2\pi n - (\rho_1 + \kappa\rho_2)}{1 + \kappa} > 0 \quad (7.4)$$

where  $\sigma$  is the absorption cross section per 1 foil and 1 gap,  $\kappa = l_2/l_1$ ,  $\xi_i = \omega_{Pi}/\omega$  where  $\omega_{Pi}$  is the plasma frequency of the foil(gap).

Adding the absorption in the mylar foil and in the gas volume, final spectrum of the absorbed TR is obtained (Fig.7.3).

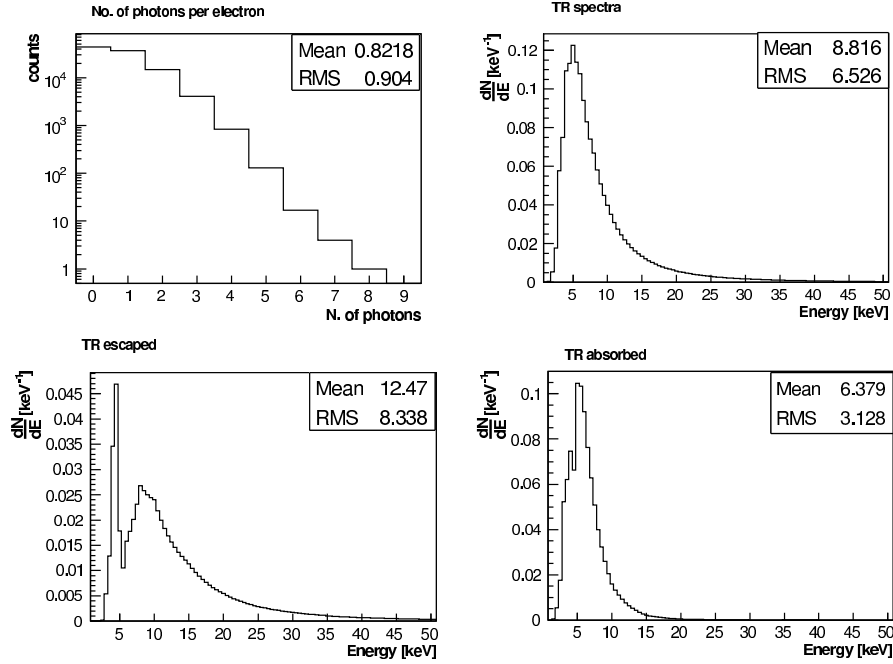


Figure 7.3: *Properties of the TR: Top left: Number of TR photons produced per electron per radiator; Top Right: spectrum of TR after the radiator; Bottom left: spectrum of TR not absorbed in the gas volume (escaped); Bottom right: TR spectrum absorbed in the gas. 90 foils per layer.*

Once the spectra for given set of parameters are produced - the mean number of photons  $\bar{N}$  produced in the radiator is computed by integrating the whole spectrum. On event by event basis the actual number of photons results from random sampling of a Poisson distribution with the mean value  $\bar{N}$ .

To study the performance of a setup that would simulate the one to be used in CBM (9 - 12 TRD layers) configurations up to 12 detector layers were computed.

For the evaluation of the electron pion separation the energy losses are the only source of information. Although it is possible to use the total energy deposit (for all layers), the more common method is based on likelihoods [77]. With this method the total energy loss spectra (from single detector layer) for electron and pions are taken as a probability distributions. After normalization these distribution represent a probability  $P_e(P_\pi)$  of an electron

(pion) to leave the energy  $E_n$  in the  $n$ th layer. All energies  $E_n$  of an event then give the probabilities that an electron (pion) produced these data:

$$\begin{aligned}
 P_e &= \prod_{i=1}^n P_e(E_i) \\
 P_\pi &= \prod_{i=1}^n P_\pi(E_i)
 \end{aligned}
 \tag{7.5}$$

The quantity  $P = P_e/(P_e + P_\pi)$  is then used for the particle identification. For a given electron efficiency (corresponds to a given threshold on  $P$ ) the pion contamination can be obtained.

For a TRD with a drift chamber read out (e.g ALICE TRD) another information used to improve the electron pion separation can be obtained from the drift time distributions of the clusters [78].

## 7.7 Results

The required performance of the CBM TRD is to reach a pion suppression of 100 what translates into pion efficiency of 1%. The optimization of the layout of a single chamber was made such that 9 or 12 layers of such a detector would reach a pion efficiency of around 0.1% or lower to keep a safety factor of 10 to account for the effects not included in this simulation.

The parameters of the simulation were the following (value in the brackets represents the default value):

- thickness of the gas volume (6 mm)
- thickness of the foil (15  $\mu m$ )
- thickness of the gap (200  $\mu m$ )
- total number of foils (150 or 90)
- fraction of the Xe in the Xe/CO<sub>2</sub> gas mixture (85/15)

Because two basic designs of the CBM TRD include 3 stations with 3 or 4 layers each - number of foils per layer (90 or 150) was chosen such that these two TRD configurations would result in approximately the same value of electron pion separation.

Fixed parameters in the simulation:

- material of the foil: polypropylene
- material of the gap: air
- thickness of the mylar window:  $25\mu\text{m}$
- temperature and the pressure of the gas: STP
- momentum of the simulated electron and pion:  $2\text{ GeV}/c$
- pion efficiency is computed for electron efficiency of 90

One simulated event was corresponding to one electron and one pion crossing the detector, both with momentum  $2\text{ GeV}/c$ . Schematic view of such an event can be seen in Fig. 7.4.

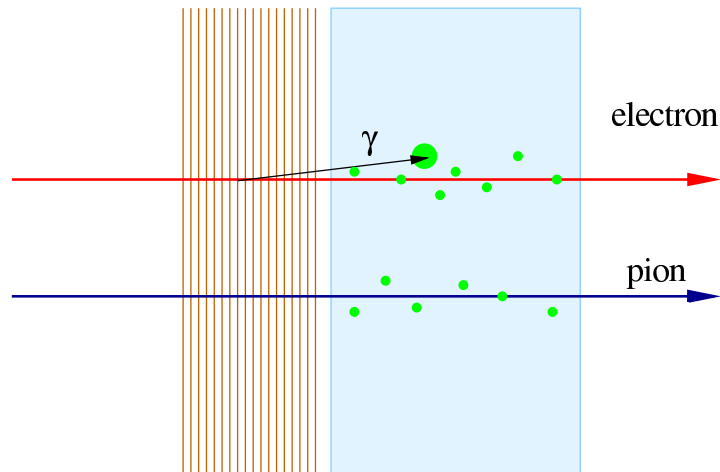


Figure 7.4: *Schematic illustration of one event. Both electron and pion deposit energy via ionization. If electron produced a photon in the radiator - it may be absorbed in the gas volume.*

Spectra of the energy deposit of electrons and pions of  $2\text{ GeV}/c$  in 6 mm Xe-CO<sub>2</sub> 85/15 mixture of can be seen in Fig. 7.5. The difference between the spectrum for electron  $dE/dx$  only and electron  $dE/dx$  plus TR shows as an "shoulder" in the second distribution. The difference between spectrum of the pions and  $dE/dx$  only electrons is the fact that at  $2\text{ GeV}/c$  the pions do not reach the relativistic plateau of the ionization energy losses.

Total energy deposit spectra with default settings are shown in Fig. 7.6. Likelihood distributions for the default settings and 12 layers are shown in Fig. 7.7.

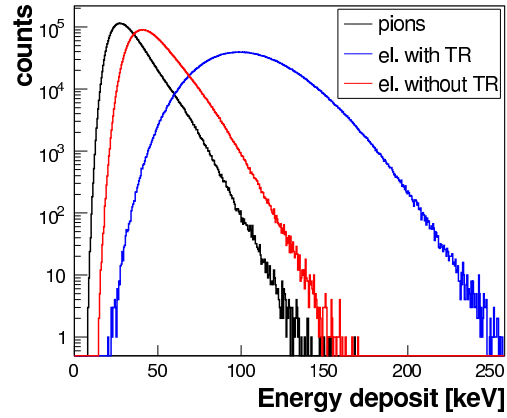
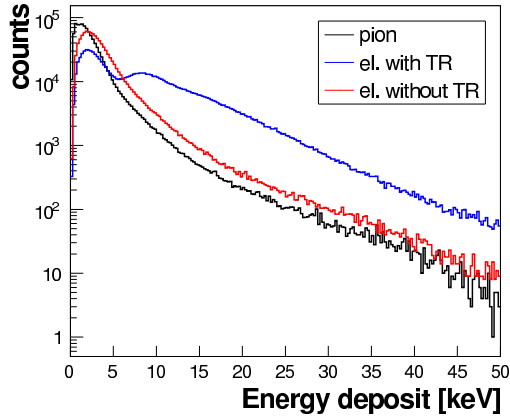


Figure 7.5: Spectra of energy deposit of  $2\text{ GeV}/c$  pions, electrons and electrons without TR in 6 mm of Xe- $\text{CO}_2$  (default configuration) 85/15

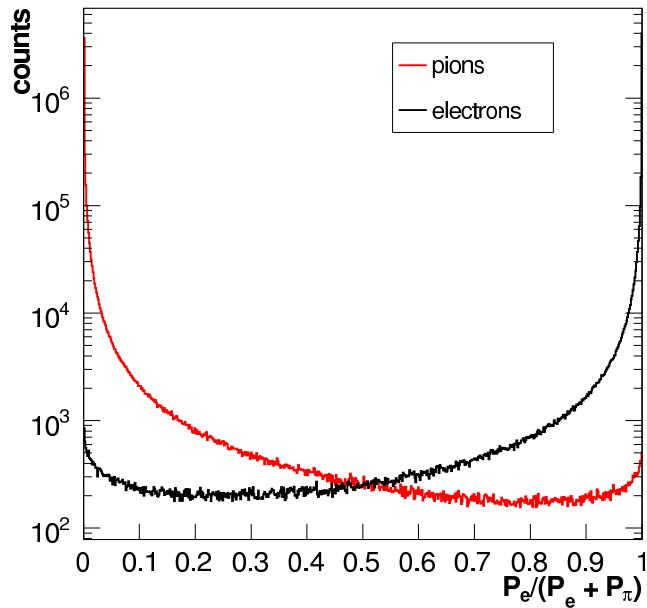


Figure 7.7: Electron pion separation likelihood for 12 layers and default parameters settings.



As mentioned before, both integrated spectra of energy deposition and likelihood can be used for particle identification. To obtain the pion efficiency with any of the two one integrates both pion and electron spectra from the right side until required electron efficiency (90% in our case) is reached. The pion efficiency is then estimated as the fraction of the integrated pion spectrum.

Comparison of these two methods can be seen in Fig. 7.8. The difference for 12 layers is  $\sim$  factor 10. Contrary to the common experience the truncation of the energy deposit spectra does not bring any improvement in terms of pion suppression. This can be explained by the fact that on average only 0.5 TR photon is absorbed per one layer and applying the truncation of around 60% would suppress predominantly entries from those layers in which a TR photo was absorbed.

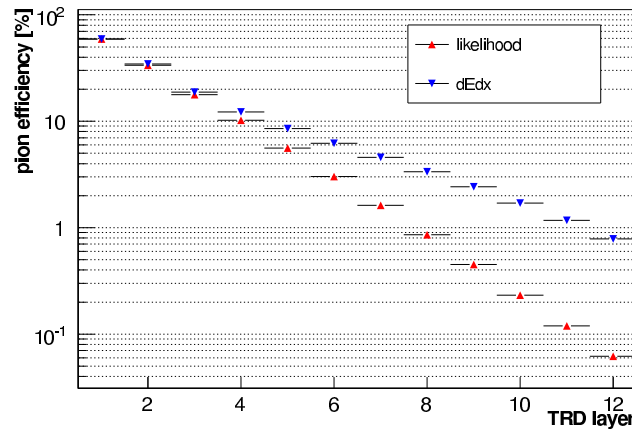


Figure 7.8: Comparison of pion efficiency for likelihood method and method based on integrated energy losses as a function of number of layers.

In Fig. 7.9 the pion efficiency as a function of number of layers for different radiator thicknesses (number of foils) is presented. The required pion efficiency of 0.1% (including the above mentioned safety factor) can be reached either with 150 foils with 9 layers or 90 foils with 12 layers. Different detector configurations are equivalent in this respect. The 12 layer version with lighter (thinner) radiator would be preferred by tracking. On the other hand 9 layer configuration would mean less material in total and also lower cost.

Fig. 7.10 shows the dependence of the pion efficiency for different detector thicknesses. Strong dependence on this variable reflects the fraction of the TR is absorbed inside the gas. This dependence can be seen in Fig. 7.11.

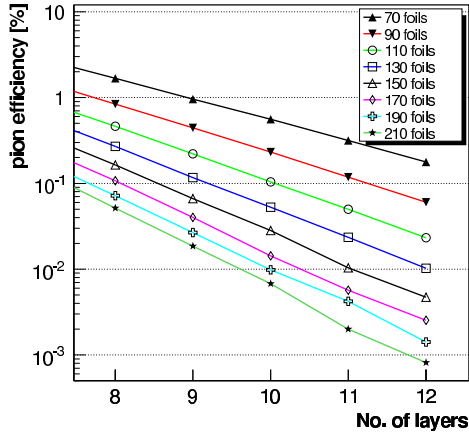


Figure 7.9: *Pion efficiency as a function of number of layers for different radiator thicknesses.*

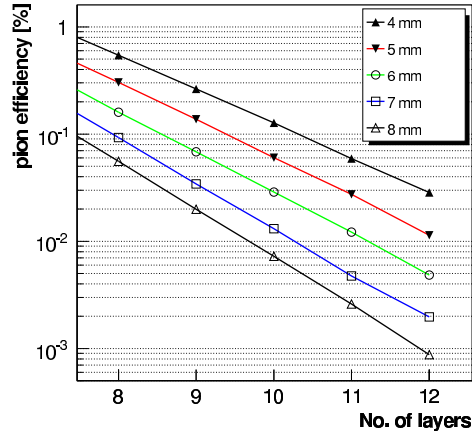


Figure 7.10: *Pion efficiency as a function of number of layers for different detector (gas) thicknesses. 150 foils per layer were considered.*

At the same time the average energy of the absorbed photons is increasing (Fig. 7.12).

The TR yield and spectrum depends strongly on the thickness of the foil and the spacing between the foils. Optimizing these two parameters in order to achieve the best possible performance of the detector is therefore essential.

The dependence of the number of TR photons (produced and absorbed) and their mean energy on the thickness of the foil is shown in Fig. 7.13 and 7.14 respectively. It is interesting to stress that while the total number of photons produced is increasing over the whole range, the total number of the photons absorbed in the detector shows a maximum at around  $15 \mu\text{m}$ . The reason is the step increase in the mean energy of the photons (Fig. 7.14). Because the detector is only 6 mm thick, the probability of TR photons to be absorbed decreases rather strongly as their energy increases. Pion efficiency as a function of the foil thickness is shown in Fig. 7.15. Optimal value of the thickness of the foil for this configuration is about  $15 - 17 \mu\text{m}$ .

The dependence of the number of TR photons (produced and absorbed) and their mean energy on the width of the gap between the foils is shown in Fig. 7.16 and 7.17 respectively. While the mean energy of the photons remains nearly constant, the total number of produced and absorbed photons shows strong increase. As a consequence the pion efficiency experiences a step decrease with the increasing width of the gap. In Fig. 7.18 can be

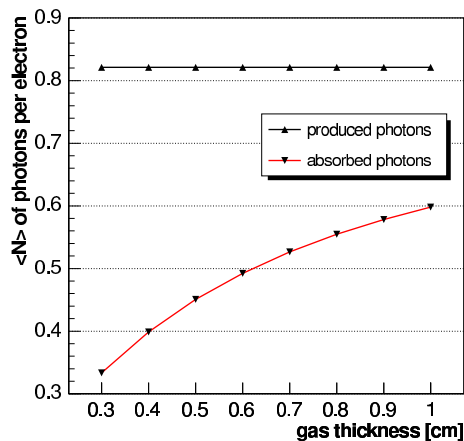


Figure 7.11: *Dependence of the average number of TR photons absorbed in the detector (per layer) on the gas thickness. For comparison also the total number of TR photons produced is shown. 90 foils per layer were considered.*

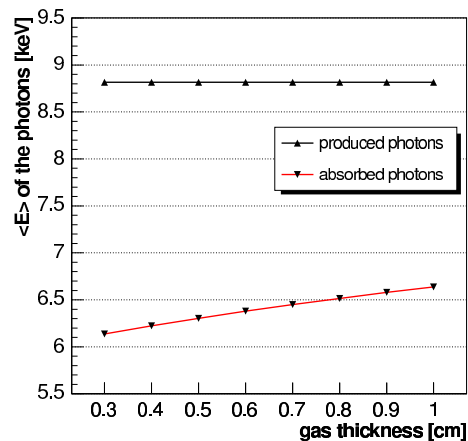


Figure 7.12: *Dependence of the average energy of TR photons absorbed in the detector (per layer) on the gas thickness. For comparison also the average energy of TR photons produced is shown. 90 foils per layer were considered.*

seen that about a factor 6 could be gained if the gap width is increased from 200 to 500  $\mu\text{m}$ . This effect is known as the formation zone effect [79]. This is indeed a very interesting possibility because the material budget per layer would remain unchanged.

Last parameter of the simulation was the composition of the gas. The default value of the  $\text{CO}_2$  content of 15% was based on commonly used relative content of  $\text{CO}_2$  in gas mixtures. This ratio of Xe -  $\text{CO}_2$  was also used in the first test measurements [80]. The  $\text{CO}_2$  content is responsible for the detector stability. It has rather small absorption cross section for TR because of its rather low atomic numbers. The influence of the relative contents of Xe and  $\text{CO}_2$  is shown in Fig. 7.19. It can be seen that going from 15% of  $\text{CO}_2$  content to only 5% can bring an improvement of about 30% in pion rejection. Whether the detector could be operated with such a low  $\text{CO}_2$  content has to be tested.

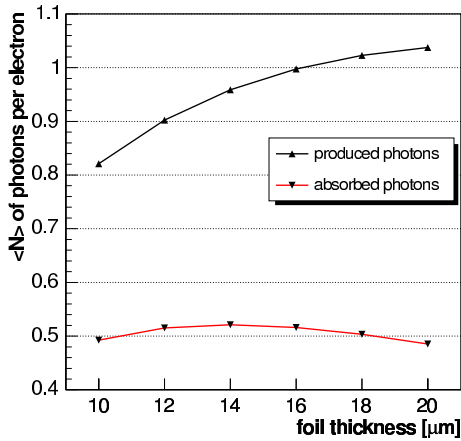


Figure 7.13: Number of produced and absorbed TR photons as a function of the thickness of the foil. 150 foils per layer were considered.

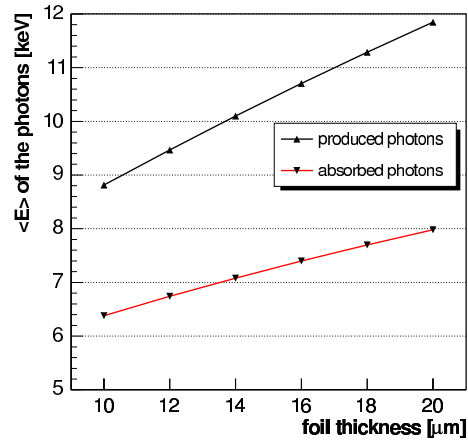


Figure 7.14: Mean energy of produced and absorbed TR photons as a function of the thickness of the foil. 150 foil per layer were considered.

## 7.8 Simulations versus Data

First measurements of  $dE/dx$  spectra for electrons and pions with a prototype chamber including the radiator were performed in 2006 in GSI [80] at a beam energy of 1.5 GeV/c.

The 6 mm thick read out gas chamber was filled with 85/15 - Xe/CO<sub>2</sub>. The radiator was composed of 200 foils each 15  $\mu\text{m}$  thick with 500  $\mu\text{m}$  spacing. The resulting energy deposit spectra compared to simulation are shown in Fig. 7.20. While the pion energy deposition is described rather well, the simulation overestimated the energy deposition of the electrons above 20 keV. Also - the local minimum at around 5 keV is not seen in the data. The reason for this discrepancy is not yet fully understood. Previous measurements of ionization energy deposits [74] and TR absorption [71] were in good agreement with simulations.

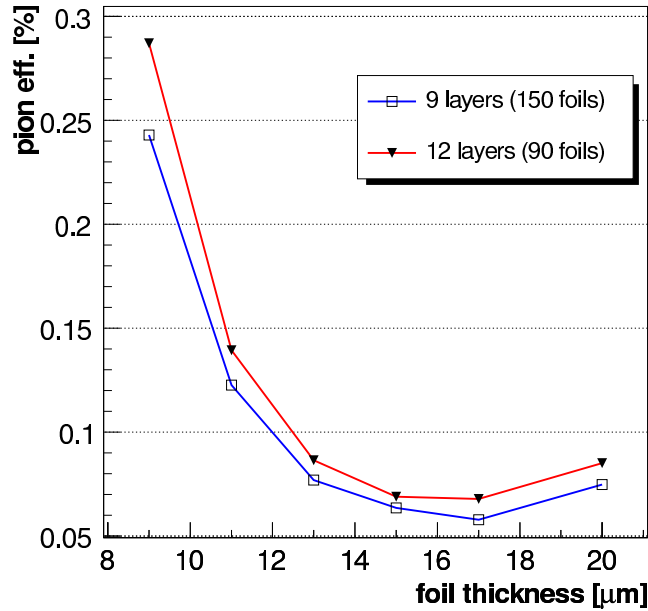


Figure 7.15: Pion efficiency as a function of the thickness of the foil for both 9 and 12 layers TRD designs with 150 and 90 foils per layer.

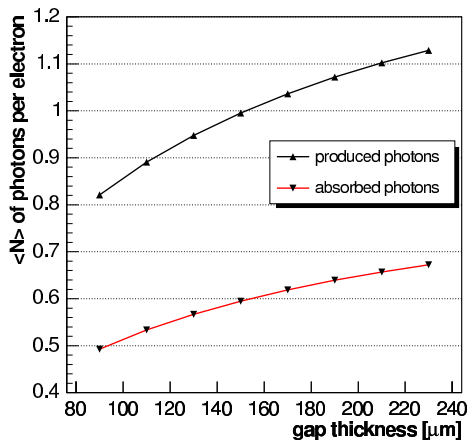


Figure 7.16: Number of produced and absorbed TR photons as a function of the thickness of the gap. 150 foil per layer were considered.

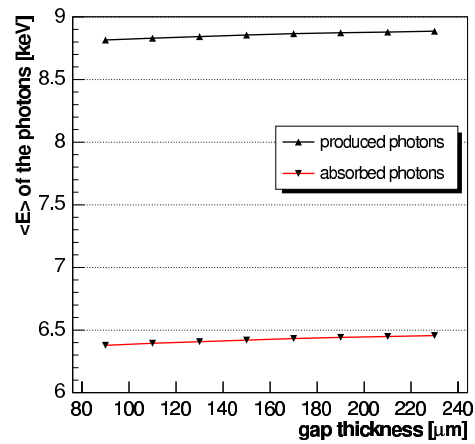


Figure 7.17: Mean energy produced and absorbed TR photons as a function of the thickness of the gap. 150 foil per layer were considered.

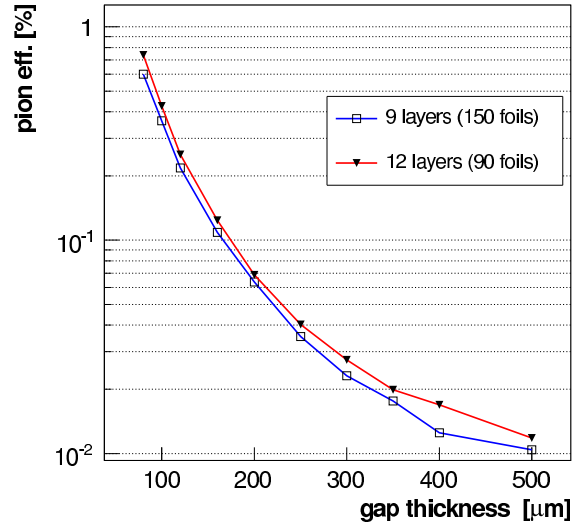


Figure 7.18: Pion efficiency as a function of the thickness of the gap for both 9 and 12 layers TRD designs with 150 and 90 foils per layer.

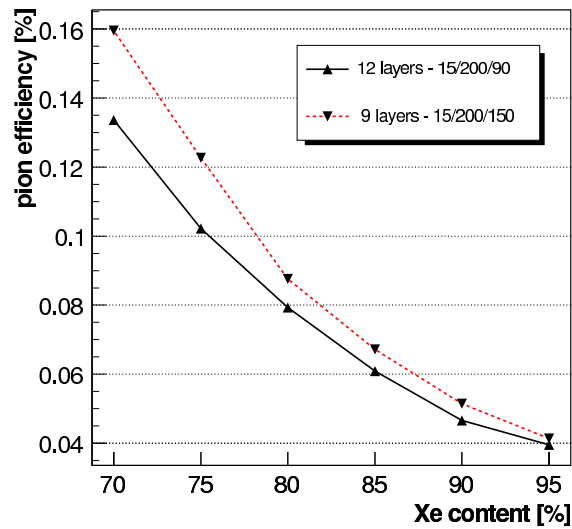


Figure 7.19: Pion efficiency as a function of relative Xe content in the gas for both 9 and 12 layers TRD designs with 150 and 90 foils per layer.

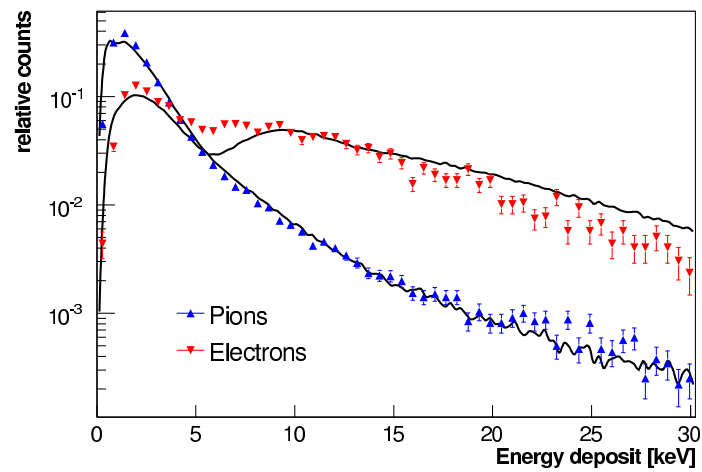


Figure 7.20: Comparison of measured (points) and simulated (lines) energy losses of 1.5 GeV/c electrons and pions in 6mm gas detector filled with 85/15 - Xe/CO<sub>2</sub>. The radiator was composed of 200 foils with thickness of 20 $\mu$ m with 500 $\mu$ m spacing. The data points are taken from [80]

## 7.9 Discussion

In this chapter a performance of a fast transition radiation detector in terms of electron - pion separation was studied. It was shown that with both designs foreseen the CBM TRD ( 9 or 12 detector layers) the required pion efficiency of 100 or better can be obtained.

The pion efficiency is very sensitive to the parameters of the radiator; the thickness of the foil and the distance between the foils. While the first experiences minimum of pion efficiency at around  $17 \mu m$ , the latter shows monotonous decrease. Whether is possible to construct mechanically stable large area radiators with foil spacing of  $500 \mu m$  or more has to be proven.

Further detailed simulations and precision measurements are needed for detector design and optimization. The main topics include the tracking abilities of the full CBM TRD within the CBM detector setup and electron-pion separation in high particle density environment. The first is currently being studied with the CBM ROOT framework. The latter one should be answered within next test beam measurement.

The TR part of this simulation code used for the present study was implemented inside the CBM ROOT framework where it is being further developed.



# Chapter 8

## Appendix - A -

Invariant mass spectra for  $K^+$  for 8 rapidity bins. Scaled mixed event background together with scaled OMC are shown to allow for comparison. The up to 16 histograms represent 16  $p_T$  bins with 0.1 GeV/c bin size for  $p_T \in (0, 1)$  GeV/c and 0.2 GeV/c bins for  $p_T \in (1, 2)$  GeV/c

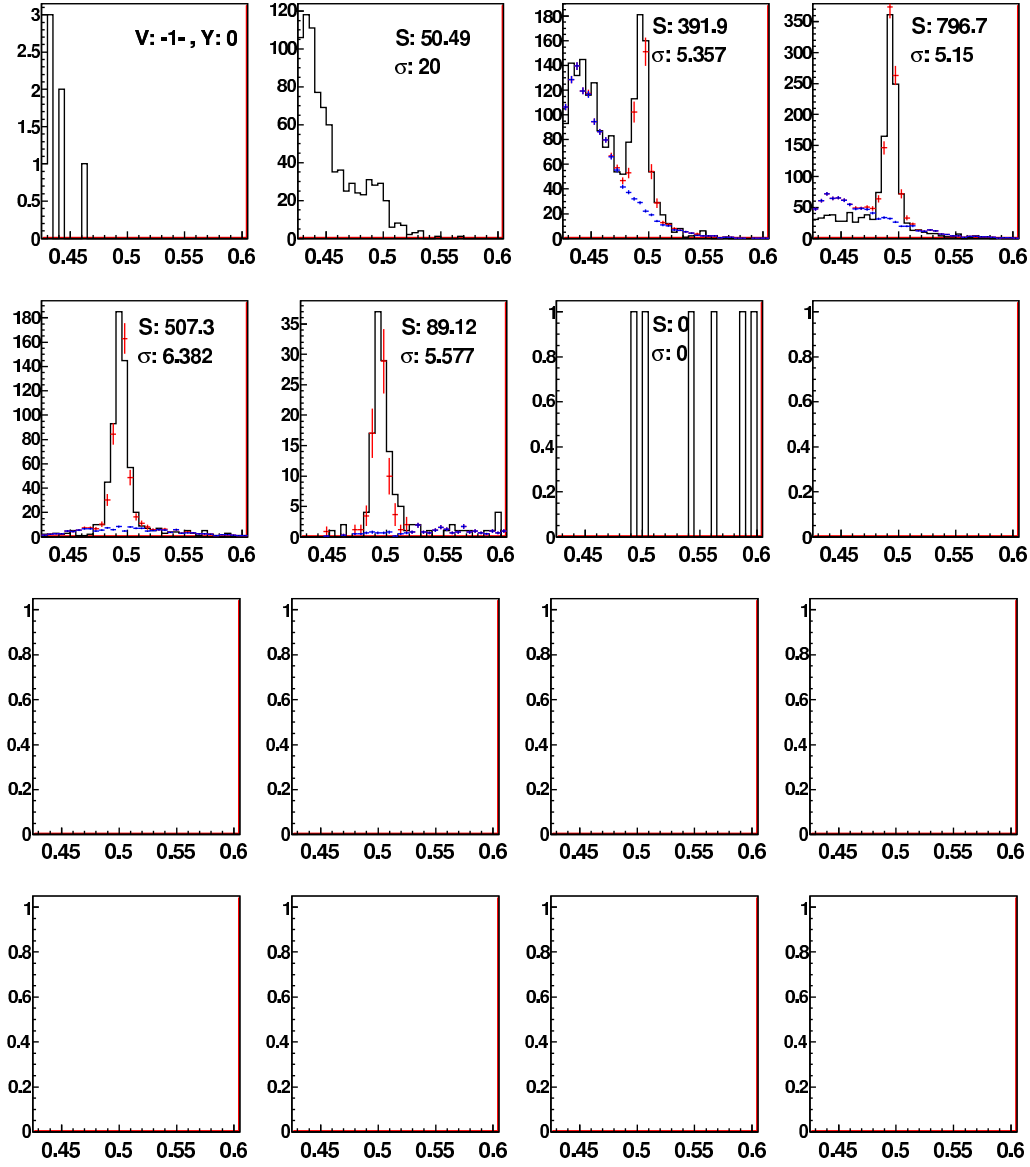


Figure 8.1:  $K^+$  Invariant mass distributions for different  $p_T$  bins for the rapidity bin  $[0]$ . Black line shows the data distribution, the blue points show scaled mixed event background, the red points show the scaled OMC on top of the mixed event background. Quoted are the integral and  $\sigma$  of the peak.

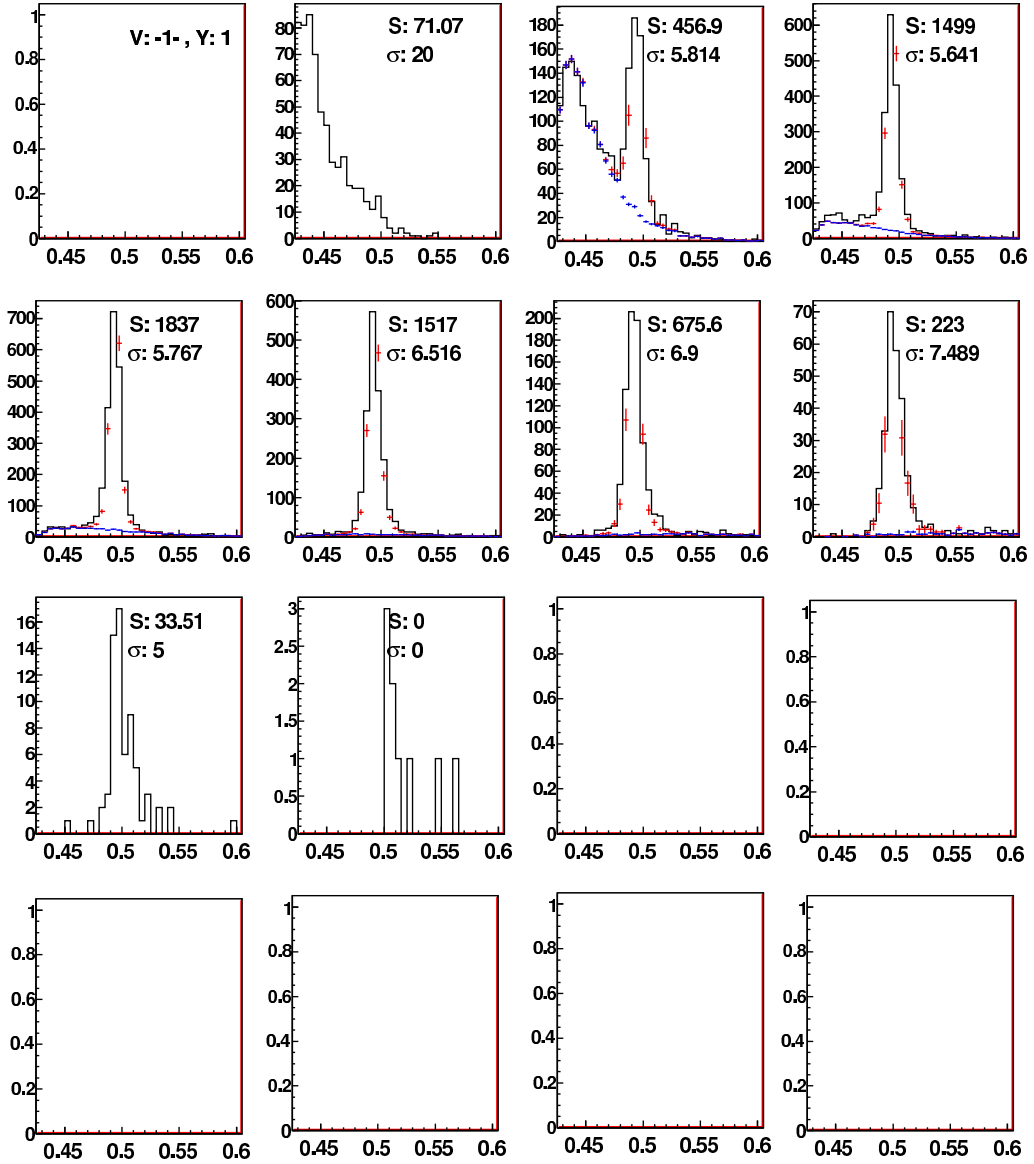


Figure 8.2:  $K^+$  Invariant mass distributions for different  $p_T$  bins for the rapidity bin [1]. Black line shows the data distribution, the blue points show scaled mixed event background, the red points show the scaled OMC on top of the mixed event background. Quoted are the integral and  $\sigma$  of the peak.

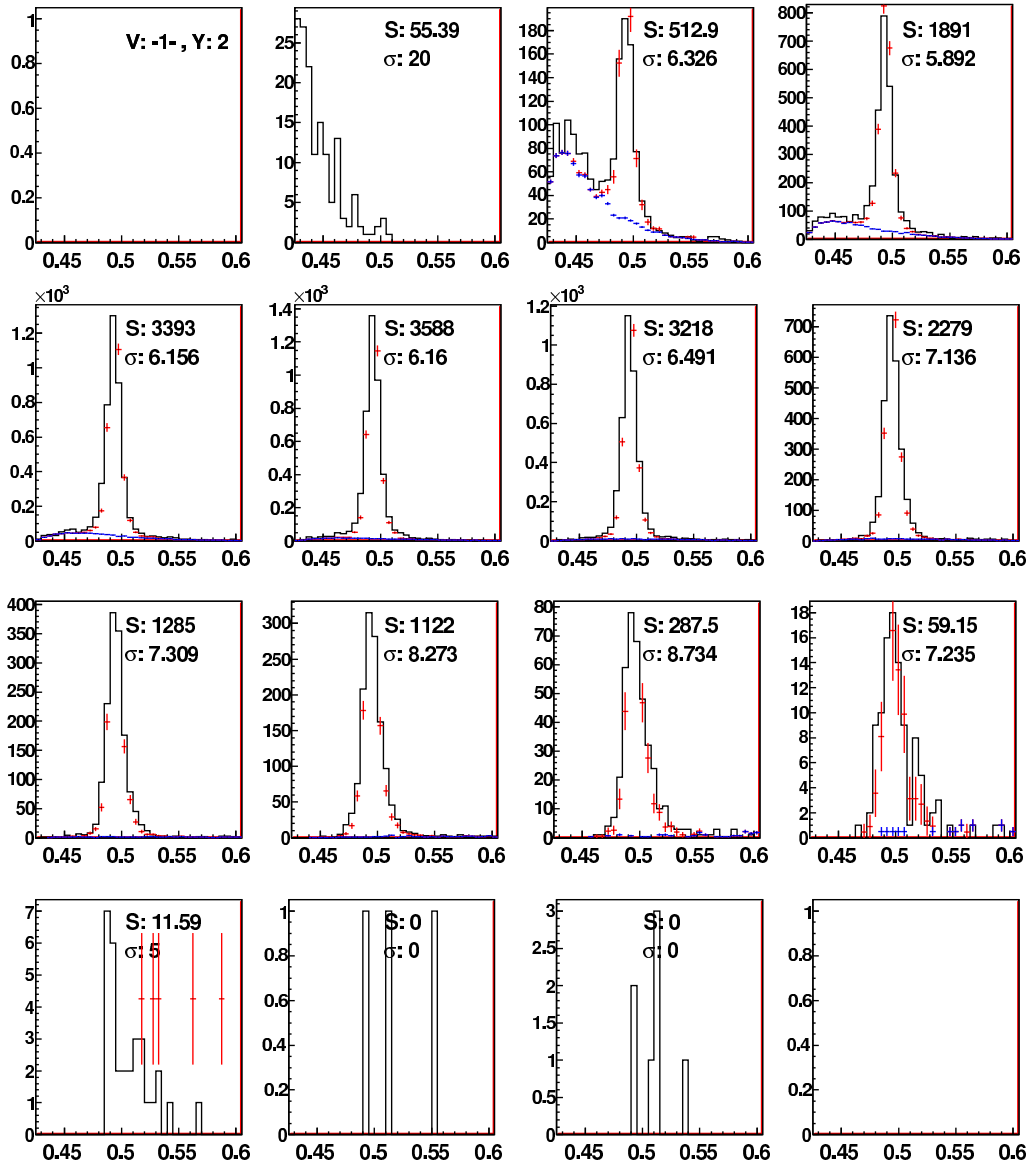


Figure 8.3:  $K^+$  Invariant mass distributions for different  $p_T$  bins for the rapidity bin [2]. Black line shows the data distribution, the blue points show the scaled mixed event background, the red points show the scaled OMC on top of the mixed event background. Quoted are the integral and  $\sigma$  of the peak.

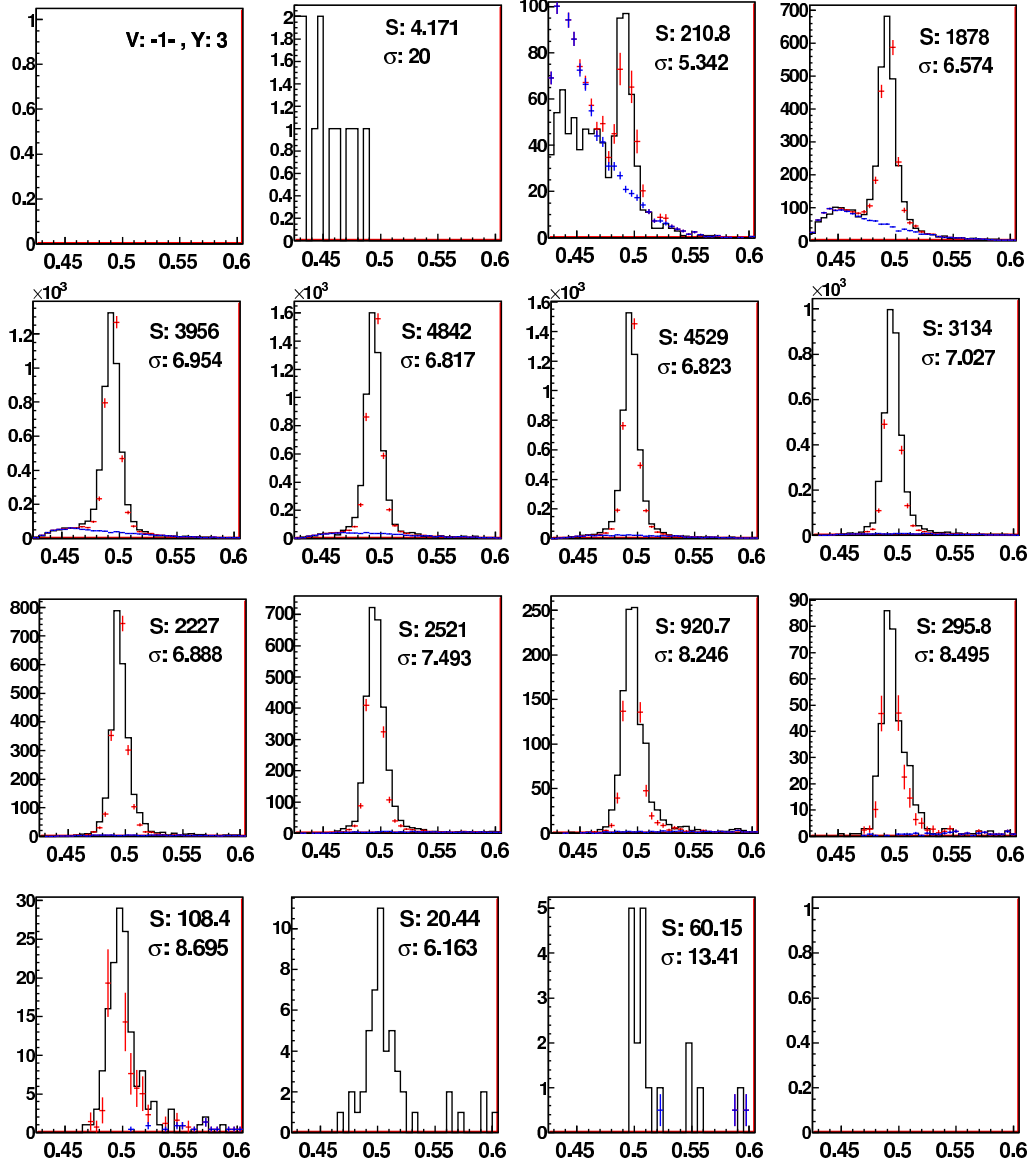


Figure 8.4:  $K^+$  Invariant mass distributions for different  $p_T$  bins for the rapidity bin [3]. Black line shows the data distribution, the blue points show scaled mixed event background, the red points show the scaled OMC on top of the mixed event background. Quoted are the integral and  $\sigma$  of the peak.

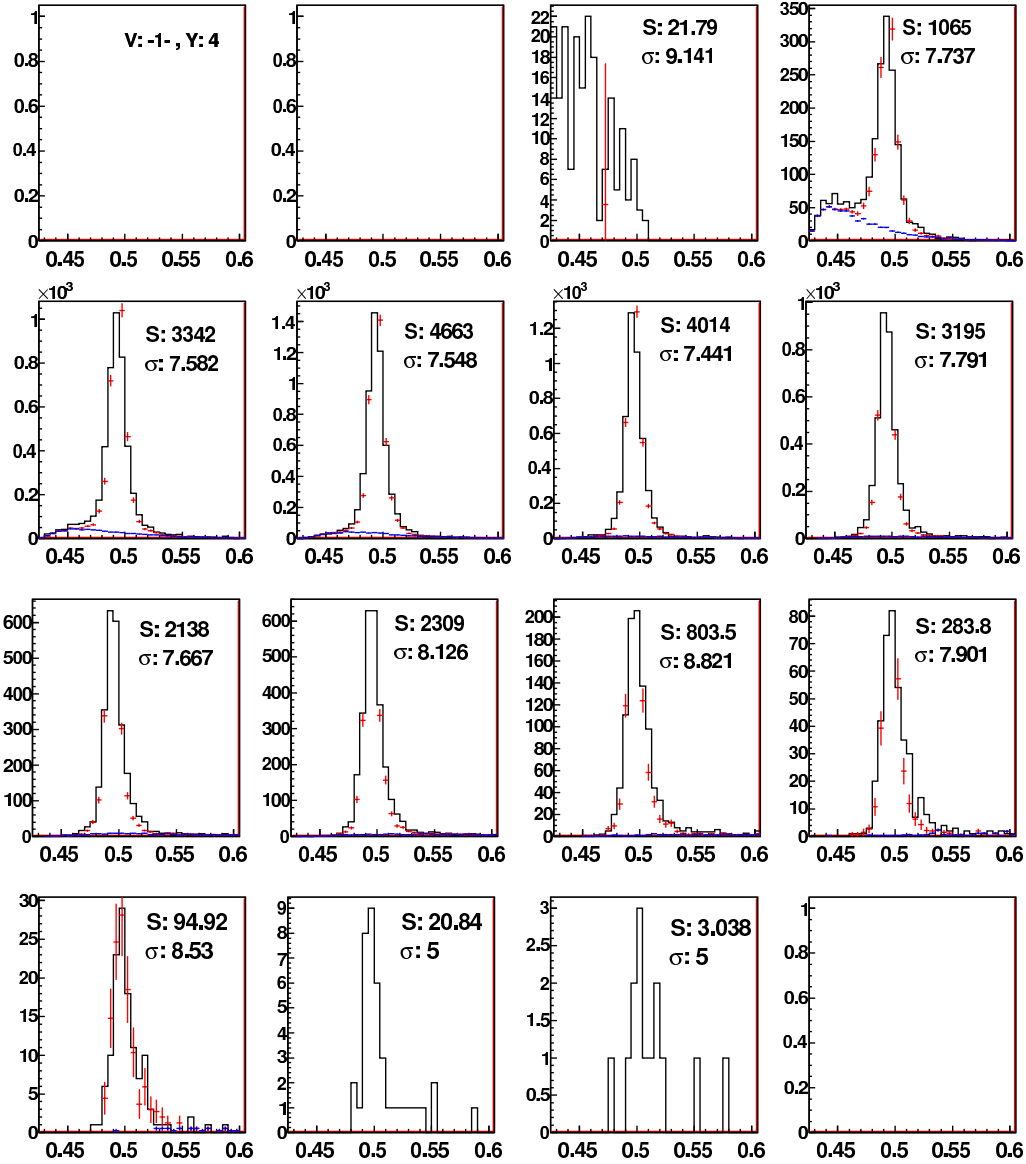


Figure 8.5:  $K^+$  Invariant mass distributions for different  $p_T$  bins for the rapidity bin [4]. Black line shows the data distribution, the blue points show scaled mixed event background, the red points show the scaled OMC on top of the mixed event background. Quoted are the integral and  $\sigma$  of the peak.

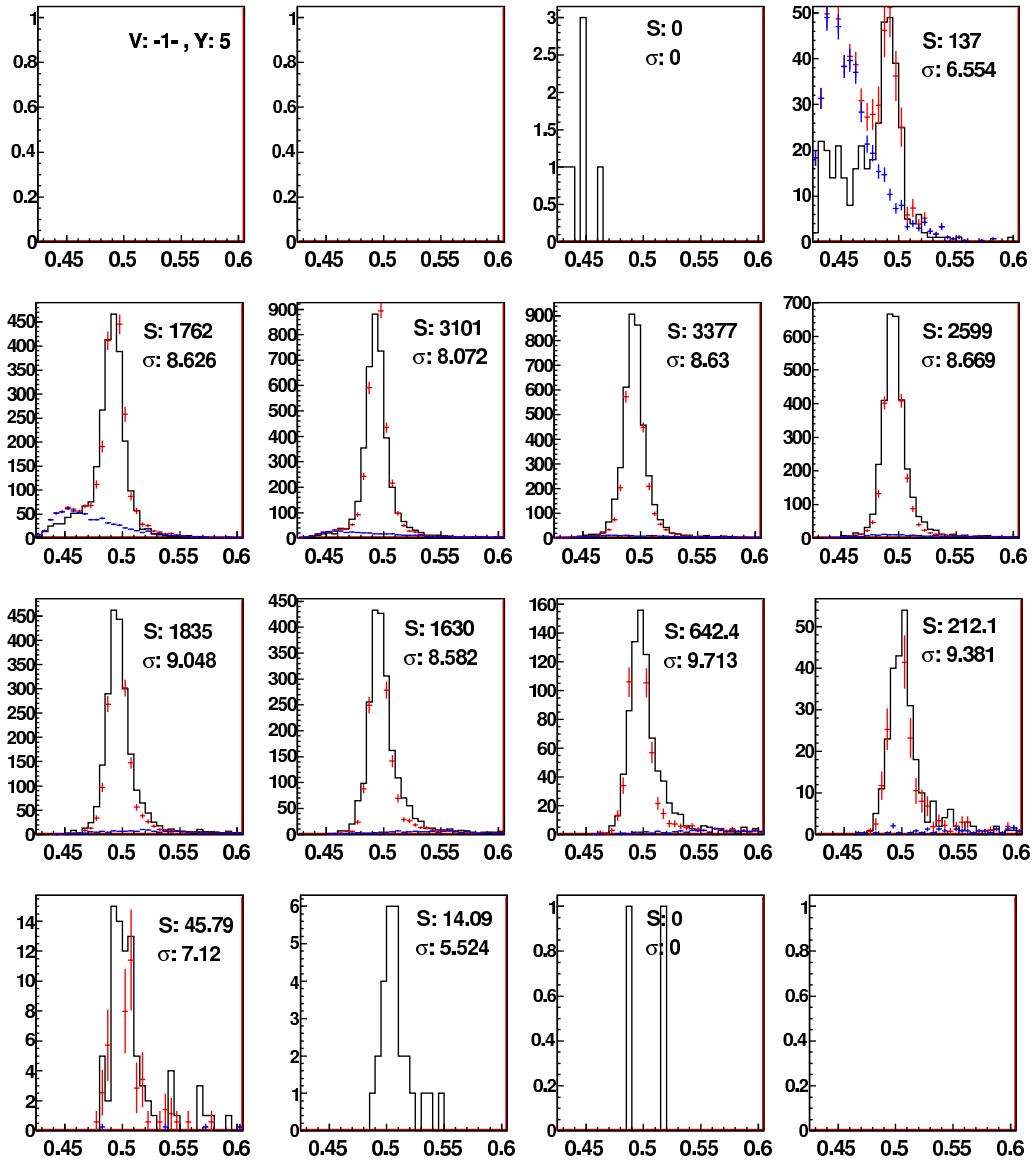


Figure 8.6:  $K^+$  Invariant mass distributions for different  $p_T$  bins for the rapidity bin [5]. Black line shows the data distribution, the blue points show scaled mixed event background, the red points show the scaled OMC on top of the mixed event background. Quoted are the integral and  $\sigma$  of the peak.

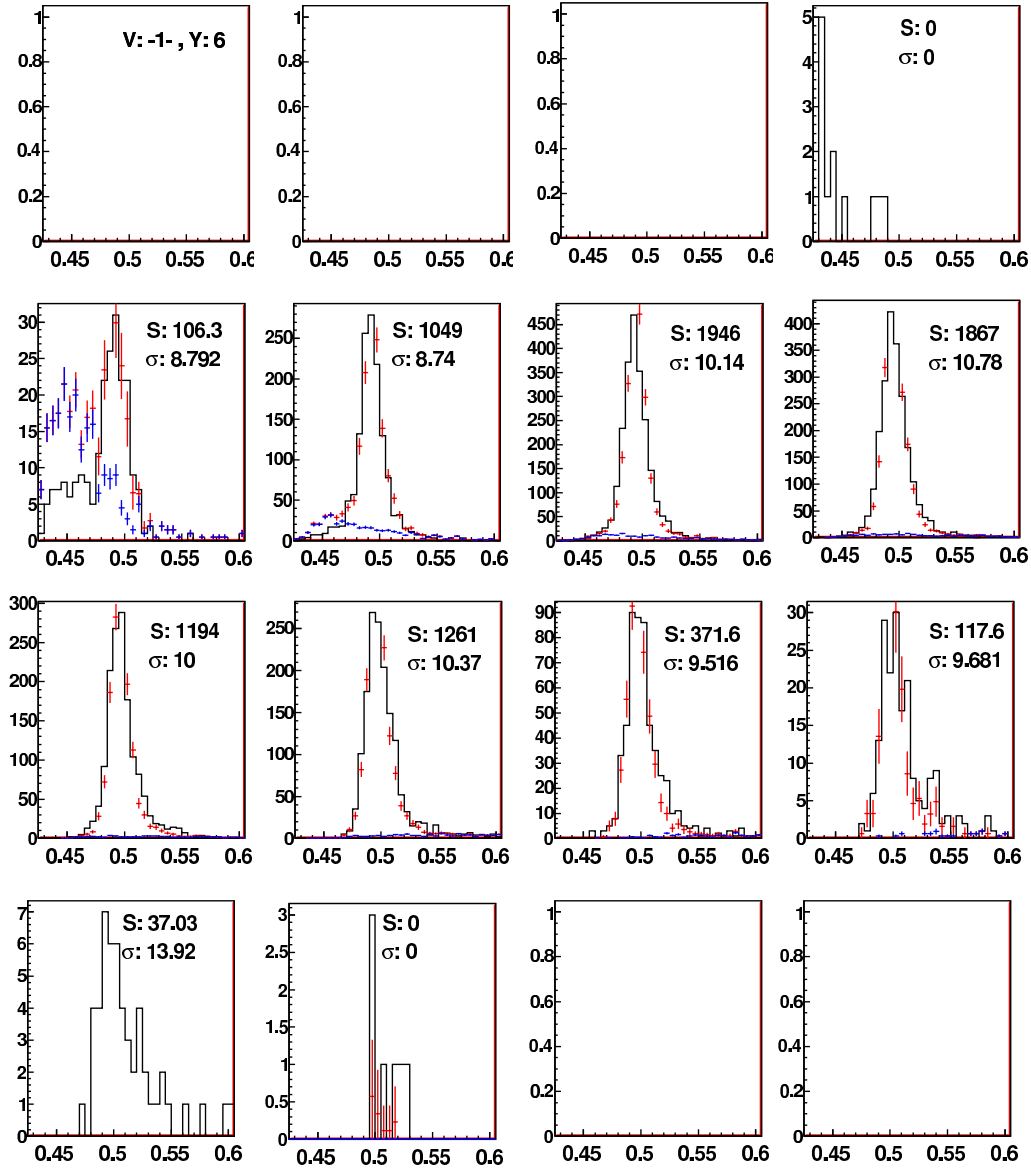


Figure 8.7:  $K^+$  Invariant mass distributions for different  $p_T$  bins for the rapidity bin [6]. Black line shows the data distribution, the blue points show the scaled mixed event background, the red points show the scaled OMC on top of the mixed event background. Quoted are the integral and  $\sigma$  of the peak.



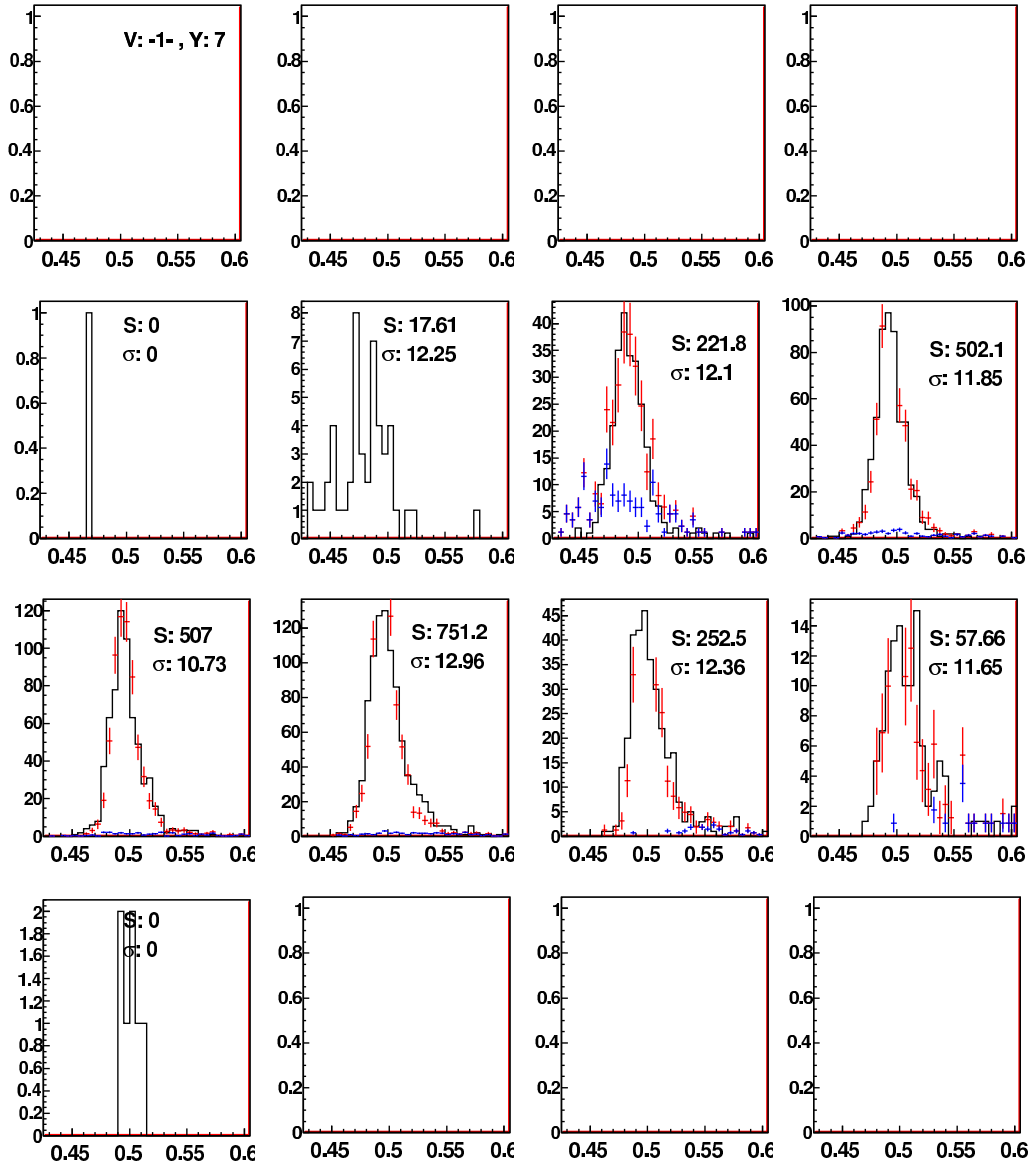


Figure 8.8:  $K^+$  Invariant mass distributions for different  $p_T$  bins for the rapidity bin  $[-1, 1]$ . Black line shows the data distribution, the blue points show scaled mixed event background, the red points show the scaled OMC on top of the mixed event background. Quoted are the integral and  $\sigma$  of the peak.



# Chapter 9

## Appendix - B -

Blast wave fits of the  $K^+$   $p_T$  spectra for 8 different values of the fixed  $\beta_S$  parameter. (Fig. 9.1 - 9.4).

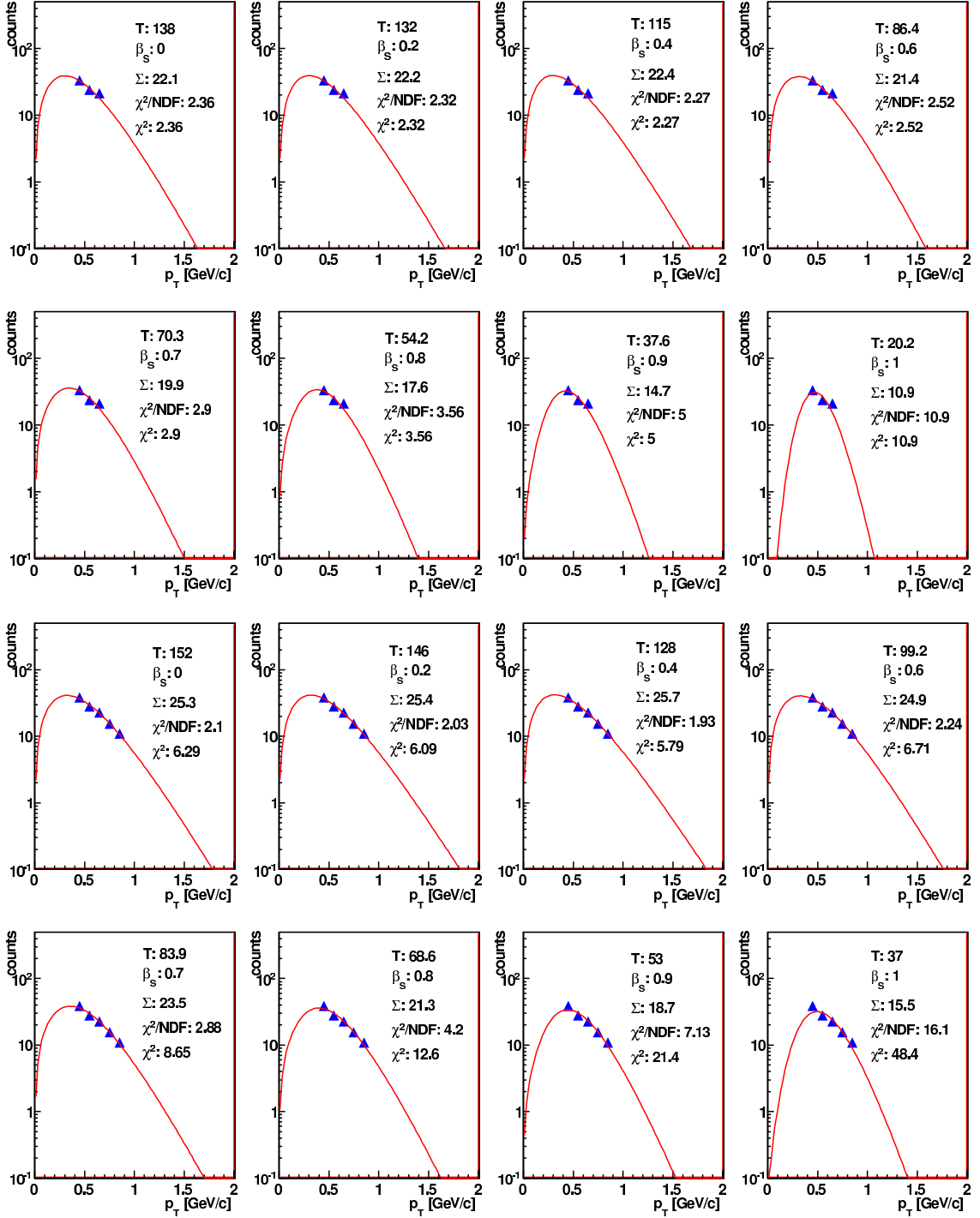


Figure 9.1: Blast wave fits of the  $K^+$   $p_T$  spectra for the rapidity bins 0 (upper part) and 1 (lower part) for 8 different fixed values of  $\beta_S$  parameter. Quoted values are: temperature,  $\beta_S$ , integral,  $\chi^2$  per degree of freedom and total  $\chi^2$ .

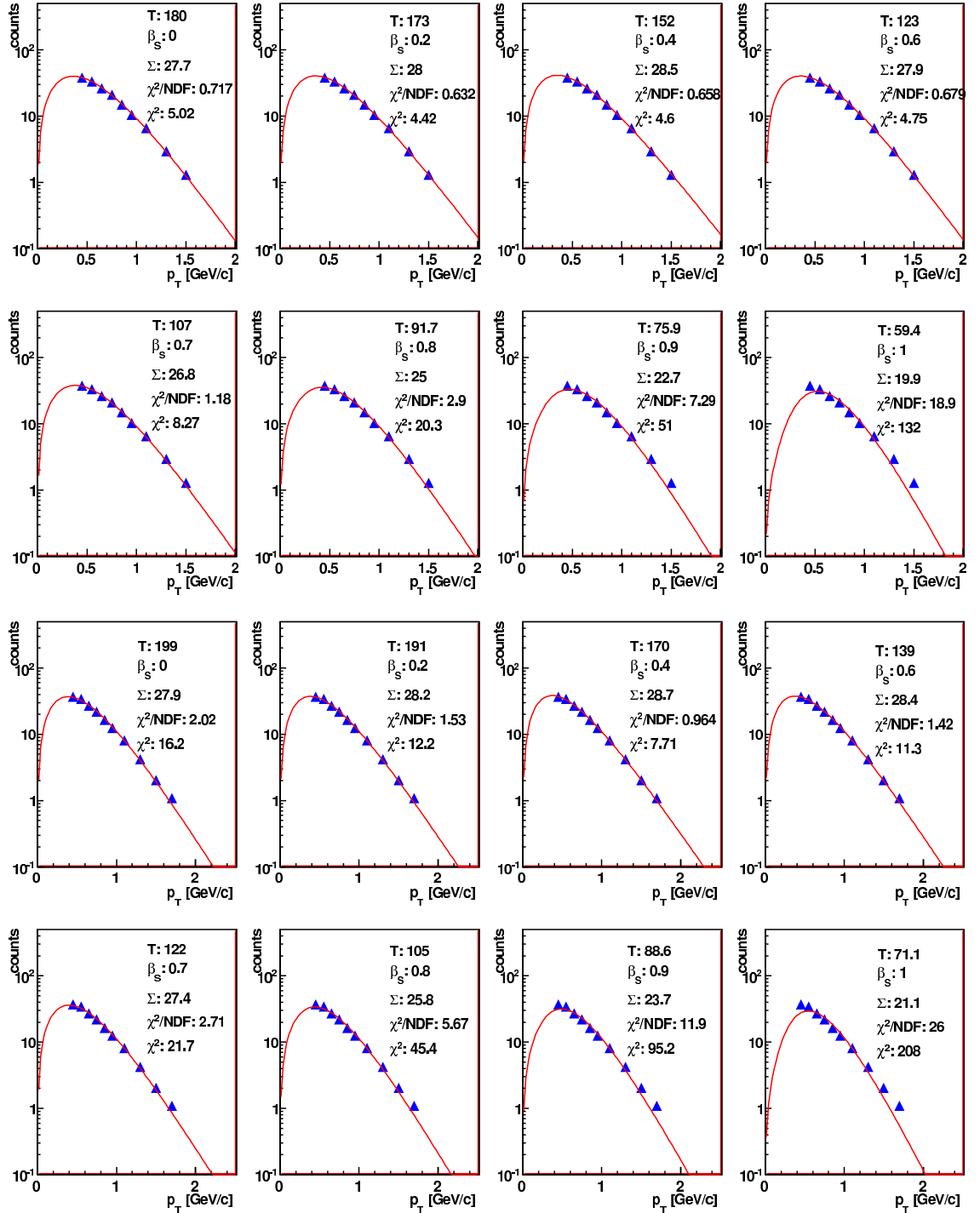


Figure 9.2: Blast wave fits of the  $K^+$   $p_T$  spectra for the rapidity bins 2 (upper part) and 3 (lower part) for 8 different fixed values of  $\beta_S$  parameter. Quoted values are: temperature,  $\beta_S$ , integral,  $\chi^2$  per degree of freedom and total  $\chi^2$ .

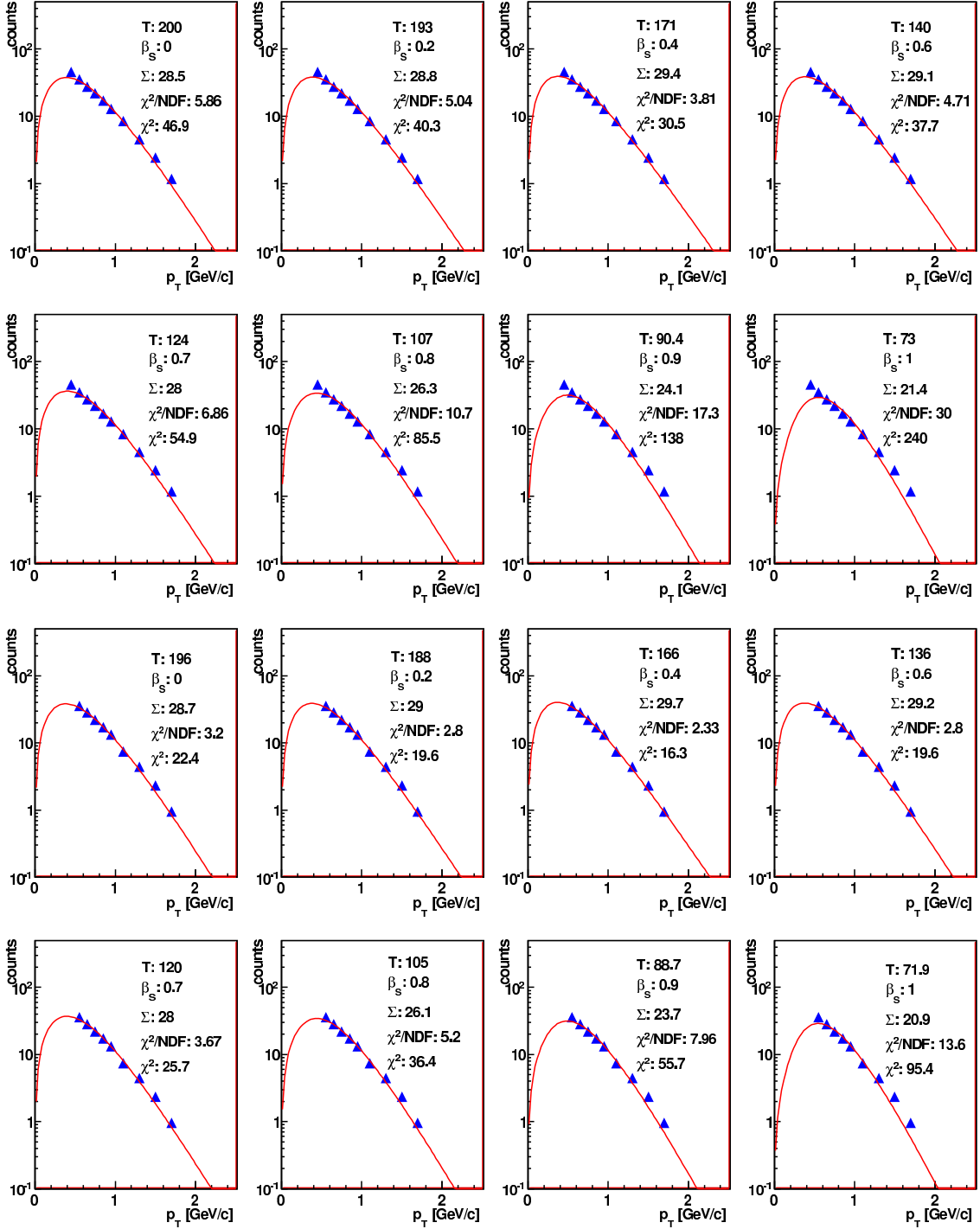


Figure 9.3: Blast wave fits of the  $K^+$   $p_T$  spectra for the rapidity bins 4 (upper part) and 5 (lower part) for 8 different fixed values of  $\beta_S$  parameter. Quoted values are: temperature,  $\beta_S$ , integral,  $\chi^2$  per degree of freedom and total  $\chi^2$ .

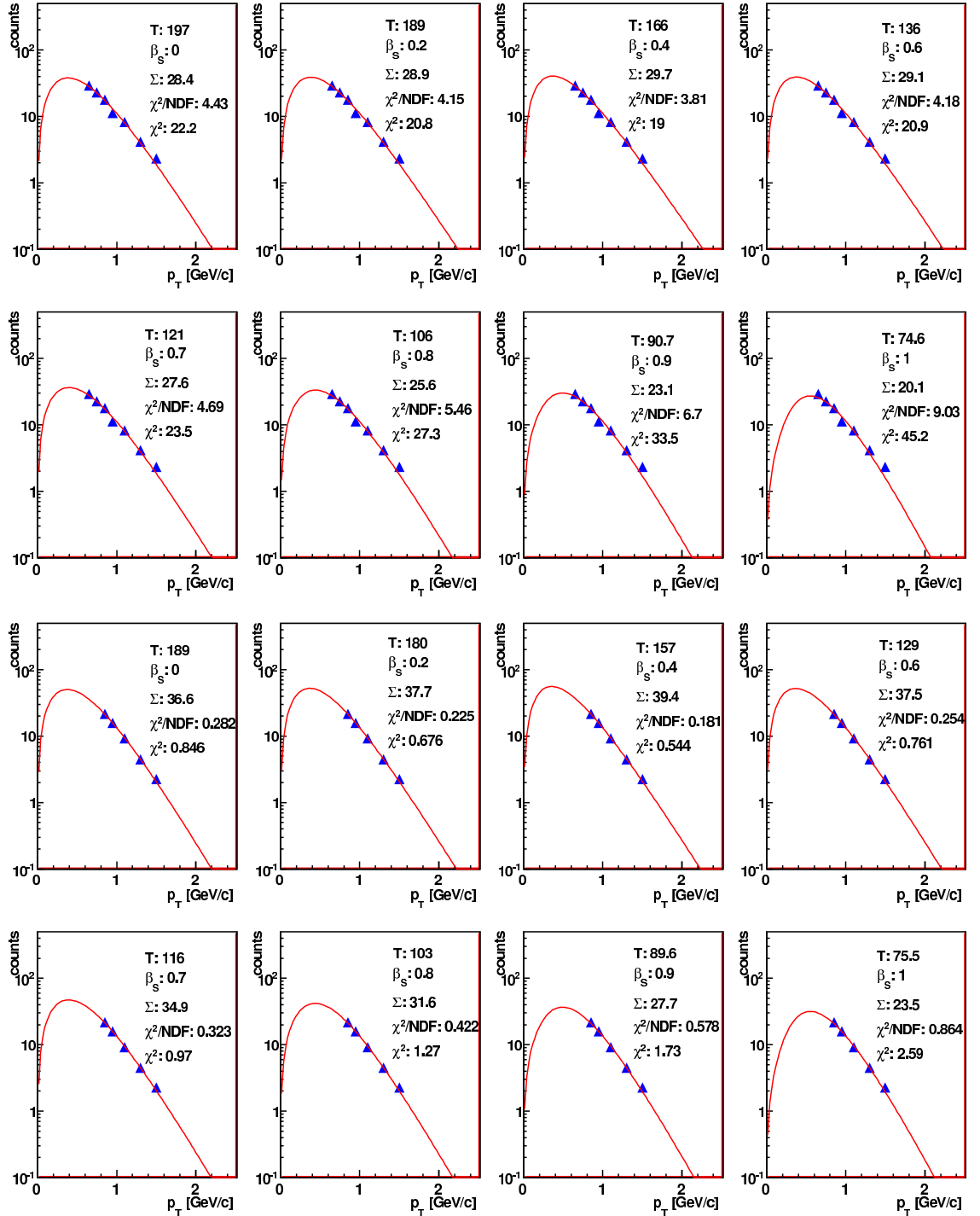


Figure 9.4: Blast wave fits of the  $K^+$   $p_T$  spectra for the rapidity bins 6 (upper part) and 7 (lower part) for 8 different fixed values of  $\beta_S$  parameter. Quoted values are: temperature,  $\beta_S$ , integral,  $\chi^2$  per degree of freedom and total  $\chi^2$ .





# Bibliography

- [1] H. Satz: Limits of confinement: The first 15 years of ultra- relativistic heavy ion studies. *Nucl. Phys.*, A715:3–19, (2003).
- [2] J. Collins and M. Perry: Superdense matter: neutrons or asymptotically free quarks ? *Phys. Rev. Lett.*, 34:1353, (1979).
- [3] U. W. Heinz and M. Jacob: Evidence for a new state of matter: An assessment of the results from the CERN lead beam programme. (2000).
- [4] F. Karsch and E. Laermann: Thermodynamics and in-medium hadron properties from lattice QCD. (2003).
- [5] A. Andronic and P. Braun-Munzinger: Ultrarelativistic nucleus nucleus collisions and the quark- gluon plasma. *Lect. Notes Phys.*, 652:35–68, (2004).
- [6] U. W. Heinz: Thermalization at RHIC. *AIP Conf. Proc.*, 739:163–180, (2005).
- [7] G. Odyniec: Signs of thermalization from RHIC experiments. *Eur. Phys. J.*, A29:1–5, (2006).
- [8] G. D. Westfall: Nuclear Fireball Model for Proton Inclusive Spectra from Relativistic Heavy-Ion Collisions. *Phys. Rev. Lett.*, 37:1202–1205, (1976).
- [9] J. D. Bjorken: Highly relativistic nucleus-nucleus collisions: The central rapidity region. *Phys. Rev. D*, 27:140–151, (1983).
- [10] K. Kajantie and L. D. McLerran: Probes of the Quark Gluon Plasma in High-Energy Collisions. *Ann. Rev. Nucl. Part. Sci.*, 37:293–323, (1987).
- [11] J. W. Harris and B. Muller: The search for the quark-gluon plasma. *Ann. Rev. Nucl. Part. Sci.*, 46:71–107, (1996).

- 
- [12] S. A. Bass et al.: Signatures of quark-gluon-plasma formation in high energy heavy-ion collisions: A critical review. *J. Phys.*, G25:R1–R57, (1999).
- [13] T. Peitzmann and M. H. Thoma: Direct photons from relativistic heavy-ion collisions. *Phys. Rept.*, 364:175–246, (2002).
- [14] R. Rapp and J. Wambach: Chiral symmetry restoration and dileptons in relativistic heavy-ion collisions. *Adv. Nucl. Phys.*, 25:1, (2000).
- [15] J. Rafelski and J. Letessier: Strangeness and quark gluon plasma. *J. Phys.*, G30:S1–S28, (2004).
- [16] R. Stock: The strangeness signal in hadron production at relativistic energy. *hep-ph/0312039*, (2003).
- [17] H. Satz: Colour deconfinement in nuclear collisions. *Rept. Prog. Phys.*, 63:1511, (2000).
- [18] S. S. Adler et al.: Suppressed  $\pi^0$  production at large transverse momentum in central Au + Au collisions at  $\sqrt{s_{NN}} = 200$  GeV. *Phys. Rev. Lett.*, 91:072301, (2003).
- [19] S. S. Adler et al.: Absence of suppression in particle production at large transverse momentum in  $\sqrt{s_{NN}} = 200$  GeV d + Au collisions. *Phys. Rev. Lett.*, 91:072303, (2003).
- [20] J. Adams et al.: Transverse momentum and collision energy dependence of high  $p_T$  hadron suppression in Au + Au collisions at ultrarelativistic energies. *Phys. Rev. Lett.*, 91:172302, (2003).
- [21] J. Adams et al.: Evidence from d + Au measurements for final-state suppression of high  $p_T$  hadrons in Au + Au collisions at RHIC. *Phys. Rev. Lett.*, 91:072304, (2003).
- [22] B. B. Back et al.: Centrality dependence of charged hadron transverse momentum spectra in d + Au collisions at  $\sqrt{s_{NN}} = 200$  GeV. *Phys. Rev. Lett.*, 91:072302, (2003).
- [23] I. Arsene et al.: Transverse momentum spectra in Au + Au and d + Au collisions at  $\sqrt{s_{NN}} = 200$  GeV and the pseudorapidity dependence of high  $p_T$  suppression. *Phys. Rev. Lett.*, 91:072305, (2003).

- 
- [24] G. Agakichiev et al.: Semi-hard scattering unraveled from collective dynamics by two-pion correlations in 158 AGeV/c Pb + Au collisions. *Phys. Rev. Lett.*, 92:032301, (2004).
- [25] D. Adamova et al.: Event-by-event fluctuations of the mean transverse momentum in 40 AGeV/c, 80 AGeV/c, and 158 AGeV/c Pb + Au collisions. *Nucl. Phys.*, A727:97–119, (2003).
- [26] Asakawa et al.: Fluctuation probes of quark deconfinement. *Phys. Rev. Lett.*, 85:2072–2075, (2000).
- [27] W. M. Yao et al.: Review of particle physics. *J. Phys.*, G33:1–1232, (2006).
- [28] T. Biro and J. Zimanyi: Quarkochemistry in relativistic heavy ion collisions. *Phys. Lett.*, B113:6, (1982).
- [29] J. Rafelski and B. Muller: Strangeness Production in the Quark - Gluon Plasma. *Phys. Rev. Lett.*, 48:1066, (1982).
- [30] J. Bartke et al.: Neutral strange particle production in sulphur sulphur and proton sulphur collisions at 200 GeV/nucleon. *Z. Phys.*, C48:191–200, (1990).
- [31] E. Andersen et al.: Strangeness enhancement at mid-rapidity in Pb Pb collisions at 158-A-GeV/c. *Phys. Lett.*, B449:401–406, (1999).
- [32] M. Gazdzicki and M. I. Gorenstein: On the early stage of nucleus nucleus collisions. *Acta Phys. Polon.*, B30:2705, (1999).
- [33] S. V. Afanasiev et al.: Energy dependence of pion and kaon production in central Pb + Pb collisions. *Phys. Rev.*, C66:054902, (2002).
- [34] C. Alt et al.: Pion and kaon production in central Pb+Pb collisions at 20A and 30A GeV: Evidence for the onset of deconfinement. (2007).
- [35] D. Di Bari et al.: Results on the production of baryons with  $|S| = 1, 2, 3$  and strange mesons in S + W collisions at 200-GeV/c per nucleon. *Nucl. Phys.*, A590:307c–315c, (1995).
- [36] F. Antinori et al.: Transverse mass spectra of strange and multi-strange particles in Pb Pb collisions at 158 AGeV/c. *Eur. Phys. J.*, C14:633–641, (2000).

- 
- [37] F. Antinori et al.: Enhancement of hyperon production at central rapidity in 158 AGeV/c Pb Pb collisions. *J. Phys.*, G32:427–442, (2006).
- [38] F. Antinori et al.: Energy dependence of hyperon production in nucleus nucleus collisions at SPS. *Phys. Lett.*, B595:68–74, (2004).
- [39] L. Sandor: Results on strangeness production from the NA57 experiment. *J. Phys.*, G31:S919–S927, (2005).
- [40] I. Bearden et al.: Strange meson enhancement in Pb Pb collisions. *Phys. Lett.*, B471:6–12, (1999).
- [41] G. Agakishiev et al.: Enhanced production of low mass electron pairs in 200 GeV/u S + Au collisions at the CERN SPS. *Phys. Rev. Lett.*, 75: 1272–1275, (1995).
- [42] G. Agakishiev et al.: e+ e- pair production in Pb Au collisions at 158-GeV per nucleon. *Eur. Phys. J.*, C41:475–513, (2005).
- [43] D. Adamova et al.: Leptonic and charged kaon decay modes of the Phi meson measured in heavy-ion collisions at the CERN SPS. *Phys. Rev. Lett.*, 96:152301, (2006).
- [44] S. Radomski: *Neutral strange particle production at top SPS energy measured by the CERES experiment*. PhD thesis, Technische Universität Darmstadt, 2006.
- [45] H. Appelshäuser: Physics with the upgraded CERES detector. *Acta Phys. Polon.*, B29:3153–3159, (1998).
- [46] E. Gatti and P. Rehak: Semiconductor drift chamber - an application of a novel charge transport scheme. *Nucl. Instrum. Meth.*, A225:608–614, (1984).
- [47] D. Miskowicz: Collections of CERES results. *Nucl. Phys.*, A774:43–50, (2006).
- [48] I. G. Bearden et al.: Particle production in central Pb+Pb collisions at 158A GeV/c. *Phys. Rev.*, C66:044907, (2002).
- [49] D. Miskowicz: Beam Trigger description, (2004). URL <http://www-linux.gsi.de/misko/ceres/analysis.html>.
- [50] D. Antonczyk: *Detailed Analysis of Two Particle Correlations in Central Pb-Au Collisions at 158 GeV per Nucleon*. PhD thesis, Technische Universität Darmstadt, 2006.

- [51] D. Rohrlich: Review of SPS experimental results on strangeness. *J. Phys.*, G27:355–366, (2001).
- [52] C. Höhne: Strangeness production in nuclear collisions: Recent results from experiment NA49. *Nucl. Phys.*, A661:485–488, (1999).
- [53] R. Brun and F. Rademakes: ROOT An object oriented data analysis framework, 1995. URL <http://root.cern.ch/>.
- [54] F. Antinori et al.: Study of the transverse mass spectra of strange particles in Pb - Pb collisions at 158 AGeV/c. *J. Phys.*, G30:823–840, (2004).
- [55] T. Anticic et al.: Energy and centrality dependence of deuteron and proton production in Pb+Pb collisions at relativistic energies. *Phys. Rev.*, C69:024902, (2004).
- [56] T. Anticic et al.: Lambda and anti-Lambda production in central Pb Pb collisions at 40 AGeV, 80 AGeV, and 158 AGeV. *Phys. Rev. Lett.*, 93:022302, (2004).
- [57] S. V. Afanasiev et al.: Xi- and anti-Xi+ production in central Pb + Pb collisions at 158-GeV/c per nucleon. *Phys. Lett.*, B538:275–281, (2002).
- [58] C. Alt et al.: Omega- and Antiomega+ production in central Pb + Pb collisions at 40 AGeV and 158 AGeV. *Phys. Rev. Lett.*, 94:192301, (2005).
- [59] F. Antinori et al.: Rapidity distributions around mid-rapidity of strange particles in Pb Pb collisions at 158-A-GeV/c. *J. Phys.*, G31:1345–1357, (2005).
- [60] A. Bialas et al.: Multiplicity distributions in nucleus-nucleus collisions at high energies. *Nuclear Physics B*, 111:461–476, (1976).
- [61] K. J. Eskola et al.: Quark and Gluon Production in High-Energy Nucleus-Nucleus Collisions. *Nucl. Phys.*, B323:37, (1989).
- [62] A. Bialas and A. Bzdak: Wounded quarks and diquarks in high energy collisions. (2007).
- [63] D. Miskowiec: Nuclear Overlap Calculation, 2001. URL <http://www-linux.gsi.de/~misko/overlap/>.
- [64] J. L. Klay et al.: Charged pion production in 2-AGeV to 8-AGeV central Au + Au collisions. *Phys. Rev.*, C68:054905, (2003).

- 
- [65] L. Ahle et al.: Excitation function of  $K^+$  and  $\pi^+$  production in Au + Au reactions at 2-A-GeV to 10-A-GeV. *Phys. Lett.*, B476:1–8, (2000).
- [66] S. S. Adler et al.: Identified charged particle spectra and yields in Au + Au collisions at  $\sqrt{s} = 200$  GeV. *Phys. Rev.*, C69:034909, (2004).
- [67] A. Andronic et al.: Hadron production in central nucleus nucleus collisions at chemical freeze-out. *Nucl. Phys.*, A772:167–199, (2006).
- [68] T. Alber et al.: Strange particle production in nuclear collisions at 200-GeV per nucleon. *Z. Phys.*, C64:195–207, (1994).
- [69] CBM Collaboration: Technical Status Report, DOC-2005-Feb-447/QCD\_CBM-report. GSI, 2005.
- [70] I. Frank and V. Ginsburg: *J. Phys.*, 9:353, (1945).
- [71] A. Andronic et al.: Transition radiation spectra of electrons from 1 to 10 GeV/c in regular and irregular radiators. *Nucl.Instrum.Meth.A*, 558: 516–525, (2006).
- [72] ALICE Collaboration: ALICE TRD Technical Design Report. CERN/LHCC, 2001-021.
- [73] ATLAS Collaboration: ATLAS TDR Technical Design Report 5. CERN/LHCC, 97-17.
- [74] A. Andronic et al.: Energy loss of pions and electrons of 1-6 GeV/c in drift chambers operated with Xe,CO<sub>2</sub>(15%). *Nucl.Instrum.Meth.A*, 519: 508–517, (2004).
- [75] W. Blum and L. Rolandi: *Particle Detection with Drift Chambers*. Springer Berlin, 1994.
- [76] C. W. Fabjan and W. Struczinski: Coherent emission of transition radiation in periodic radiators. *Physics Letters B*, 57:483–486, (1975).
- [77] R. Appuhn et al.: Transition radiation detectors for electron identification beyond 1 GeV/c. *Nucl. Instrum. Meth. A*, 263:309–318, (1988).
- [78] M. Holder and H. Suhr: Separation of electrons and pions by a transition radiation detector using flash ADCs. *Nucl Instrum Meth A*, 263:319–324, (1988).
- [79] B. Dolgoshein: Transition radiation detectors. *Nucl.Instrum.Meth.A*, 326:434–469, (1993).

- [80] A. Andronic et al.: Electron/pion identification with fast TRD prototypes. *GSI Scientific Report*, 01, (2006).

## Acknowledgements

And now for something completely different. The time is nearly over and I take my pleasure to write a few words to mention and honor at least a small fraction of the people that not only helped me on my way, but also believed it is a good idea to finish this thesis.

I consider myself very lucky for having the opportunity of spending a few years at an international research center not only because of all the knowledge and enthusiasm concentrated here, but also for the possibility to meet many different people from different countries. Here I would like to thank to my colleagues and teachers from Comenius University who have introduced me to the "Big World". Especially I would like to thank Prof. Sitar, Dr. Strmen and Ing. Janik.

To finish this thesis took indeed longer than I expected, though I would not dare to bet whether I would have finished it without a help of my colleagues at all. At the very beginning during my late discovery of the C++ the support from Denis and Mohammad was invaluable. Once I moved more towards physics problems the discussions with Anton or Dariusz often let me thinking: ".. of course it has to be that way, why didn't I realize it before ..". When things did not work well (most of the time) the discussions with Oliver or Ana concerning possible checks either on data or simulations often directed my attention to the details I have overlooked. To discuss some results or problems with Ana was often a dangerous business as her insights and questions led so many times to numerous additional systematical checks or uncovered topics I considered solved or final. And then all the little help, suggestions and intriguing questions from, Sylwester, Juan, Sedat, Jens, Georgios, Silvia, Raphaele, Jacek and others were the daily bread and butter for my soul and work. A big thanks goes to Anar. His kindness and willingness to help when an unsolvable problem appeared in my code, saved my day many times.

I am specially grateful to my boss Prof. Braun-Munzinger for giving me the opportunity to accomplish my PhD study at GSI. It were not only our discussions about my analysis that were so essential for my progress. The way the significance of the results was put in a wider context together with the importance of the attitude towards the work itself changed my point of view.

I am very grateful to my parents and Dasa whose love and support goes far beyond what can be described with a few words.

But it was not only the support of my colleagues, friends and family that



helped me on my way and made my stay in GSI worthwhile and interesting. The new friendships, interests, contacts and activities both numerous and diverse allowed me to learn to look at the world around in a different way.

A special event that needs to be mentioned were the daily coffee breaks. This very important and enjoyable social event was, as well as the lunch that preceded it, a mixture of everything. Here the topics like global warming, medieval European history or (should I say that) photography were discussed, new team members were introduced and birthdays were celebrated.

At the very end I would like to express a sincere thank you to all the people I had the opportunity to meet, as they gave this whole story its colors and sense.

## curriculum vitae

---

### Personal data

name	Matus Kalisky
date of birth	10th November 1979
nationality	Slovak
address	Bornstrasse 7 64291 Darmstadt Deutschland

### Contact data

GSI	Phone: +49-6159-71 2183
Planckstrasse 1	Fax: +49-6159-71 2989
64291	m.kalisky@gsi.de
Darmstadt	

### Education

Doctoral studies:  
Ph.D. Nuclear physics, Technical University Darmstadt, 2003 - 2008 (Expected)

University:  
Mgr. Nuclear Physics, Comenius University, Bratislava, 1998 - 2003  
Master Thesis: Characteristics of proportional chambers for TPC - ALICE

### Professional experience

Research assistant, GSI, Darmstadt, 2003 - present

### Publications and talks

A Transition Radiation Detector for the CBM experiment at FAIR, GSI scientific report, p11, (2004)  
High rate performance of fast gaseous detectors, GSI scientific report, p.362 (2004)  
Charged Kaon Analysis within the CERES experiment, GSI scientific report, p. 163 (2006)  
TRD layout, presentation : CBM Collaboration meeting, (2005)  
Electron/pion identification with fast TRD prototypes, CBM Progress Report, published in GSI scientific report, p. 233 (2006)

### Technical skills

programming: C++, ROOT  
applications:  $\text{\LaTeX}$ , Adobe Photoshop

### Other activities

CERN Summer student program 2002

### Languages

English, German (passive)

### Personal interests

photography, dancing, hiking